SANDIA REPORT

SAND2009-6086
Unlimited Release
Printed September 2009

Vibrational Spectra of Nanowires Measured Using Laser Doppler Vibrometry and STM Studies of Epitaxial Graphene: An LDRD Fellowship Report

Laura B. Biedermann

Prepared by
Sandia National Laboratories
Albuquerque, New Mexico 87185 and Livermore, California 94550

Sandia is a multiprogram laboratory operated by Sandia Corporation,
a Lockheed Martin Company, for the United States Department of Energy's
National Nuclear Security Administration under Contract DE-AC04-94-AL85000.

Approved for public release; further dissemination unlimited.

Sandia National Laboratories

Issued by Sandia National Laboratories, operated for the United States Department of Energy by Sandia Corporation.

NOTICE: This report was prepared as an account of work sponsored by an agency of the United States Government. Neither the United States Government, nor any agency thereof, nor any of their employees, nor any of their contractors, subcontractors, or their employees, make any warranty, express or implied, or assume any legal liability or responsibility for the accuracy, completeness, or usefulness of any information, apparatus, product, or process disclosed, or represent that its use would not infringe privately owned rights. Reference herein to any specific commercial product, process, or service by trade name, trademark, manufacturer, or otherwise, does not necessarily constitute or imply its endorsement, recommendation, or favoring by the United States Government, any agency thereof, or any of their contractors or subcontractors. The views and opinions expressed herein do not necessarily state or reflect those of the United States Government, any agency thereof, or any of their contractors.

Printed in the United States of America. This report has been reproduced directly from the best available copy.

Available to DOE and DOE contractors from
U.S. Department of Energy
Office of Scientific and Technical Information
P.O. Box 62
Oak Ridge, TN 37831

Telephone: (865) 576-8401
Facsimile: (865) 576-5728
E-Mail: reports@adonis.osti.gov
Online ordering: http://www.osti.gov/bridge

Available to the public from
U.S. Department of Commerce
National Technical Information Service
5285 Port Royal Rd
Springfield, VA 22161

Telephone: (800) 553-6847
Facsimile: (703) 605-6900
E-Mail: orders@ntis.fedworld.gov
Online ordering: http://www.ntis.gov/help/ordermethods.asp?loc=7-4-0#online

SAND2009-6086
Unlimited Release
Printed September 2009

Vibrational Spectra of Nanowires Measured Using Laser Doppler Vibrometry and STM Studies of Epitaxial Graphene: An LDRD Fellowship Report

Laura Butler Biedermann
Rad Hard CMOS Technology
Sandia National Laboratories
P.O. Box 5800
Albuquerque, NM 87185- 892
lbieder@sandia.gov

Abstract

A few of the many applications for nanowires are high-aspect ratio conductive atomic force microscope (AFM) cantilever tips, force and mass sensors, and high-frequency resonators. Reliable estimates for the elastic modulus of nanowires and the quality factor of their oscillations are of interest to help enable these applications. Furthermore, a real-time, non-destructive technique to measure the vibrational spectra of nanowires will help enable sensor applications based on nanowires and the use of nanowires as AFM cantilevers (rather than as tips for AFM cantilevers).

Laser Doppler vibrometry is used to measure the vibration spectra of individual cantilevered nanowires, specifically multiwalled carbon nanotubes (MWNTs) and silver gallium nanoneedles. Since the entire vibration spectrum is measured with high frequency resolution (100 Hz for a 10 MHz frequency scan), the resonant frequencies and quality factors of the nanowires are accurately determined. Using Euler-Bernoulli beam theory, the elastic modulus and spring constant can be calculated from the resonance frequencies of the oscillation spectrum and the dimensions of the nanowires, which are obtained from parallel SEM studies. Because the diameters of the nanowires

studied are smaller than the wavelength of the vibrometer's laser, Mie scattering is used to estimate the lower diameter limit for nanowires whose vibration can be measured in this way. The techniques developed in this thesis can be used to measure the vibrational spectra of any suspended nanowire with high frequency resolution

Two different nanowires were measured–MWNTs and Ag_2Ga nanoneedles. Measurements of the thermal vibration spectra of MWNTs under ambient conditions showed that the elastic modulus, E, of plasma-enhanced chemical vapor deposition (PECVD) MWNTs is 37 ± 26 GPa, well within the range of E previously reported for CVD-grown MWNTs. Since the Ag_2Ga nanoneedles have a greater optical scattering efficiency than MWNTs, their vibration spectra was more extensively studied. The thermal vibration spectra of Ag_2Ga nanoneedles was measured under both ambient and low-vacuum conditions. The operational deflection shapes of the vibrating Ag_2Ga nanoneedles was also measured, allowing confirmation of the eigenmodes of vibration. The modulus of the crystalline nanoneedles was 84.3 ± 1.0 GPa.

Gas damping is the dominate mechanism of energy loss for nanowires oscillating under ambient conditions. The measured quality factors, Q, of oscillation are in line with theoretical predictions of air damping in the free molecular gas damping regime. In the free molecular regime, Q_{gas} is linearly proportional to the density and diameter of the nanowire and inversely proportional to the air pressure. Since the density of the Ag_2Ga nanoneedles is three times that of the MWNTs, the Ag_2Ga nanoneedles have greater Q at atmospheric pressures. Our initial measurements of Q for Ag_2Ga nanoneedles in low-vacuum (10 Torr) suggest that the intrinsic Q of these nanoneedles may be on the order of 1000.

The epitaxial carbon that grows after heating $(000\bar{1})$ silicon carbide (SiC) to high temperatures (1450–1600°) in vacuum was also studied. At these high temperatures, the surface Si atoms sublime and the remaining C atoms reconstruct to form graphene. X-ray photoelectron spectroscopy (XPS) and scanning tunneling microscopy (STM) were used to characterize the quality of the few-layer graphene (FLG) surface. The XPS studies were useful in confirming the graphitic composition and measuring the thickness of the FLG samples. STM studies revealed a wide variety of nanometer-scale features that include sharp carbon-rich ridges, moiré superlattices, one-dimensional line defects, and grain boundaries. By imaging these features with atomic scale resolution, considerable insight into the growth mechanisms of FLG on the carbon-face of SiC is obtained.

Acknowledgment

This SAND report is a summary of my graduate research, which was supported by Sandia National Laboratories through the Purdue Excellence in Science and Engineering Fellowship from August 2005 through May 2009. Throughout this fellowship, Dr. Steve Howell of Sandia National Laboratories provided invaluable guidance.

This research, a five-year collaborative effort, was undertaken at Purdue University. First and foremost, I would like to thank my advisor, Professor Ron Reifenberger, for his guidance, wisdom, and humor. When that "great thing called Google" failed, Ron was always there with advice. When the experiments were successful, interesting, or puzzling, I appreciated his insight into how to improve the experiments and explain the results. When the experiments were disappointing, I was immensely grateful to him for his encouragement.

Professor Arvind Raman has graciously served as an unofficial second advisor the past few years. He has been an enthusiastic collaborator in the measurements of the vibrational spectra of nanowires. I have appreciated working with all of his graduate students, whom have been fabulous collaborators and friends. First, all of the vibrometer measurements of carbon nanotube spectra were done in collaboration with Ryan Tung. Bill Conley and Mark Strus provided insight into the properties of carbon nanotubes. Much of my understanding of cantilever dynamics comes from reading papers and attending presentations by John Melcher as well as many hours of conversations with John. Ryan Wagner assisted with the Sader's method calculations. José Lozano is thanked for his advice concerning thermally-excited cantilevers and the fluctuation-dissipation theorem.

As this SAND report is a summary of my graduate research, I would like to thank the members of my thesis committee, Professor Erica Carlson, Dr. Steve Howell, and Professor Ken Ritchie for their experimental advice as well as for being excellent role models and teachers.

I have been fortunate to meet a number of inspiring collaborators. Dr. Mehdi Yazdanpanah of the University of Louisville provided the silver gallium nanoneedles whose vibrational spect and operational deflection shape were measured. Professor Michael Capano, Michael Bolen, and Sara Harrison were instrumental collaborators in the study of epitaxial graphene as they grew all the samples studied and contributed to the analysis. I thank Dr. Dima Zemlyanov for his x-ray photoemission spectroscopy analysis of the graphene samples. Gyan Prakash's atomic force microscopy studies of the same graphene samples were very illuminating.

I would especially like to thank Mark Smith and Dr. Bob Santini for their electronics advice for the tunnel gap modulation spectroscopy project. While that experiment was not successful, I will always appreciate their kind assistance and remember their advice.

My labmates have been wonderful sources of support, encouragement, advice, laughter, and

spare hands over the past five years. I would like to thank Babita Dhayal, Roya Lahiji, Chun Lan, Deepak Pandey, Gyan Prakash, Yexian Qin, Joel Therrien, and Steve Tripp,

Finally, I thank my mom and dad for their years of support, including letting me solder electronics in the living room and study vibrational modes with sand in the kitchen. I am very lucky to have such encouraging parents. Last, but not least, I owe more thanks than I can express to my loving husband, Eric. Eric literally went the extra mile to support me throughout my PhD.

Studies of the epitaxial graphene growth were supported by the Indiana 21st Century Fund.

Contents

Preface **18**

Nomenclature **19**

1 Introduction **21**

1.1 Chapters of this SAND report 22

2 A brief literature review for carbon nanotubes and silver gallium nanoneedles **25**

2.1 Overview of carbon nanotubes 25

2.1.1 Growth methods for MWNTs 26

2.1.2 Mechanical properties of carbon nanotubes 26

Experimental methods to measure the elastic modulus of MWNTs 27

2.1.3 Electrical properties of carbon nanotubes 28

2.2 Overview of silver gallium nanoneedles 29

2.2.1 Fabrication of Ag_2Ga nanoneedles 30

2.2.2 Prior measurements of E, Q, and k_c of Ag_2Ga nanoneedles 30

2.2.3 Applications for Ag_2Ga nanoneedles 31

3 Eigenfrequencies and vibrational spectra of cantilevered nanowires **33**

3.1 Oscillation frequency of cantilevered nanowires 33

3.2 Frequency response function (FRF) for a cantilever 35

3.3 Power spectral density (PSD) of a cantilevered beam 36

3.3.1 Autocorrelation of a random signal 36

3.3.2 Power spectral density (PSD) of a cantilevered beam 37

3.3.3 Extension to multimode harmonic oscillators 37

3.4 Damping and quality factor of cantilevers in fluids 39

3.4.1 Damping in the continuum, cross-over and free-molecular regimes 39

3.4.2 Calculated quality factor due to gas damping at atmospheric pressure 42

4 Experimental details for measurements of the vibrational spectra of nanowires 43

4.1 Polytec MSA-400 scanning vibrometer 43

4.2 Calibration of LDV by measuring the thermal tuning curve of a Si microcantilever 45

4.2.1 Experimental details 46

4.2.2 k_c from Sader's method for AFM and LDV data 47

4.2.3 Calculation of $\langle z^2 \rangle$ from $z_{meas}(t)$ and from the PSD 48

4.2.4 Comparison of the potential and thermal energy of a Si_3N_4 cantilever in thermal equilibrium 48

4.3 The MWNT-Ni STM tips 49

4.3.1 Literature review of affixing MWNTs to AFM tips 49

4.3.2 Creating MWNT-Ni STM tips 50

Etching Ni tips 50

Affixing MWNTs to Ni-STM tips 50

4.4 Ultimate measurement limits for LDV calculated using Mie scatting theory 51

5 Measured vibration spectra, elastic modulus, and quality factors of MWNTs and Ag_2Ga nanoneedles 55

5.1 Qualitative MWNT vibration spectra 55

5.2 Quantitative MWNT spectra measured using LDV 56

5.2.1 Vibration spectra of bare MWNTs 58

5.2.2 Extension to smaller diameters: vibration spectra of MWNTs with beads . . 59

5.3 Ag_2Ga nanoneedle results 62

5.3.1 Eigenfrequencies f_1–f_9 measured from the vibration spectra of a long Ag_2Ga nanoneedle 63

5.3.2 Vibrational spectra of short nanoneedles show flat frequency response below 1 MHz 67

5.3.3 Non-degenerate eigenfrequency peaks caused by asymmetrical nanoneedle cross sections 69

Elliptical nanowires 69

Conjoined cylindrical nanowires 69

5.3.4 Optical forcing and trapping of a Ag_2Ga nanoneedle 72

Brief literature review of optical trapping 72

Optical forces relevant to trapping 72

Optical forces exerted on cylindrical Ag nanowires 73

Experimental observations of optically forced nanoneedles 74

5.3.5 Nanoneedle vibration spectra measured in low vacuum 77

5.4 Measured quality factors of nanowire oscillations 78

5.5 Theoretical basis for understanding Q-factors 79

5.6 Proposed application: nanowires as mass sensors 81

6 A brief review of methods for fabricating graphene and the properties of graphene 85

6.1 Motivation for studying graphene: fundamental physics and applications 85

6.2 Epitaxial graphene growth on SiC 86

6.3 Other methods of producing graphene: exfoliation, chemical vapor deposition, and reduction from graphene oxide 87

7 Insights into Few-Layer Epitaxial Graphene Growth on 4H-SiC(000$\bar{1}$) Substrates from STM Studies 89

7.1 Introduction 89

7.2 Superlattices in layered carbon 90

7.2.1 Defects in highly orientated pyrolitic graphite 90

7.2.2 Superlattices observed in graphene 91
7.2.3 Atomic arrangement of moiré superlattices 91
7.3 Experimental considerations 93
7.3.1 Graphene growth 93
7.3.2 XPS considerations 93
7.3.3 STM considerations 94
7.3.4 Preparation of epitaxial graphene samples for STM 95
7.4 XPS confirmation of graphitic carbon and estimation of graphene thickness 95
7.5 STM study of the C-face growth 97
7.5.1 General observations 97
Pits in the substrate 99
7.5.2 Rough Graphene 100
7.5.3 1D superlattice on smooth FLG 101
7.5.4 Ridges and wrinkles on FLG 101
7.5.5 Moiré superlattices on FLG 104
7.5.6 Atomic resolution within a moiré superlattice 104
7.5.7 I(V) across a moiré region 105
7.5.8 A moiré superlattice across a SiC step edge with constant periodicity 107
7.5.9 Termination and energetics of a small moiré region 108
7.5.10 Moiré superlattices coexistent with wave-like features 109
7.6 Implications for epitaxial graphene growth on SiC 111
7.7 Conclusions 113

8 Contributions and suggestions for future study **115**

References **117**

Appendix

A The solution to the Euler-Bernulli beam equation for a cantilevered beam **131**

B Tunnel Gap Modulation Spectroscopy **137**

B.1 Aim of tunnel gap modulation spectroscopy (TGMS) 137

B.2 Initial TGMS experiments by J. Therrien 140

B.3 Redesign of the rf-STM circuit (June 2006) 142

C Polytec MSA-400 Laser Doppler Vibrometer **151**

C.1 Manufacturer specifications for the Polytec MSA-400-M2-20 Micro System Analyzer 151

C.2 Basic instructions for using the Polytec MSA-400 LDV 151

D Mie Scattering Codes **157**

D.1 Fortran code used to calculate $\mathscr{Q}_{sca}$ 157

D.2 Matlab code used to plot $\mathscr{Q}_{sca}$ 162

E Matlab code for power spectral density (PSD) analysis of vibration spectra **165**

E.1 Main analysis code 165

E.2 Pwelch PlotAnalysis2.m 169

E.3 PeakPower.m 170

F Copyright statements for previously published work **173**

List of Figures

2.1 A sheet of graphene with the chiral vector $\mathbf{C_h}$ specifying a SWNT. The dashed lines indicate the surface of the carbon nanotube. 28

3.1 A schematic of the the point-mass model for cantilever oscillations assuming a stationary base. 38

3.2 Knudsen numbers calculated for the 35-μm wide cantilever and two nanowires of different diameters. Shaded regions indicate the free molecular flow, cross-over, and continuum regimes. 40

3.3 The non-dimensionalized fluid damping coefficients are plotted for the three cantilevers for the case of free molecular (·), cross-over (o), and continuum (+) flow regimes. 42

4.1 In (a), a schematic of the Polytec LDV used in this work. In (b), a schematic diagram of a cantilevered nanowire. The reflected light (R) of the normally incident laser beam (I) is Doppler shifted by frequency Δ when reflected from the MWNT. In (c), an illustration of the relative dimensions when the object beam is focused through the 50× objective. As indicated by the shaded region, the beam waist is much wider than the nanowire. 44

4.2 In (a), an SEM of the 16.6 μm long, 140 nm diameter nanoneedle $NNB2$. Two red circles, diameter 0.9 μm, indicate the spot size of the laser. In (b), the measured ODS and theoretical first eigenmode, both normalized. The laser return at the tip-most point on the nanoneedle was poor; for this reason the last data point underestimates the displacement amplitude. 45

4.3 (a) The FRF of a Si_3N_4 cantilever, as measured using the Nanotec AFM. (b) The power spectral density measured using the LDV for the same cantilever. 47

4.4 Darkfield image of a 13.5 μm MWNT affixed to a nickel STM tip. The magnification is 50x. 51

4.5 The calculated $\mathscr{Q}_{sca}$ for circularly polarized 633 nm light normally incident on a cylindrical nanowire in air as a function of diameter. In (a), the case of light scattering off of metallic silver and graphitic nanowires. The diameters of MWNTs studied fall within the range indicated by the dashed vertical lines. In (b), the case of light scattering off of a semiconducting silicon nanowire. 53

5.1 In (a), a schematic of the experimental set-up for electrostatic excitation of a MWNT. In (b), the electrostatic excitation of MWNT $A7a-9$ at resonance. 56

5.2 The E calculated for seven PECVD-MWNTs based on the resonant frequencies measured in the electrostatic excitation experiments. 57

5.3 In (a), the displacement frequency spectrum from MWNT NT1 shows eigenmode peaks attributed to the 1st and 2nd bending modes of the MWNT. In (b), an SEM micrograph of the MWNT affixed to the Ni tip. 59

5.4 A series of 50× darkfield images showing the transfer of a gold-coated glass bead to a MWNT. 60

5.5 In (a), the velocity spectrum of a MWNT showing a vibration peak at 53.3 kHz that is attributed to the bending oscillation of the MWNT. In (b), an SEM micrograph of the MWNT with gold-coated glass bead affixed to the MWNT tip. 61

5.6 In (a), an SEM micrograph of NNB. (b) The 1st through 4th eigenfrequencies are observed in the velocity PSD. (c) The displacement PSD shows the 2nd through 9th eigenfrequencies. In (d), the measured ODS of the eighth eigenmode. 65

5.7 In (a) and (b), log-log plots of the power spectra densities of NND and NNE, respectively, show a flat frequency response below ∼1 MHz. In (c) and (d), SEM micrographs of NND and NNE, respectively. 68

5.8 In (a) and (b), SEM micrographs of nanoneedle B2 show two parallel nanoneedles, 16.6 μm and 17 μm long. In (c), an illustration of the cross-sectional area. 70

5.9 The vibrational spectra of nanoneedle pair $NNB2$ shows two first eigenfrequency peaks at $f_{1,a} = 0.22$ MHz and $f_{1,b} = 0.46$ MHz and two second eigenfrequency peaks at $f_{2,a} = 1.42$ MHz and $f_{2,b} = 2.79$ MHz. 71

5.10 The optical forcing on a Ag nanowire from a 633 nm, 1 mW Gaussian laser beam as a function of nanowire diameter. 74

5.11 A 50× optical microscope image of nanoneedle NNF (d_o=65 nm, L=21.5 μm), bent $\Delta = 2\,\mu$m away from the equilibrium position due to the optical forcing. 75

5.12 (a) The time series measurement of the fundamental (j=1) oscillations of NNB shows sinusoidal oscillations with an amplitude of ∼25 nm and a beat frequency of 2.0 kHz. In (b), the Fourier transform of the time series signal has two low-frequency peaks at 29.9 kHz and 31.9 kHz. 76

5.13 (a) The thermal spectra of nanoneedle NNB, measured at 650 mTorr, shows f_2–f_4, f_6, and f_7. In (b) the split eigenfrequency peaks f_2^{vac} and f_3^{vac} are visible in this smaller frequency range. Inset (c) highlights the high quality factor of these vibrations, Q_7^{vac} = 370. 78

5.14 The measured Q_j of *NNB* increased linearly with frequency. 80

5.15 The calculated Q_{gas} for nanowires oscillating at atmospheric pressure, using the calculations of the free molecular flow regime. Q_{gas} is calculated for Ag_2Ga nanoneedles (red) and MWNTs (blue) of representative diameters. Measured Q_{meas} corresponding to the first eigenmode of vibration are superimposed on the calculated Q_{gas} 81

7.1 In the Bernal stacking of HOPG (a), the layers alternate **ABAB**. (b) A rotation of the top graphene layer of the HOPG can lead to **AAB**, **slip B**, or **BAB** stacking sequences. 92

7.2 The C-1s XPS spectra, collected at $\theta = 0^o$, from a reference HOPG substrate (a) and from a FLG sample grown at 1500 °C on SiC (b). The similarity of the two XPS spectra indicates the presence of graphitic carbon on SiC. A closer examination of the region between 288 eV and 295 eV from both samples provides evidence for shake-up satellites. 96

7.3 A gallery of $2 \times 2\,\mu m^2$ AFM (a-b) and STM (c-f) scans showing the stages of graphene growth at temperatures 1350°C–1600°C. 98

7.4 Two examples of ridges surrounding pits in the substrate. In (a), a $2 \times 2\,\mu m^2$ region showing a small pit completely surrounded by ridges (sample 927). In (b) a $7.5 \times 7.5\,\mu m^2$ region showing the highest ridge density observed on these epitaxial graphene samples (sample 976). 99

7.5 STM images of graphene grown at 1475 °C shows rough and smooth graphene. The identification of rough graphene is confirmed from an atomic-resolution image (c). 100

7.6 STM images of a region from the graphene grown at 1500 °C show a parallel 1D features within a grain boundary in rough graphene. 101

7.7 An STM image of a 200×200 nm^2 region shows a 1D superlattice. 102

7.8 STM images of ridges observed on epitaxial graphene grown at 1500^{circ}C (a-c) and 1600^{circ}C (d-f)) 103

7.9 (a) An STM image of a 20×20 nm^2 region shows a moiré superlattice with $\mathscr{D} = 4.44 \pm 0.31$ nm. (c) A 6×6 nm^2 zoom of (a) shows the hexagonal lattice of the top graphene layer. The 2D-FFTs of (a) and (c) are given in (b) and (d), respectively. 105

7.10 (a) A constant-height STM scan of a 14.5×14.5 nm^2 region with a moiré superlattice having a periodicity of 4.8 ± 0.3 nm (V_{bias} = 300 mV). In (b), a 3D-mode STM scan of the same superlattice region. In the low-bias (±50 mV) range, the I(V)s (c) obtained from the 3D-mode STM scan in (b) are linear. 106

7.11 (a) and (b) STM images show a moiré superlattice continuing across 1.1-nm high step edges in the SiC substrate. The superlattice is clearly visible in (c), a 50×50 nm^2 magnified region of the center of (b). A profile (d) drawn across the step edge in (b) illustrates that no apparent row of atoms is missing at the step edge. . . 107

7.12 (a) An STM image (1000×700 nm^2) shows the extent of the moiré region with a periodicity of $\mathscr{D} = 12.7 \pm 2.1$ nm. The exceptionally jagged edge of the moiré region is illustrated by a 350×250 nm^2 inset. 108

7.13 (a) An STM image, 500×500 nm^2, shows a 1 nm high line defect. Carbon ripples emanate from the line defect and cross over the step edge. In (b), an STM image of a 300×300 nm^2 zoom of the rippled region of (a) reveals that a superlattice is coexistent with the ripples. In (c), the hexagonal periodicity of the superlattice is confirmed by a 2D-FFT of (b). In (d), a profile of the ripples. 110

List of Tables

2.1 Elastic modulus of MWNTs as determined from experiment. Double-walled MWNTs are indicated by (*). 27

3.1 Allowed α_j which correspond to the first five oscillation frequencies. 34

4.1 Potential energy of a Si_3N_4 cantilever, using $\langle z^2_{freq} \rangle$ = 0.0094 nm^2 and $K^1_{eq} = \alpha_1^4 k_c/12$. The Q is determined from the curve fit to either the AFM or LDV data. . 49

5.1 Experimentally measured elastic modulus for the MWNTs studied. The calculations in this table assume $d_i = 0.5d_o$. The estimated estimated errors are $\pm$10 nm for d_o, $\pm 0.2\,\mu$m for L, and $\pm$2 kHz for f_j. 58

5.2 Experimentally measured elastic modulus for MWNTs with beads. The calculations in this table assume $d_i = 0.5d_o$. The estimated estimated errors are $\pm$10 nm for d_o, $\pm 0.2\,\mu$m for L, and $\pm$2 kHz for f_j. Bead diameters (not listed, estimated error $\pm$20 nm) were measured in the FESEM and used to estimate the mass of the bead. 61

5.3 Dimensions of the eight Ag_2Ga nanoneedles studied as determined from SEM micrographs. In what follows, nanoneedles *NNB*, *NND*, *NNE*, *NNG*, and *NNB*2 are discussed in more detail. 62

5.4 The measured eigenfrequencies, f_j, of *NNB* and mean square displacements, z_j^2, of the 1st–9th eigenmodes, as determined from both the velocity and displacement spectra. The percent error is calculated from the frequency ratios. The scaling factor γ_j is calculated from Eq. 5.10. 66

5.5 The measured eigenfrequencies and quality factors of nanoneedles *NND* and *NNE*. Only a single second eigenfrequency above the noise floor was observed for *NNE*. 68

5.6 Calculated elastic moduli for *NNB*2. 71

5.7 A comparison of the eigenfrequencies and quality factors of *NNB* at 760 Torr (f_j^{atm}) and 650 mTorr (f_j^{vac}). Split eigenfrequency pairs are observed for f_2^{vac} and f_3^{vac}. An undetermined eigenfrequency peak is observed at 0.53 MHz. No peak attributed to the fifth eigenmode was observed. The percent error is calculated from the difference of f_j^{vac}/f_2^{vac} and $(\alpha_j/\alpha_2)^2$. 77

5.8 Quality factors for the MWNTs studied were determined by fitting Eq. 5.2 to the oscillation resonance spectrum. 79

5.9 Dimensions and calculated f_j and Q_j of four representative cantilevers. The silicon microcantilever has a width of 35 μm and a thickness of 2 μm. The MWNT dimensions are representative of typical values. *NND* is a Ag_2Ga nanoneedle whose vibrational spectra was measured (see Section 5.3.2). 83

5.10 At atmospheric pressure (760 Torr), the calculated minimum detectable mass, mass resolution, and expected frequency shift for four representative thermally-excited cantilevers. 84

7.1 Five C-face epitaxial graphene samples were studied in depth with STM and AFM. Only AFM scans are presented for samples 924 and 926, which had incomplete graphene coverage. The growth temperatures and figures acquired from these samples are tabulated below. 95

7.2 Samples with moiré superlattice regions and their measured periodicity 104

Preface

I joined the Reifenberger Nanophysics lab at Purdue University in January 2005 with the goal of designing a custom scanning tunneling microscope (STM) to measure high frequency oscillations in the tunnel current. In 2004 Dr. Joel Therrien, a post-doc in the Reifenberger lab, had conceived of such an STM to measure the oscillations of nanoscale objects, such as multilwalled carbon nanotubes (MWNTs), placed in the tunnel gap of the STM. Joel's early data suggested that the vibrations of the carbon nanotubes, $\sim$1 nm at 10s of MHz, could be measured by monitoring the tunnel current. I worked to both repeat Joel's results and to design a custom STM head to improve the amplification of the high-frequency signals in the tunnel current. As a short summary, I was not able to replicate Joel's results; this effort is described in Appendix B: Tunnel Gap Modulation Spectroscopy (TGMS).

From the TGMS project, I did learn (1) the theory of nanowire oscillations, (2) how to prepare cantilevered MWNT samples, and (3) scanning tunneling microscopy, three skills which I have used throughout my degree. At the 2008 APS March Meeting, I presented a talk describing our measurements of MWNT flexural vibration spectra. This talk led to a collaboration with Dr. Mehdi Yazdanpanah and Prof. Robert Cohn of the University of Louisville. Dr. Yazdanpanah had discovered how to fabricate silver gallium nanoneedles on scanning probe microscope tips, but lacked a facile, non-destructive way to determine their elastic modulus. Using our laser Doppler vibrometery technique, we were able to measure the thermal and driven vibration spectra of these silver gallium nanoneedles and determine their elastic modulus.

My prior STM experience, as well as a long-standing interest in graphene, led me to join a Purdue graphene collaboration in October 2007. I provided STM analysis of epitaxial graphene grown on silicon carbide. This fruitful collaboration, primarily between electrical engineers and physicists at the Birck Nanotechnology Center, has led to insights into the nature of the graphene growth on the carbon-face of SiC.

The results of these projects to measure the vibrational spectra of nanowires, as well as the STM studies of graphene, are presented in this SAND report.

Nomenclature

AFM Atomic force microscopy

CNT Carbon nanotube

CVD Chemical vapor deposition

FLG Few-layer graphene

FRF Frequency response function (linear response function)

LDV Laser Doppler vibrometry

ML Monolayer

MWNT Multiwalled carbon nanotube

MSD Mean square displacement

ODS Operating deflection shape

PECVD Plasma-enhanced chemical vapor deposition

PSD Power spectral density

SEM Scanning electron microscopy

SPM Scanning probe microscopy

STM Scanning tunneling microscopy

TEM Transmission electron microscopy

TGMS Tunnel gap modulation spectroscopy

XPS X-ray photoemission spectroscopy

Chapter 1

Introduction

Current commercial applications for nanowires include probe tips for atomic force microscope (AFM) cantilevers and the use of nanowires as stiffening elements in polymer matrices. Potentially, nanowires may be incorporated into vibrating nanomechanical systems (NEMS) such as ultra-high frequency resonators, force and mass sensors, and nanoelectronics. A challenge limiting the use of nanowires in NEMS is that few methods exist to reliably measure their motion. A real-time technique capable of measuring the vibration of an individual nanowire would enable the design of sensitive chemical sensors and the use of nanowires as oscillators in nanomechanical systems. Of interest are the resonant frequencies of various eigenmodes of oscillation, the quality factor characterizing each resonant eigenmode, and the nanowire material properties required to explain each resonance.

As carbon nanotubes (CNTs) are one of the most extensively studied nanowires, number of methods to determine the resonant frequency of a CNT have been published. Electrically excited resonant vibrations of a cantilevered multiwalled carbon nanotube (MWNT) were observed in a transmission electron microscope (TEM) [1] and from the field emission pattern of a vibrating MWNT [2]. The oscillation of a suspended, doubly clamped MWNT, excited using an oscillating gate voltage, was detected from the modulation in the conductance of the suspended device [3, 4]. The shape of the first three bending eigenmodes of a suspended, doubly clamped MWNT was measured using an AFM [5].

A number of the above techniques have been adopted to measure the resonant frequency of other nanowires. For example, parametric resonance of boron nanowires has been observed in SEM [6]. Driven resonances of composite SiO_2/SiC nanowires have been observed in TEM [7]. Electrostatic actuation and piezoresistive self-detection has been used to detect driven resonance of clamped-clamped Si nanowire resonators [8].

These techniques require either high vacuum conditions, electron microscopy, or complicated fabrication methods that utilize advanced lithographic techniques. A feature common to all these methods is the low frequency resolution that accompanies the measurement of the nanowire vibration spectrum. We have used laser Doppler interferometry to measure the vibration spectra of nanowires with high frequency resolution.

Albert Michelson used an interferometer in 1887 to measure the velocity of light with respect to the Earth's motion [9]. Since then, laser interferometers have been used to measure displacements and velocities with high resolution. The Laser Interferometer Gravitational Wave Observatory

(LIGO) is designed to measure displacements of 10^{-18} m at frequencies as low as 10s of Hz [10]. Interferometers, being highly versatile, are also used to measure acoustic vibrations (few nanometers at tens of kHz frequencies) of the cochlea in the inner ear [11] as well as GHz oscillations of bulk acoustic wave (BAW) resonators [12].

Laser Doppler vibrometery uses the Doppler shift of a reflected laser beam from a vibrating object to measure that object's vibrational velocity. Laser Doppler vibrometers (LDVs) are well suited for real-time measurements of oscillations up to frequencies of tens of MHz with high frequency resolution, enabling a precise determination of resonant frequencies and quality factors of the different eigenmodes. LDV has been used to detect the oscillations of devices such as Si cantilevers [13] and rotational oscillators [14, 15]. The objects studied with LDV need not be larger than the laser beam spot size or wavelength. Recently interferometric methods, including LDV, have been used to measure driven resonances of nanoscale doubly clamped Si beams [16], cantilevered Ag and Rh nanowires in vacuum [17], and Si nanowires [18]. In order to measure the driven resonance of a cantilevered MWNT in vacuum with an LDV, a small Si mirror was affixed to the free end of the MWNT [19].

This report describes the techniques used to measure the vibration spectra of MWNTs and silver gallium nanoneedles and the results obtained with these measurements. While preliminary measurements of driven MWNT vibrations were made using an optical microscope, the majority of the results were obtained using a commercial Polytec MSA-400 scanning LDV.

As demonstrated by the study of these two nanowires, the techniques developed are completely general and can be used under ambient or vacuum conditions to measure the vibration spectra of a wide variety of suspended and cantilevered nanotubes and nanowires. The operating deflection shapes of driven resonances of the silver gallium nanoneedles were also measured. Taken together, these results represent a major advance in the study of the vibrational properties of nanowires.

1.1 Chapters of this SAND report

The above results are discussed in detail as follows. Chapter 2 is an introduction to carbon nanotubes and silver gallium nanoneedles, providing information about their synthesis as well as basic physical properties. Chapter 3 provides the theoretical background to interpret the measured vibration spectra; this chapter includes Euler-Bernoulli beam theory and calculation of the frequency response function of a cantilever using the point-mass model. Since most of the experiments were performed at atmospheric pressure, a discussing of damping and quality factors is presented in section 3.4. Chapter 4 describes the experimental techniques, namely sample preparation and the laser doppler vibrometer used, as well as a discussion of Mie scattering as it applies to nanowires. Chapter 5 presents the results of the nanowire measurements, including the measured oscillation spectra and calculated elastic moduli, and a brief discussion of mass detection. In October 2007, I was asked to perform a scanning tunneling microscopy (STM) analysis of graphene samples. An introduction to graphene, focusing primarily on graphene fabrication and growth, is presented in Chapter 6. Chapter 7 summarizes the insights gained into epitaxial graphene growth from these

STM scans. Contributions of this research and suggestions for future work are summarized in Chapter 8.

Chapter 2

A brief literature review for carbon nanotubes and silver gallium nanoneedles

This chapter presents an introduction to the two types of nanowires that I studied, multiwalled carbon nanotubes and silver gallium nanoneedles. For both types of nanowires, I discuss growth and fabrication methods and prior measurements of material properties, such as the elastic modulus, E. Subsection 2.1.2 describes a number of methods to measure E of a carbon nanotubes; these techniques are generally applicable for measuring E of any nanowire.

2.1 Overview of carbon nanotubes

Carbon nanotubes (CNTs) are a cylindrical member of the fullerene family. A perfect nanotube would consist solely of carbon atoms with each carbon atom bonded to three others. The carbon atoms form a hexagonal planar lattice, as if a sheet of graphene were rolled into a cylinder. Two forms of carbon nanotubes exist, single-walled (SWNT) and multiwalled (MWNT). As the name implies, a SWNT is a two-dimensional cylindrical fullerene structure. A MWNT consists of concentric tubes of graphene with an interlayer spacing of 0.34–0.39 nm; smaller diameter MWNTs have a larger interlayer spacing [20]. Typical SWNTs have diameters of 1–2 nm. MWNTs are larger with outer diameters, d_o, of 5–300 nm and inner diameters, d_i, of 2–100 nm.

While S. Iijima is often cited as the discoverer of carbon nanotubes, carbon nanotubes were observed at least 40 years earlier. Researchers in the 1950s grew carbon filaments with similar dimensions as MWNTs. However, the graphene structure of these filaments could not be resolved; transmission electron microscopes (TEMs) did not obtain nanometer resolution until the 1970s. Two Russian scientists, Radushkevich and Lukyanovich, are credited with first noticing carbon nanotubes in 1952. Individual shells are not visible in their TEM images of the carbon structures, but the electron transparency and dimensions are consistent with those of nanotubes. Radushkevich and Lukyanovich's 1952 paper was published in Russian and not widely available in the west until after the Cold War [21]. In 1991 S. Iijima reported growing "helical microtubules of graphitic carbon" using arc-discharge evaporation [22]. Both Iijima and Ichihashi and Bethune et al. reported the formation of SWNTs in 1993 [21]. Early papers referred to carbon nanotubes as "carbon tubules," "graphene tubules," or "graphitic carbon needles."

2.1.1 Growth methods for MWNTs

Defects in a CNT can adversely effect the elastic and transport properties. The number of defects in a CNT depend on growth conditions. The two techniques most commonly used to grow MWNTs are arc discharge (AD) and chemical vapor deposition (CVD). The arc-discharge method generally produces the highest quality MWNTs, as judged by their concentric SWNT shells, strongest mechanical properties, and best electrical transport characteristics [23]. The paucity of defects in the AD-MWNTs' shells is due to the high growth temperature, 2000-3200° C, which anneals most defects.

CVD-MWNTs were first reported in in 1994 by Amelinckx et al [24]. CVD-MWNTs grow from a variety of catalysts, including Fe, Ni, and Co. For CVD growth, a precursor gas, such as methane, ethane, or other hydrocarbon is used as the feedstock. The high temperatures, typically 500-1500°C, inside the growth chamber cause the feedstock gas to disassociate; MWNT growth then occurs on the catalyst particles [25]. The diameter of the catalyst particles governs the diameter of the CVD-MWNTs. CVD-MWNTs often exhibit growth defects such as bamboo, stacked cone, or coffee cup structures [23, 26]. Despite the increased number of growth defects, CVD-MWNTs are worthy of study since they can be grown to longer lengths, are mass-produced more economically than AD-MWNTs, and can be grown on substrates at lower temperatures. The lower CVD growth temperatures are more compatible with standard semiconductor processing techniques than the high AD growth temperatures.

Plasma-enhanced CVD (PECVD) MWNTs are a subset of CVD-MWNTs. The advantage of PECVD-MWNTs is that growth can occur at even lower temperatures and that PECVD-MWNTs can be grown in vertically-alligned arrays. For PECVD growth, the plasma (frequently from a DC or rf source) disassociates the hydrocarbon feedstock at the surface of the catalyst particle, rather than in the surrounding atmosphere of the growth chamber. This disassociation at the catalyst surface allows the PECVD-MWNTs to grow at even lower temperatures than CVD-MWNTs [23].

2.1.2 Mechanical properties of carbon nanotubes

The hexagonal arrangement of the carbon atoms gives carbon nanotubes their robust nature. Each carbon atom in the graphene tube is σ-bonded to three other carbon atoms through sp^2 orbitals. Nanotubes owe their great strength to the sp^2 carbon-carbon bond, which is the strongest of all chemical bonds [27]. The MWNT shells are coupled mainly by van der Waals intershell attraction [28]. The weak coupling between shells in a MWNT allows the shells to slide independently in a telescoping action [29, 30].

Carbon nanotubes are uniquely suited for applications in nanomechanical systems in part due to their high strength and flexibility. Experiments on AD-MWNTs revealed an elastic (Young's) modulus $\sim$1 TPa, a tensile strength of 11–63 GPa, and a flexural (bending) strength of $\sim$14 GPa [29]. MWNTs are quite flexible; they buckle readily when compressed [31]. Computer simulations of small diameter ($d_o \sim$ 5–10 nm) MWNTs show that MWNTs can elastically bend through angles up to 110°. When bending elastically, the bonds on the outer side of the MWNT stretch and kinks

form on the inner side; no bonds are broken [32].

Experimental methods to measure the elastic modulus of MWNTs

Values of E reported in literature differ over two orders of magnitude, depending on the growth method of the MWNTs (see Table 2.1). Two approaches are commonly used to measure E of MWNTs. By recording the oscillation amplitude at the tip of an oscillating MWNT and the dimensions of the MWNT, E can be inferred from an Euler-Bernoulli analysis of a cantilever beam. In the first experimental determination of E for MWNTs, Treacy et al. observed the thermal excitations of AD-MWNTs in a TEM and noted a full order of magnitude range for E with larger E for smaller diameter MWNTs. The average value of E, 1.8 TPa, was slightly higher than E for the basal plane of graphite, 1.06 TPa [33]. In similar experiments, electrically excited resonant vibrations of MWNTs were observed in a TEM [1] and under a dark-field microscope [34]. Both Treacy et al. and Poncharal et al. noted a decrease in E with increasing MWNT diameter [33, 1].

Table 2.1. Elastic modulus of MWNTs as determined from experiment. Double-walled MWNTs are indicated by (*).

Author	d_o (nm)	E (GPa)	Growth method
Treacy et al. (1996)	6–25	400–3700; $\langle E \rangle$ = 1800	arc-discharge
Wong et al. (1997)	26–76	$\langle E \rangle$ = 1280±590	arc-discharge
Poncharal et al. (1999)	8–40	100–1000	arc-discharge
Salvetat et al (1999)	10–20	$\langle E \rangle$ = 810	arc-discharge
Yu et al. (2000)	19–40	270–950	arc-discharge
Salvetat et al (1999)	26–32	10–50; $\langle E \rangle$ =27	catalytic CVD
Gaillard et al. (2005)	50–150	3–300	CVD
Guhados et al. (2007)	20-50	$\langle E \rangle$ = 350±110	CVD
Lee et al. (2007)	10–25	6–600	catalytic CVD
Lee et al. (2007)	5^*	700–1500	catalytic CVD
Biedermann et al. (2009)	160–230	$\langle E \rangle$ = 40±30	PECVD

The elastic modulus has also been measured by performing force versus distance ($F(z)$) curves on MWNTs. In such studies, the MWNTs can be cantilevered [35] or clamped-clamped [26, 36, 25, 29]. Both geometries for the $F(z)$ curves share the limitation that the boundary conditions of the MWNT clamped to the support cannot be determined accurately. Frequently, the MWNTs are dispersed over a porous substrate; the $F(z)$ curves are performed midway along the suspended length of a nanotube bridging a gap. Using Euler-Bernoulli theory, E is calculated for a clamped-clamped beam with the MWNT dimensions determined from AFM scans.

Two groups have reported a decrease in E with increasing diameter for small-diameter (10–50 nm) CVD-grown MWNTs [36, 25]. Lee et al. theorize that the smaller catalyst particles are completely liquid during the CNT-growth, which promotes fewer growth defects [25].

The first measurement of the shear modulus, $\langle G \rangle = 1.4 \pm 0.3$ GPa, for a MWNT was determined from $F(z)$ curves of a suspended MWNT, as described above. Guhados et al. calculated the deformation of a clamped-clamped beam to depend both on the bending deformation and a shear deformation [36]. This measured value of G is between the values of $G = 0.18$ GPa for pyrolytic graphite and $G = 4.5$ GPa for a perfect graphitic crystal [26].

2.1.3 Electrical properties of carbon nanotubes

To understand the electronic properties of carbon nanotubes, first imagine the prototypical SWNT, open on each end. A SWNT can be conducting or semiconducting, depending on its structure. Consider a SWNT as a rolled-up sheet of graphene, as shown in Fig. 2.1 [37]. The chiral vector, $\mathbf{C_h}$, is the sum of the unit vectors of the honeycomb lattice, $\mathbf{a_1}$ and $\mathbf{a_2}$; $\mathbf{C_h} = n\mathbf{a_1} + m\mathbf{a_2}$, where n and m are integers and $n \geq m$ [27]. The length of the chiral vector is the circumference of the SWNT ($|\mathbf{a_1}| = |\mathbf{a_2}| = 1.42\sqrt{3}\mathring{A}$) [37]. SWNTs are divided into three symmetry groups: armchair (n,n), zigzag $(n,0)$, and chiral. SWNTs are metallic if $n - m = 3q$, where q is an integer, and semiconducting in all other cases. Thus all armchair SWNTs are metallic as well are one-third of chiral and zig-zag SWNTs [27].

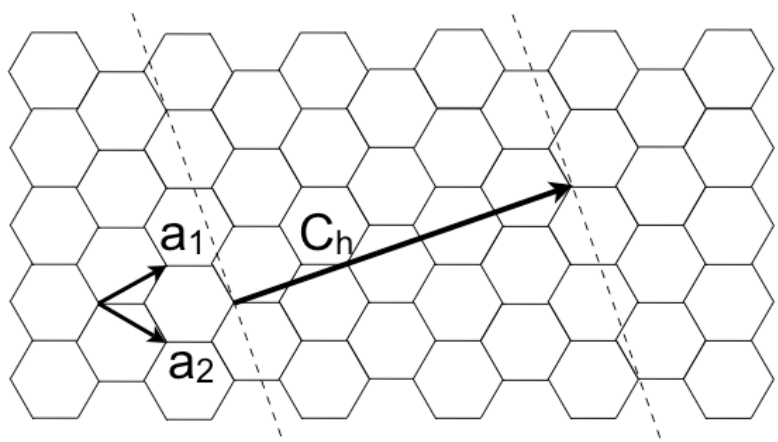

Figure 2.1. A sheet of graphene with the chiral vector $\mathbf{C_h}$ specifying a SWNT, $(n,m) = (4,1)$. The dashed lines indicate the surface of the carbon nanotube. The unit vectors, $\mathbf{a_1}$ and $\mathbf{a_2}$, are also shown (following Dresselhaus, 1995 [37]).

The electrical properties of MWNTs are a subject of current debate. Each shell of a MWNT can be considered as a SWNT and is either metallic or semiconducting. However, intershell interactions exist which may change the conductive properties of the MWNT [38]. Theoretical calculations are reasonably possible only for the simplest case of double-walled carbon nanotubes (DWNTs). Early theoretical calculations suggested that the intershell interactions did not affect the electronic properties of DWNTs due to symmetry considerations [38]. Later calculations showed

that if the inner nanotube were displaced laterally or rotationally to a less symmetric configuration, pseudogaps appeared in the density of states near the Fermi energy [39].

The band gap, E_g, in semiconducting carbon nanotubes is inversely proportional to R, the radius of the nanotube,

$$E_g = |V_o| \frac{a_{c-c}}{R}, \tag{2.1}$$

where $|V_o|$ is the nearest-neighbor transfer integral, 2.7 eV, and a_{c-c} is the carbon-carbon distance, 0.142 nm [40]. Thus, as shown experimentally, narrow MWNTs ($d_o \leq 30$ nm) can be semiconducting or metallic while wide MWNTs are effectively metallic, regardless of their chiral vector [41].

A N-shell MWNT is, electronically, a set of N parallel conductors (both semiconducting and metallic). The number and location of shells participating in electronic conduction is an area of active research. Researchers associated with the Reifenberger Nanophysics Lab found that 25 ± 1 of $\sim$65 shells of a 40-nm MWNT conducted current. The resistance, measured with a two-probe technique, of this MWNT was nearly a multiple of the fundamental quantum of resistance (12.6 kΩ), suggesting ballistic transport [42].

Other studies confirm that multiple shells conduct current, however comparisons between studies are difficult since nanotube growth conditions and diameters are not consistently reported. To count the number of shells carrying current, Collins and Avouris measured resistances of arc-grown MWNTs while sequentially removing the outer shells [43]. This current-induced oxidation technique only removed the outer shells from the MWNT region between the probe electrodes; the portion of the MWNT contacting the electrodes remained intact. At room temperature, the outer shells contributed to conduction; the number of shells conducting ranged from three to nine, depending on the MWNT sample [44]. A second experiment measuring the gate-dependence of conductance showed that a MWNT with an outmost semiconducting shell has non-zero conductance due to inner metallic shells [43].

Chun Lan in the Reifenberger Nanophysics Lab at Purdue University studied the electrical properties of the same PECVD-grown MWNTs whose vibration spectra are reported in this report. She discovered that at low bias voltage, only a few of the MWNT shells conducted current. As the bias voltage increased, more shells conducted current. High bias voltage caused MWNT shells to fail and break [45].

2.2 Overview of silver gallium nanoneedles

Dr. Yazdanpanah discovered how to fabricate silver gallium nanoneedles in 2005. These nanoneedles are a remarkable example of nanoscale self-assembly. Yazdanpanah observed that silver gallium crystals formed when narrow lines of Ga were drawn on thin (15–35 nm thick) Ag films [46]. Further research lead to the fabrication of Ag_2Ga nanoneedles on various probe tips such as conventional Si AFM cantilevers and etched W STM tips. X-ray diffraction patterns and TEM micrographs show that the nanoneedles are crystalline, with uniform diameter along their length [46]. Nanoneedles are faceted with 8-16 sides forming a nearly-circular cross-section. [47]. Based on

the stoichiometric ratio, the density of the Ag_2Ga nanoneedles is estimated to be 8960 kg/m^3 [48].

2.2.1 Fabrication of Ag_2Ga nanoneedles

To prepare an AFM cantilever for use as a substrate for Ag_2Ga nanoneedle growth, a thin (10 nm) Cr adhesion layer is sputter coated onto a pyramidal probe tip. A $\sim$100 nm sputter coated Ag layer provides the Ag material for nanoneedle growth [48]. Thicker Ag layers enable growth of longer nanoneedles [47]. Nanomanipulators inside an SEM allow these coated cantilever tips to be dipped into a sphere of liquid Ga resting on a silicon substrate. As the cantilever is retracted, nanoneedles crystallize in the Ga meniscus. The Ag_2Ga nanoneedles originate from the Cr-Ag boundary [46].

Many short nanoneedles crystallize parallel to the pyramidal AFM tip, but do not protrude past the tip. An ideal nanoneedle-tiped probe would have a single nanoneedle extending from the apex of the AFM cantilever. Frequently, two fused parallel nanoneedles of similar diameter and unequal length extend from the same AFM tip [47]. Typical dimensions of the Ag_2Ga nanoneedles are diameters of 25–500 nm and lengths 1–100 μm. These nanoneedle lengths are much greater than the thickness of the Ga meniscus [46].

2.2.2 Prior measurements of E, Q, and k_c of Ag_2Ga nanoneedles

In 2006, the elastic modulus of a set of 21 Ag_2Ga nanoneedles was determined from measurements of their driven eigenfrequencies in SEM in a manner similar to Poncharal's measurements of driven MWNT oscillations [1, 48]. From the measured resonance frequencies and dimensions of the nanoneedles, an E of 42.6 ± 22.4 GPa was calculated. For a subset of seven nanoneedles, quality factors of 600-3300 in the vacuum of the SEM were estimated from the 3dB-point of the driven resonance peak [48].

Elastic bending experiments were also used to determine the elastic modulus of individual Ag_2Ga nanoneedles. The deflection and bending shape of a Ag_2Ga nanoneedle fabricated on the end of an AFM cantilever were observed in an SEM as the nanoneedle was buckled by compression against a substrate. Timoshenko beam theory, which is valid for large deflections, was used to model the deflection shape of the nanoneedle. From these experiments, a E of 68.3 GPa was calculated for a 157-nm diameter, 15.6-μm long Ag_2Ga nanoneedle [49].

The static bending coefficient, k_c, was measured from $F(z)$ curves for two Ag_2Ga nanoneedles attached to the side of AFM tips. The spring constant of the AFM cantilever-nanoneedle system was modeled as two springs in series. Using this method, k_c of 0.033 N/m and 0.085 N/m were calculated for the two nanoneedles [48].

2.2.3 Applications for Ag_2Ga nanoneedles

Due to their robust nature and high aspect ratio, Ag_2Ga nanoneedles can be used as probe tips for AFM cantilevers. Such nanoneedle-tipped cantilevers can be used for scanning in both contact and tapping mode [46]. Since the nanoneedles are cylindrical, rather than pyramidal as are conventional AFM probe tips, they are ideal for measurements of surface tension and wetting forces from force-distance curves. The low spring constant and constant wetting force as a function of probe diameter make Ag_2Ga nanoneedles ideal for scanning soft materials under liquid, a common condition for biological AFM samples.

Chapter 3

Eigenfrequencies and vibrational spectra of cantilevered nanowires

This chapter presents the fundamental framework for calculating the eigenfrequencies of vibration for cantilevered nanowires from Euler-Bernoulli beam theory (section 1). The vibrational spectra of the nanowires is measured, in either the frequency or time domain, and the eigenfrequencies determined using one of two methods. Frequency spectra is analyzed by comparison to the frequency response function (FRF) for a linear spring-mass system, as described in section 2. The vibrational spectra of a thermally excited cantilever is random in time. For this reason, the power spectral density (PSD), appropriate for random signals, is calculated. Section 3 presents the relationship between the PSD and the FRF using the fluctuation dissipation theorem.

At atmospheric pressures, the dominant mechanism of energy loss is fluid damping. Section 4 presents a brief discussion of the damping in the continuum, cross-over, and free molecular regimes as they apply to nanostructures of the dimension studied. Estimated quality factors of the fluid damping are also given.

3.1 Oscillation frequency of cantilevered nanowires

To calculate the resonant frequency of a nanowire, the nanowire is modeled as a cantilevered beam of length L. By the equipartition theorem, the transverse, longitudinal, and torsional modes of vibration will be equally thermally excited. For this work, only the transverse mode is considered since it leads to the greatest displacement of the nanowire. The transversal vibrations of the nanowire are given by the Euler-Bernoulli equation,

$$\frac{\partial^2 w(x,t)}{\partial t^2} + \frac{EI}{\rho_L}\frac{\partial^4 w(x,t)}{\partial x^4} = 0 \tag{3.1}$$

where E is the elastic modulus, I is the areal moment of inertia, and ρ_L is the density per unit length, calculated by multiplying ρ, the density of the nanowire by its cross-sectional area. The bending deflection of the nanowire, $w(x,t) = \Phi(x)z(t)$ is a function of x, the distance along the length of the nanowire and time, t. The bending deflection can be decomposed into $\Phi(x)$, a function describing the oscillation mode shape, and $z(t)$, the deflection of the free end of the nanowire.

Using separation of variables, a solution of the form (3.2) is substituted into (3.1)

$$w(x,t) = \sum_{j=1}^{\infty} C_j \Phi_j(x) e^{\pm i\omega_j t}, \tag{3.2}$$

which yields

$$\frac{\partial^4 \Phi_j(x)}{\partial x^4} - \left(\frac{\alpha_j}{L}\right)\Phi_j(x) = 0, \text{ where,} \tag{3.3}$$

$$(\alpha_j/L)^4 = \rho_L \omega_j^2/EI. \tag{3.4}$$

Equation 3.3 is solved by applying the boundary conditions for a cantilevered beam. The resulting transcendental dispersion equation,

$$\cos(\alpha_j)\cosh(\alpha_j) + 1 = 0 \tag{3.5}$$

is solved numerically; Table 3.1 gives the solutions corresponding to the first five eigenfrequencies, f_j. Appendix A gives a complete derivation of the eigenfrequencies and eigenmodes of oscillation.

The eigenfrequencies of oscillation for a cantilevered beam as a function of length are given by [50]

$$f_j = \frac{\alpha_j^2}{2\pi L^2}\sqrt{\frac{EI}{\rho_L}}, \tag{3.6}$$

assuming that I and ρ are constant along the length of the cantilevered beam.

In the case of a hollow cylinder, such as a MWNT, of inner diameter, d_i, and outer diameter, d_o, Eq. 3.6 can be rewritten as

$$f_j = \frac{\alpha_j^2}{8\pi L^2}\sqrt{\frac{E}{\rho}(d_o^2 + d_i^2)}, \tag{3.7}$$

where the substitutions $I = \pi(d_o^4 - d_i^4)/64$ and $\rho_L = \pi\rho(d_o^2 - d_i^2)/4$ were used. For a solid nanowire ($d_i = 0$) Eq. 3.6 simplifies further to

$$f_j = \frac{\alpha_j^2}{8\pi L^2} d_o \sqrt{\frac{E}{\rho}}. \tag{3.8}$$

For both MWNTs and Ag_2Ga nanoneedles, typical lengths are 5–50 μm and outer diameters are 50–200 nm. Based on TEM micrographs of MWNTs, d_i is estimated to be $0.5\,d_o$. The density of MWNTs is assumed to be that of graphite, 2300 kg/m^3. From the stoichiometric ratio, ρ = 8960 kg/m^3 is estimated for Ag_2Ga nanoneedles [48]. Estimates for the first eigenfrequencies range from 10s of kHz for the longest nanowires to 1000s of kHz for short nanowires.

Table 3.1. Allowed α_j which correspond to the first five oscillation frequencies.

j	1	2	3	4	5
α_j	1.8751	4.6941	7.8548	10.995	14.1372

3.2 Frequency response function (FRF) for a cantilever

A cantilevered beam in a fluid (gas or liquid) is an example of a linear spring-mass system with viscous damping. In the time domain, the motion of such as system is described by Newton's equation of motion for damped, driven oscillations. The drive force, $f(t)$, is assumed to be harmonic, but could represent many types of forcing, including acoustic, base, and thermal excitations. In the time domain, the displacement $z(t)$ of a linear spring-mass system is

$$m\ddot{z} + c\dot{z} + k_c z = f(t) \tag{3.9}$$

where m is the mass of the cantilever, c is the damping, and k_c is the static bending coefficient. For the case that $f(t)$ is a harmonic forcing of the form $F_o e^{i\omega t}$, the solution to Eq. 3.9 is assumed to be $z = Ze^{i(\omega t - \delta)}$.

Since the eigenfrequencies of oscillation are of interest, Eq. 3.9 is converted to the frequency domain by taking the Fourier transform of Eq. 3.9 which yields

$$-m\omega^2 Z(\omega) + ic\omega Z(\omega) + k_c Z(\omega) = F(\omega), \tag{3.10}$$

where $z(t) \Leftrightarrow Z(\omega)$ and $f(t) \Leftrightarrow F(\omega)$. Solving Eq. 3.10 for $Z(\omega)$ yields the frequency response function (FRF, also referred to as the linear response function), $Z(\omega)$

$$Z(\omega) = \frac{F(\omega)}{[-m\omega^2 + ic\omega + k_c]}, \tag{3.11}$$

where the transfer function is $\left[-m\omega^2 + ic\omega + k_c\right]^{-1}$. Using the substitutions $k_c/m = \omega_o^2$ and $c/m = \omega_o/Q$ [51], Eq. 3.11 can be re-written in terms of the resonant frequency ω_o and quality factor, Q, as

$$Z(\omega) = \frac{F(\omega)/k_c}{\left[1 - \left(\frac{\omega}{\omega_o}\right)^2 + i\frac{\omega}{Q\omega_o}\right]} \tag{3.12}$$

The magnitude of $Z(\omega)$ is

$$|Z(\omega)| = \frac{F(\omega)/k_c}{\sqrt{\left[1 - \left(\frac{\omega}{\omega_o}\right)^2\right]^2 + \left(\frac{\omega}{Q\omega_o}\right)^2}} \tag{3.13}$$

The above FRF is valid for any system described by Eq. 3.9, including cantilevered nanowires. Since the vibration spectra of the MWNTs were measured in the frequency domain, the eigenfrequencies f_j and associated quality factors Q were found by fitting Eq. 3.13 to the measured spectra.

The two frequency limits ($\omega \ll \omega_o$ and $\omega \gg \omega_o$) suggest how a cantilevered nanowire can be used as a vibrometer or accelerometer. To understand these limits, consider a sinusoidal base

motion of the form $F(\omega) = m\omega^2 A_{base}$, where A_{base} is the base motion of the fixed end of the cantilever. In the low-frequency limit, Eq. 3.13 reduces to

$$|Z(\omega)| = \frac{F(\omega)}{k_c} A_{base}, \text{ where } \omega \ll \omega_o. \tag{3.14}$$

Since $|Z(\omega)|$ is proportional to A_{base}, the cantilevered nanowire can be used as a vibrometer. In the high-frequency limit, Eq. 3.13 reduces to

$$|Z(\omega)| = \frac{F(\omega)}{m\omega_o^2}\left(\frac{\omega_o}{\omega}\right)^2 = \frac{acceleration}{\omega^2}, \text{ where } \omega \gg \omega_o. \tag{3.15}$$

Thus in the high-frequency limit, the cantilever behaves as an accelerometer [52].

3.3 Power spectral density (PSD) of a cantilevered beam

With the Polytec MSA-400 system, measurements of the vibration spectrum in time can have a much higher data resolution than those measured in frequency. For this reason, it is useful to measure the displacement (or velocity) of the thermally-excited cantilever in the time domain and Fourier transform that signal to the frequency domain. This approach requires a statistically valid method to transform the vibration spectrum into the frequency domain so that the eigenfrequency peaks can be identified. Second, the appropriate theoretical response of the cantilever in the frequency domain must be derived.

3.3.1 Autocorrelation of a random signal

The Fourier transform of a signal is defined only for periodic signals. For this reason, it is not accurate to directly take the Fourier transform of the time series measurement of a thermally-excited cantilever's oscillation. Instead, the autocorrelation function, $R_{hh}(\tau)$, is first calculated. The autocorrelation function is a mathematical tool for finding periodic signals in random data and is defined as

$$R_{hh}(\tau) = \lim_{\mathsf{T}\to\infty} \frac{1}{\mathsf{T}} \int_{-\mathsf{T}/2}^{\mathsf{T}/2} h(t)h(t+\tau)dt \tag{3.16}$$

where $h(t)$ is a generic random signal in time, τ is a time interval, and T is the period. The double-subscript hh indicates the autocorrelation of $h(t)$ with itself. The cross-correlation of signals $g(t)$ and $h(t)$ would be written as $R_{gh}(\tau)$. An important property of $R_{hh}(\tau)$ is that "If a random process has a periodic component, of period T, then the autocorrelation function also has a periodic component of period T" (ref. [[53]], pg. 201). Taking the Fourier transform of Eq. 3.16 yields the power spectral density (PSD) $S_{hh}(\omega)$, which is defined as [53]

$$S_{hh}(\omega) = \int_{-\infty}^{\infty} R_{hh}(\tau)e^{-i\omega\tau}d\tau. \tag{3.17}$$

For white noise, $S_{hh}(\omega)$ is a constant.

For discrete data sets, the Fourier transform of the signal's autocorrelation function can be accomplished using the PWelch algorithm. This algorithm is implemented in Matlab following the method of Welch [54]. For an example of the Matlab code used to analyze the time series data, see Appendix E.

3.3.2 Power spectral density (PSD) of a cantilevered beam

Once the PSD, $S_{zz}(\omega)$, has been calculated from the time-series data, $z(t)$, the next step is to identify the eigenfrequencies and associated quality factors. The fluctuation-dissipation theorem is an important result from statistical mechanics that relates the equilibrium thermal fluctuations of an object to the dissipative properties acting on the object. For the case of a classical oscillator, the fluctuation-dissipation theorem states that

$$S_{zz}(\omega) = \frac{2k_BT}{\omega}\mathrm{Im}\{Z(\omega)\}, \tag{3.18}$$

where $S_{zz}(\omega)$ is the power spectral density (PSD) of the mean square fluctuation, k_B is Boltzmann's constant, and T is temperature [55]. For a damped oscillator, $Z(\omega)$ is the FRF given by Eq. 3.11. For thermally-excited oscillations, the PSD is:

$$S_{zz}(\omega) = \frac{2k_BT}{\omega}\mathrm{Im}\left\{\frac{1/k_c}{1-(\frac{\omega}{\omega_o})^2+i\frac{\omega}{Q\omega_o}}\right\} \tag{3.19}$$

$$S_{zz}(\omega) = \frac{2k_BT}{\omega k_c}\mathrm{Im}\left\{\frac{1-(\frac{\omega}{\omega_o})^2-i\frac{\omega}{Q\omega_o}}{\left[1-(\frac{\omega}{\omega_o})^2\right]^2+\left(\frac{\omega}{Q\omega_o}\right)^2}\right\} \tag{3.20}$$

$$S_{zz}(\omega) = \frac{2k_BT}{m\omega_o^3Q}\frac{1}{\left[1-(\frac{\omega}{\omega_o})^2\right]^2+\left(\frac{\omega}{Q\omega_o}\right)^2}, \tag{3.21}$$

where the substitution $k_c = m\omega_o^2$ was used. The units of $S_{zz}(\omega)$ are [m^{2}s], as they should be.

3.3.3 Extension to multimode harmonic oscillators

By Euler-Bernoulli beam theory, a cantilevered beam oscillates in multiple modes. The above derivation of the FRF and PSD assumed that the oscillator had a single mode of oscillation. The point-mass model (single-degree-of-freedom model) is used to extend the derivation of $Z(\omega)$ and $S_{zz}(\omega)$ to multimode oscillations.

In the point-mass model, the frequency response of the cantilever is modeled as that of a damped mass-spring system, as shown in Fig. 3.1. The equation of motion for the jth eigenmode,

which has frequency ω_j, is

$$M_{eq}^j \ddot{z}(t) + C_{eq}^j \dot{z}(t) + K_{eq}^j z(t) = f_j(t), \tag{3.22}$$

where $z_j(t)$ is the tip deflection of the jth eigenmode. The point-mass model of cantilever oscillations is valid for oscillations measured at the free end of the cantilever at frequencies near the eigenfrequencies. In this limit, the equivalent mass M_{eq}^j, equivalent stiffness K_{eq}^j, and equivalent damping C_{eq}^j must be identified.

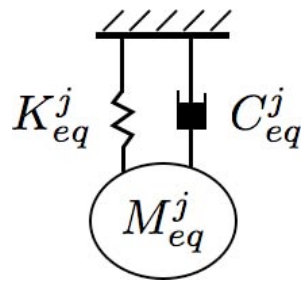

Figure 3.1. A schematic of the the point-mass model for cantilever oscillations assuming a stationary base.

The equivalent stiffness and equivalent mass, are defined as [56]

$$K_{eq}^j = k_c \alpha_j^4 / 12 \tag{3.23}$$

$$M_{eq}^j = m/4. \tag{3.24}$$

The stiffness of the cantilever increases dramatically for higher eigenmodes (eg: $K_{eq}^{j=1}/k_c$ =1.03, $K_{eq}^{j=2}/k_c$=40.5, $K_{eq}^{j=3}/k_c$=317), while the equivalent mass is independent of eigenmode [56]. The damping is unchanged for higher eigenmodes; $C_{eq}^j = c$.

Substitution of K_{eq}^j, Q_j, M_{eq}^j into Eq. 3.12 for the FRF and Eq. 3.19 leads to

$$Z(\omega) = \frac{F(\omega)/K_{eq}^j}{\left[1 - \left(\frac{\omega}{\omega_j}\right)^2 + i\frac{\omega}{Q_j \omega_j}\right]} \tag{3.25}$$

and

$$S_{zz}(\omega) = \sum_{j=1}^{N} \frac{2k_B T}{M_{eq}^j \omega_j^3 Q_j} \frac{\Phi_j^2(x)}{\left[1 - (\frac{\omega}{\omega_j})^2\right]^2 + \left(\frac{\omega}{Q_j \omega_j}\right)^2}. \tag{3.26}$$

where $\Phi_j(x)$ is the cantilever deformation of the jth eigenmode, as defined previously [57].

3.4 Damping and quality factor of cantilevers in fluids

The quality factor Q of an oscillation is proportional to the ration of the energy stored to that dissipated, that is

$$Q = 2\pi \frac{E_{stored}}{E_{diss}}. \tag{3.27}$$

For a linear harmonic oscillator, Eq. 3.27 can be expressed as [58]

$$Q = \frac{k_c + m\omega^2}{2c\omega}; \text{ at resonance, } Q = \frac{m\omega_o}{c}. \tag{3.28}$$

Assuming an ideally cantilevered nanowire (ie: displacement and velocity at the fixed end are zero), mechanisms for the damping of the nanowire's vibrations include c_s, the structural damping due to phonon modes and defects in the nanowire, and c_f, the damping due to the ambient fluid (gas or liquid). The total damping is $c = c_s + c_f$. The fluid damping depends primarily on the diameter of the nanowire and the pressure of the surrounding fluid.

In order to calculate reasonable estimates for Q, c must be known. For fluid damping of nanostructures, $c_f \gg c_s$, so c_s can be neglected. For all the experiments in this report, the surrounding fluid is standard lab atmosphere, at pressures, P, of 760 Torr and lower. In this gaseous environment, three different fluid flow regimes can be applicable for the calculation of c_f, depending on P and the dimensions of the nanowire or Si microcantilever.

3.4.1 Damping in the continuum, cross-over and free-molecular regimes

The effect of fluid damping c_f depends on the dimensions of the cantilever (eg: nano-wire or Si microcantilever) and the density of the surrounding fluid. The Knudsen number, Kn, is a dimensionless parameter that can be used to characterize fluid flow regimes:

$$Kn = l_{mfp}/w_{rep}, \tag{3.29}$$

where l_{mfp} is the mean free path of the gas molecules, 65 nm for air at STP, and w_{rep} is a representative length scale, the width, w, or diameter, d_o, of an oscillating cantilever [58]. The flow regimes are defined as continuum ($Kn \leq 0.01$), cross-over ($0.01 < Kn \leq 10$), and free molecular regime ($Kn > 10$). In the continuum regime, air pressure, P, is considerable and viscous forces act on the cantilever. In the cross-over regime, the air molecules interact slightly with the cantilever. At the low relative pressures of the free molecular regime, the forcing is due solely to momentum exchange of the molecules striking the cantilever and the air-cantilever interactions are described using statistical mechanics [59]. Since the damping c_f depends on the flow regime, it is important to identify the appropriate flow regime.

During the course of this work, the vibration spectra of numerous nanowires and a few standard Si microcantilevers, including the μmasch NSC35, were studied. Diameters of 75 nm and

150 nm are representative of the MWNTs and Ag_2Ga nanoneedles studied; the width of the μmasch NSC35 microcantilever is $w = 35\ \mu$m.

Using these parameters, the Knudsen number is calculated as a function of pressure between 10 mTorr and 1000 Torr (Fig 3.2). The damping of the Si microcantilever spans all three flow regimes in the pressure range plotted, while at atmospheric pressures and below, damping of the nanowire is in the cross-over and free molecular regimes. The cut-off pressure between the cross-over and free molecular regime is 35 Torr and 75 Torr for the 75-nm and 150-nm diameter nanowires, respectively. At atmospheric pressure, silicon microcantilevers are in the viscous continuum regime while nanowires are in the cross-over regime.

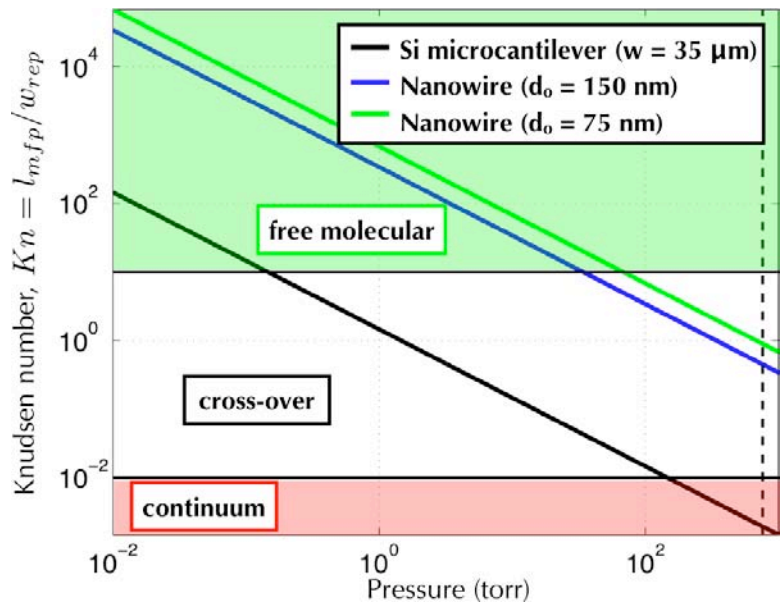

Figure 3.2. Knudsen numbers calculated for the 35-μm wide cantilever and two nanowires of different diameters. Shaded regions indicate the free molecular flow, cross-over, and continuum regimes. The dashed vertical line indicates 760 Torr.

Fluid damping coefficient

The fluid damping coefficient, c_f, is a function of pressure and is given by different expressions in the continuum, crossover, and free molecular regimes. All three expressions for c_f contain a common term equal to $\rho_f U_{th}$, where ρ_f is the gas density and U_{th} is the rms air speed, $U_{th} = \sqrt{\frac{3k_b N_A T}{M_m}}$ [58]. In U_{th}, N_A is Avogado's constant and M_m is the molecular weight of the gas (eg. 29.87 g/mol for Earth's atmosphere) [60]. Using the ideal gas law, the fluid density ρ_f can be

expressed in terms of the gas temperature T and pressure,

$$PV = nR_oT \rightarrow P = \frac{m_{gas}}{V}\frac{R_oT}{M_m} \rightarrow \rho_f = P\frac{M_m}{R_oT}, \tag{3.30}$$

where the universal gas constant is $R_o = N_A k_B = 8.314$ J/(mol K) and m_{gas} is the mass of the gas. Thus the aforementioned common term can be expressed as

$$\rho_f U_{th} = P\sqrt{\frac{3M_m}{R_oT}} \tag{3.31}$$

which appears in the below expressions for c_f. These definitions for c_f in the continuum, cross-over, and free molecular regime are from Ref. [58].

$$c_f = \sqrt{3}[1.41\beta K_c Kn]\, Lw_{rep}P\sqrt{\frac{M_m}{R_oT}} \qquad Kn \leq 0.01, \text{ continuum regime} \tag{3.32}$$

$$c_f = 2\sqrt{3}\,\frac{\pi^{3/2}Kn}{\alpha_{Kn}}\, Lw_{rep}P\sqrt{\frac{M_m}{R_oT}} \qquad 0.01 \leq Kn \leq 10 \text{ cross-over regime} \tag{3.33}$$

$$c_f = \frac{F_d}{u} = 2\sqrt{3}\, Lw_{rep}P\sqrt{\frac{M_m}{R_oT}} \qquad Kn > 10, \text{ free molecular regime.} \tag{3.34}$$

Continuum c_f: The continuum fluid damping coefficient depends on the cantilever's dimensions (L and w_{rep}), the gas properties, and dimensionless parameters β and K_c. K_c, a fluid density parameter, is a function of β and is given in Ref. [58]. The dimensionless parameter $\beta = Re/(4P_w)$ is a function of the Reynolds number, Re, and a frequency parameter $P_w = A_{cant}/w_{rep}$, where A_{cant} is the oscillation amplitude of the cantilever. The Reynolds number is $Re = \rho_f U_{cant}\, w_{rep}/\mu$ where μ is the dynamic viscosity of the fluid (gas) and $U = A_{cant}\omega$ is the oscillation velocity of the cantilever [58].

Cross-over c_f: The cross-over fluid damping coefficient is proportional to the free molecular fluid damping coefficient and depends on the Mach number, Knudsen number, and dimensionless parameter α_{Kn}, where

$$\alpha_{Kn} = ln\left(\frac{2\sqrt{\pi}Kn}{S}\right) - \gamma + 0.5 + \Lambda\sqrt{\pi}Kn. \tag{3.35}$$

The Mach number is $S = U_{cant}/U_{sound}$; γ is the Euler constant, 0.5772; and Λ, which varies between 1 and 1.5 in the cross-over regime, is given by

$$\Lambda = 1 + \frac{1}{2}(1 - e^{-Kn/2}). \tag{3.36}$$

Free molecular c_f: The free molecular fluid damping coefficient is independent of Knudsen number and depends linearly on the cantilever dimensions and pressure. The free molecular fluid damping is proportional to the drag force F_d and a velocity term u.

The non-dimensionalized fluid damping coefficients, $c_f/(\pi\mu L)$, are plotted in Fig. 3.3 for the Si microcantilever and two nanowires. As defined previously, L is the length of the cantilever or nanowire and μ is the dynamic viscosity, $\mu = 0.45\sqrt{3}l_{mfp}P/\sqrt{R_oT}$ [58].

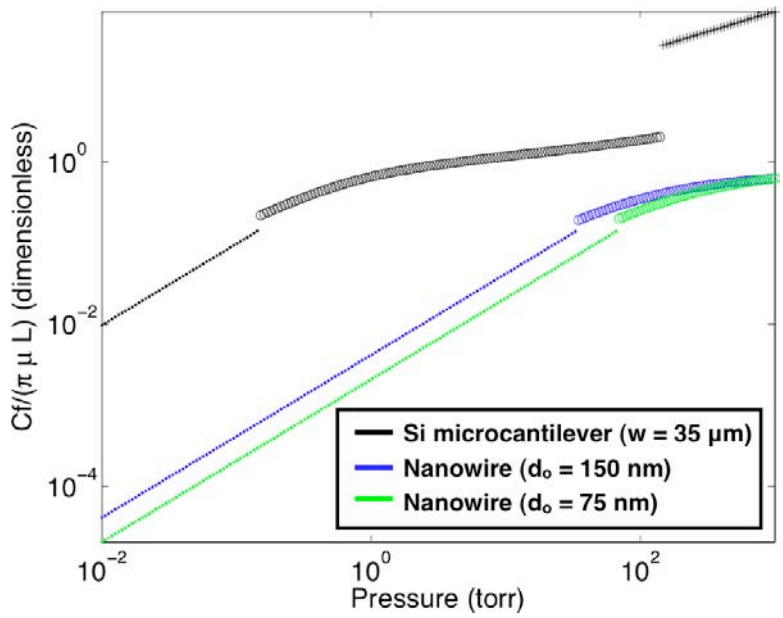

Figure 3.3. The non-dimensionalized fluid damping coefficients are plotted for the three cantilevers for the case of free molecular (·), cross-over (o), and continuum (+) flow regimes. The cross-over solution underestimates the cross-over damping, resulting in a discontinuity between the cross-over (0) and continuum flow (+) regimes.

3.4.2 Calculated quality factor due to gas damping at atmospheric pressure

Following Eq. 3.28, the quality factor of the jth eigenmode is

$$Q_j = \frac{m\omega_j}{c_f + c_s}; \tag{3.37}$$

when $c_f \gg c_s$, Q_j is inversely proportional to c_f.

Equation 3.37 and the expression for c_f in the cross-over regime are used to calculate Q at 760 Torr for nanowires of $L = 10\ \mu$m, d_o = 100–200 nm. For MWNTs of these dimensions, Q_1 = 3–18; for Ag_2Ga nanoneedles of these dimensions, Q_1 = 10–60. The above expressions for c_f and Eq. 3.37 are used in the calculation of the minimum detectable mass for cantilevered nanowire sensors (section 5.5).

Chapter 4

Experimental details for measurements of the vibrational spectra of nanowires

4.1 Polytec MSA-400 scanning vibrometer

Nanowire oscillations were recorded using a Polytec MSA-400 scanning LDV. To reduce noise from flood vibrations, the LDV is situated directly on top of a 30,000 kg cement slab supported by six air spring dampers. The vibrometer consists of a modified Mach-Zehnder interferometer with an optical microscope in the signal leg of the vibrometer. The object beam of the interferometer (wavelength λ=633 nm, power <1 mW) is focused through a microscope objective and is incident normal to the vibrating nanowire. As shown in Fig. 4.1(a), the backscattered beam is recombined with a reference beam to form an interference signal which is decoded and Fourier transformed to yield the vibrational spectra of interest. The LDV can measure velocities in the spectral range from 0–1.5 MHz and displacements in the spectral range from 50 kHz–20 MHz. The frequency resolution is 100 Hz for a typical 0-10 MHz frequency scan, allowing for a high resolution of spectral features.

In the case of the displacement spectra measurements, the backscattered beam is phase-shifted due to the change in the position of the nanowire as it vibrates. When the phase-shifted backscattered beam is recombined with the reference beam, the resulting interference pattern is decoded using a fringe-counting method. The velocity spectra measurements were decoded using the well-known Doppler effect. The nanowire's oscillatory motion with amplitude A and velocity v at frequency f caused the backscattered light, which the LDV collects, to be Doppler shifted by a frequency

$$\Delta(t) = \nu' - \nu = -\frac{\mathsf{v}}{c}\nu\, cos(2\pi f t), \tag{4.1}$$

where $\mathsf{v} = \mathsf{A}(2\pi f)$ and $\nu = c/\lambda$, where c is the speed of light. When the Doppler frequency shift is measured at an eigenmode of the MWNT, $\Delta(t)$ is proportional to the resonant frequency f_j and amplitude A_j of the jth eigenmode. Numerous tests of the LDV show that the frequencies are measured with high accuracy.

However, the measured amplitude of the LDV is only proportional to the actual displacement or velocity. When *most* of the reflected beam is collected by the sensor, the error between the measured and actual amplitude is small (<10 percent). If only a small percentage of the reflected beam

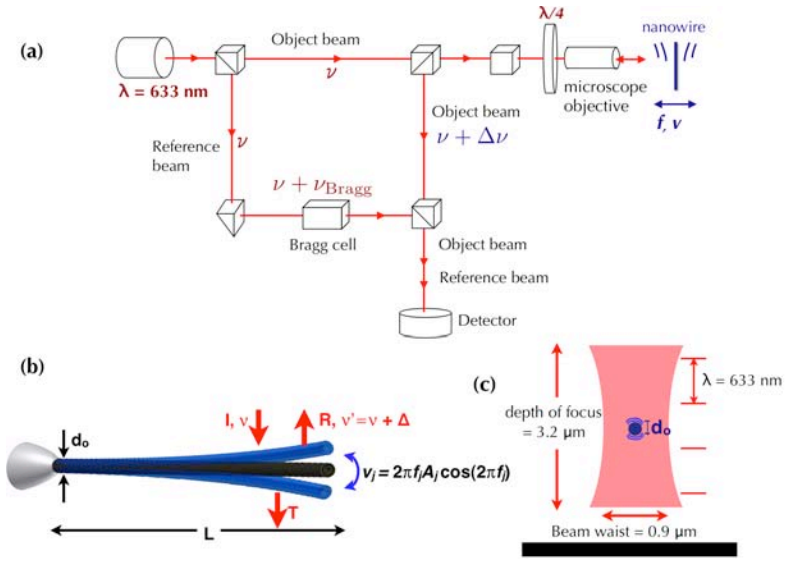

Figure 4.1. In (a), a schematic of the Polytec LDV used in this work, following Ref. [14]. The circularly polarized laser beam is split by a beamsplitter into an object and reference beam. The object beam is focused through a 50× objective onto the vibrating nanostructure, usually a nanowire. This backscatted object beam is then recombined with the reference beam, whose frequency has been shifted by $\nu_{Bragg} = 40$ MHz. In (b), a schematic diagram of a cantilevered nanowire. The reflected light (R) of the normally incident laser beam (I) is Doppler shifted by frequency Δ when reflected from the MWNT. In (c), an illustration of the relative dimensions when the object beam is focused through the 50× objective. As indicated by the shaded region, the beam waist is much wider than the nanowire.

is collected by the sensor (small signal return), then the measured signal is only *proportional* to the local displacement or velocity of the nanowire and a quantitative estimate of the local velocity or amplitude becomes problematic, even though the frequencies are accurately measured. Small signal returns occur (a) when the LDV laser spot lies on the edge of a vibrating structure or (b) when the vibrating object is much smaller than the spot size of the beam.

Figure 4.2(b) shows the measured operating deflection shape (ODS) of the first eigenmode of vibration of an Ag_2Ga nanoneedle, which was measured at 13 points along the nanoneedle. The measured ODS corresponds well to the theoretical first eigenmode of vibration for all but the tip-most data point. The displacement of this tip-most data point is only 75 percent of the expected value, which was normalized to unity. The under-measurement of the displacement indicates that the LDV laser spot likely lay on the very end of the nanoneedle, as indicated by the red circle

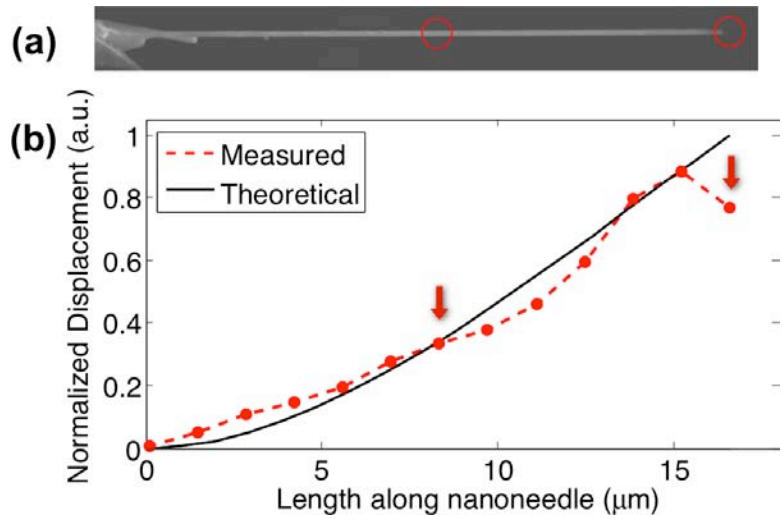

Figure 4.2. In (a), an SEM of the 16.6 μm long, 140 nm diameter nanoneedle *NNB*2. Two red circles, diameter 0.9 μm, indicate the spot size of the laser. In (b), the measured ODS and theoretical first eigenmode, both normalized. The laser return at the tip-most point on the nanoneedle was poor; for this reason the last data point under-estimates the displacement amplitude.

drawn on the tip of *NNB*2 in Fig. 4.2(a).

Since the MWNTs were relatively poor light scatters, all MWNT displacement and velocity spectra were normalized to a maximum value of unity. Spectra from Ag_2Ga nanoneedles and Si cantilevers are presented with the measured amplitude reported by the LDV, which may differ from the actual amplitude.

4.2 Calibration of LDV by measuring the thermal tuning curve of a Si microcantilever

As mentioned above, the LDV output is proportional to the local displacement or velocity. To check that that measured amplitude of the LDV is reasonably accurate, the thermal spectra of a conventional silicon microcantilever was measured. By the equipartition theorem (section 4.2.1), the thermal energy is equally divided between the potential energy and kinetic energy. The potential energy, $E_{potential}$ is proportional to the spring constant of the cantilever, k_c, and mean square displacement, $\langle z^2 \rangle$.

$$\frac{1}{2}k_B T = \frac{1}{2}k_{LDV}\langle z^2 \rangle = \frac{1}{2}k_{AFM}\langle z^2 \rangle, \tag{4.2}$$

where k_{LDV} and k_{AFM} are k_c estimated from Sader's method using the LDV and AFM spectra respectively. Sader's method (section 4.2.2) gives a method of measuring k_c from the quality factor and frequency of the resonant peak of a cantilever oscillating in a fluid of known density and damping. If the LDV calibration is accurate, then the measured $E_{potential}$ should equal $E_{thermal}$, assuming the cantilever is in thermal equilibrium with the surrounding atmosphere.

The vibration spectrum of a silicon AFM cantilever was measured using both the LDV and the Nanotec Electronica AFM. For both measurements, k_c was estimated from the vibration spectra using Sader's method. Using these k_c and the mean $\langle z^2 \rangle$ measured by the LDV, $E_{potential}$ was calculated and compared to $E_{thermal}$. The experimental details of these measurements are given in section 4.2.1; the calculated energies are given in Table 4.1.

4.2.1 Experimental details

Asylum Si_3N_4 microcantilever: An Asylum Research RC800 PSA silicon nitride microcantilever was studied. The manufacturer dimensions are $L = 100\,\mu$m and $w = 20\,\mu$m with a nominal k_c = 0.39 N/m. These dimensions were confirmed by measurements with the LDV's 50× optical microscope. This cantilever was chosen since it had a small nominal spring constant and a rectangular cross-section.

Nanotec AFM: The cantilever was mounted in the Nanotec chip holder and its tuning curve was measured using the Nanotec Electronica AFM. The drive voltage for this measurement was 0.02 V. The measured tuning curve and the associated curve fit for the frequency response function (FRF) are plotted in Fig. 4.3(a).

Polytec LDV: The cantilever, still in the Nanotec chip holder, was then mounted in the field of view of the LDV. The Nanotec chip holder, held securely in the jaws of an alligator clip, was positioned using an XYZ micromanipulator. This arrangement allowed the LDV's signal beam to be focused on the flat side of the cantilever. For these calibration tests, the laser spot of the LDV was focused fully on the end of the cantilever. Since the signal return was maximum, the measured amplitude was as accurate as possible using the LDV.

The displacement as a function of time, $z_{meas}(t)$, was measured at the free end of the cantilever. The displacement was measured at 1,048,576 time points over 4.096 sec, resulting in a time resolution of $\Delta t = 3.9\,\mu$s. By the Nyquist criterion, $2f_{Nyquist} = 1/\Delta t$, the minimum measurable frequency $f_{Nyquist}$ was 128 kHz.

Using the PWelch algorithm detailed in Appendix E, the power spectral density (PSD) of the displacement $z_{meas}(t)$ was calculated. This PSD is plotted in Fig. 4.3(b); averaging over 64 frequency windows smoothes the data. To determine Q and f_1, the following curve fit,

$$S_{zz}(f) = \frac{A}{Q_1 f_1^3} \frac{1}{\left[1 - (\frac{f}{f_1})^2\right]^2 + \left(\frac{f}{Q_1 f_1}\right)^2} + Noise, \tag{4.3}$$

which is of the form of Eq. 3.19, was fit to the PSD (64 windows) using Matlab's curve fitting

toolbox (cftool). In Eq. 4.3, the term A includes the parameters of temperature and cantilever mass; *Noise* is a small constant offset.

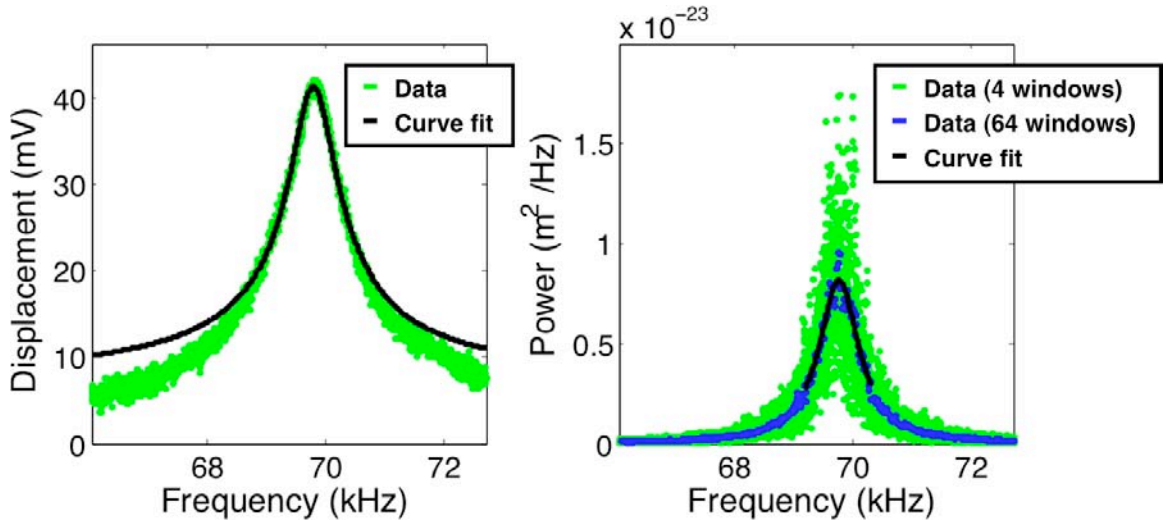

Figure 4.3. (a) The FRF of a Si_3N_4 cantilever, as measured using the Nanotec AFM. (b) The power spectral density measured using the LDV for the same Si_3N_4 cantilever. This figure shows the effect of averaging the PSD over 4 (green) and 64 (blue) windows. A curve fit (black) is fit to the 64-window data.

4.2.2 k_c from Sader's method for AFM and LDV data

Sader's method is regularly used to calibrate the static bending stiffness k_c of AFM cantilevers and is implemented in a Nanotec AFM. Assuming a rectangular cantilever of width w, the static bending coefficient k_c is then

$$k_c = 0.1906\rho_f w^2 L Q_f \Gamma_i(\omega_o)\omega_o^2, \tag{4.4}$$

where ρ_f is the density of the surrounding fluid, Q_f is the quality factor of the cantilever's oscillation in fluid, Γ_i is the imaginary part of the hydrodynamic damping function, and ω_o is the fundamental resonant frequency, also measured in fluid [61].

Ryan Wagner measured the tuning frequency response function (FRF) [Fig. 4.3(a)] using the Nanotec Electronica AFM. From a curve fit to the FRF (Eq. 3.13), we determined $f_1 = 69.81$ kHz and $Q = 89$. Using Sader's method and the measured quantities and cantilever dimensions given above, we calculated $k_c = 0.32$ N/m.

For the LDV data, $Q = 86$ was determined by the curve fit of Eq. 4.3 to the PSD, which was calculated using 64 windows. From this Q, $k_c = 0.31$ N/m was calculated using Sader's method. Thus the calculated k_c from the AFM tuning curve and the LDV PSD are in good agreement.

4.2.3 Calculation of $\langle z^2 \rangle$ from $z_{meas}(t)$ and from the PSD

From the LDV measurement, the mean square displacement $\langle z^2 \rangle$ of the cantilever can be calculated either directly from $z_{meas}(t)$ or indirectly from the PSD. By Parseval's theorem, the total energy of a signal in the time and frequency domain are equal; that is,

$$\int_{-\infty}^{\infty} dt\, h^2(t) = \int_{-\infty}^{\infty} df |H(f)|^2, \tag{4.5}$$

where $h(t)$ and $H(f)$ are a Fourier transform pair [62].

The deflection at the tip of the cantilever, $z_{meas}(t)$ was measured using the displacement decoder of the LDV. After correcting for the offset, the mean deflection in the time domain $\langle z^2_{time} \rangle = 0.0105 \times 10^{-18}$ m^2 was calculated. This calculation assumes that the deflection of the cantilever at its tip is due solely to the motion of the first eigenmode, z_1. While $z_{meas} > z_1$, the mean square deflection of the first eigenmode is 39 times that of the second ($\langle z_1^2 \rangle / \langle z_2^2 \rangle = \alpha_2^4 / \alpha_1^4 = 6.27^4$), so the assumption that $\langle z^2_{time} \rangle \equiv \langle z_1^2 \rangle$ is accurate to 2 percent.

A better measure of the energy in a single eigenmode is calculated by integrating the PSD. From Eq. 4.5, $\sum_{\text{all modes}} \langle z^2_{freq,\,j} \rangle$, the mean square deflection in the frequency domain, should equal $\langle z^2_{time} \rangle$. From the PSD, $\langle z^2_{freq,\,j} \rangle$ is calculated by numerically integrating (trapezoidal integration) the PSD over the width of the eigenmode. $\langle z^2_{freq,\,1} \rangle = 0.0094$ nm^2 was calculated by integrating the PSD over a frequency range of 5 kHz, which was centered at f_1 = 69.81 kHz. The value of $\langle z^2_{freq,\,1} \rangle$ should be more accurate than the value of $\langle z^2_{time} \rangle$ because $\langle z^2_{freq,\,1} \rangle$ only contains contributions from the first eigenmode.

4.2.4 Comparison of the potential and thermal energy of a Si_3N_4 cantilever in thermal equilibrium

Following Eq. 4.2, the potential energy can now be calculated as $\frac{1}{2} k_c \langle z^2 \rangle$, where k_c is determined by AFM or LDV. Assuming a room temperature of 293 K, $E_{thermal}$ is given by $(1/2) k_B T$, which is equal to 2.02×10^{-21} J.

The calculated $E_{potential}$, as calculated using k_c measured from the AFM and LDV, are given in table 4.1. The error in the measurement is defined as $(E_{thermal} - E_{potential}/E_{thermal})$. The error of the measured $E_{potential}$ is 25 percent, which suggests that the measured $\langle z^2 \rangle$ is ~25 percent too small. The measured Si_3N_4 cantilever is an uncoated cantilever and likely has poor reflectivity.

Table 4.1. Potential energy of a Si_3N_4 cantilever, using $\langle z^2_{freq} \rangle$ = 0.0094 nm^2 and $K^1_{eq} = \alpha^4_1 k_c/12$. The Q is determined from the curve fit to either the AFM or LDV data.

Method	Q	K^1_{eq} (N/m)	$E_{potential} \times 10^{-21}$ J	% Error
AFM	89	0.33	1.6	23
LDV	86	0.32	1.5	26

4.3 The MWNT-Ni STM tips

The MWNTs used in this experiment were grown at 900 ^{o}C in a SEKI AX5200S microwave PECVD reactor using Fe_2O_3 nanoparticle catalyst particles [63]. These MWNTs were grown by Dr. Placidus Amama of Prof. Tim Fisher's research group at Purdue University. Chun Lan of the Reifenberger Nanophysics Lab had studied the electronic properties of PECVD-grown MWNTs as a function of growth conditions. She discovered that MWNTs grown at 900°C had a lower resistance and, thus fewer defect sites, than MWNTs grown at 800°C or 900°C [64].

4.3.1 Literature review of affixing MWNTs to AFM tips

The techniques used for affixing MWNTs to STM tips strongly follow the procedure used for creating MWNT-AFM probes. In 1996 Dai et al. reported affixing MWNTs to both silicon cantilevers and STM tips using an acrylic adhesive and van der Waals force. Although they reported atomic resolution STM scans of TaS_2 using a ∼5-nm wide MWNT protruding from a MWNT bundle [65], future work from this group and others focused on MWNT-AFM probes.

Researchers at NASA Ames Research Center realized the potential of Ni-coated cantilevers for fabricating MWNT-tipped AFM probes and developed a technique for transferring a single MWNT to a probe tip using micromanipulators [66]. Using carbon vapor deposition (CVD), a cartridge of MWNTs was grown on a PtIr wire in preparation for the MWNTs' transfer to silicon cantilevers coated with ∼10–15 nm of nickel. The MWNT cartridge and Ni-coated cantilever, held by micromanipulators, were brought into close proximity under an optical microscope. When a solitary MWNT suitable for transfer was found, a small electric field (3–10 V) was applied between the cartridge (anode) and cantilever (cathode) to induce the MWNT to contact the cantilever. Then the voltage was increased to 10–40 V causing the MWNT to break from the cartridge and weld to the Ni-coated cantilever by current-induced joule heating [66, 67]. These MWNT-AFM probes are extremely stable; no degradation in AFM scan quality was seen after scanning continuously for 15 hours [68].

4.3.2 Creating MWNT-Ni STM tips

Etching Ni tips

The nickel wires were etched into high-aspect ratio STM tips using an electrochemical tip fabricator, Schrödinger's Sharpener (Model SS02, manufacturer Obbligato Objectives). The Schrödinger's Sharpener consists of a clamp to hold the wire being etched, a dual platinum ring assembly which supports the etching laminar, and a detection system with an electronic current break. The nickel wire, held vertically by the anode clamp, extends through the dual ring assembly. Etching occurs in the top ring (cathode) of the coaxial dual ring assembly. The detection system monitors current through the bottom sense ring, cutting off the current and stopping the etch as soon as the wire is etched through.

A nickel wire is cut to a length of 5–6 cm and clamped in the Schrödinger's Sharpener. Then the dual ring assembly and wire are dipped in the etchant, a 2M solution of KCl dissolved in Birck ultra-pure water. Often the rings and wire must be dipped a few times before a stable laminar film forms on both rings. Next a small ball of Play-Doh ($\sim$5 mm diameter) is slid on the free end of the nickel wire. The extra weight of the Play-Doh helps ensure that the tips from both the top and bottom halves of the wire are sharp, avoid torque at the tip etch point, and stop corrosion of the lower tip by causing it to fall as soon as etching is complete [69]. An added benefit is that the Play-Doh ball protects the lower tip as it falls, decreasing the probability that the lower tip will be bent on impact. The Schrödinger's Sharpener control electronics apply a 2.0 V_{DC} voltage and etching begins with the following chemical reaction [69],

$$\text{Cathode: } 2H_2O + 2e^- \rightarrow H_2(g) + 2OH^-$$
$$\text{Anode: } Ni(s) + 4Cl^- \rightarrow NiCl_4^2 + 2e^-.$$

As the etching proceeds, green $NiCl_4^2$ salts accumulate along the Pt ring. Occasionally the laminar in either ring breaks before the etching is completed. In that case the Play-Doh ball is removed, the rings and wire are again dipped in etchant, the Play-Doh ball is replaced, and the etching voltage applied again. To etch a good pair of Ni-STM tips typically required 5–10 minutes. After etching is complete, the tips are held in an ultrasonic bath of Birck ultra-pure water for a minute to remove salts and then rinsed with isopropanol to remove oils.

Affixing MWNTs to Ni-STM tips

Individual MWNTs were affixed to etched nickel STM tips using the procedure described by Stevens *et al.* [66]. This procedure was observed under a darkfield microscope (Zeiss Jenoptik D-07739), which has 5x and 50x magnification. A pair of XYZ nanomanipulators hold the Ni-STM tip and the MWNT cartridge above the microscope stage. To prepare the MWNT cartridge, a small ($\sim 3 \times 3$ mm) piece of conducting SEM tape is held in a alligator clip so that it barely protrudes past the end of the clamp. The SEM tape is then dipped in a sample of matted MWNTs. The mats of MWNTs are gently brushed off, leaving MWNTs stuck in the SEM tape at random directions.

To make the MWNT attachment more robust, the Ni tip is touched to soft double-sided carbon scanning electron microscope (SEM) tape (STR tape from Shinto Paint Co. Ltd.) before adding the MWNT. A small amount of adhesive from the SEM tape sticks to the Ni tip and helps affix the MWNT. Without the adhesive from the SEM tape, the forces of adding a glass bead to the MWNT would frequently push the MWNT off the Ni tip.

Under the 5x magnification, the MWNT cartridge and Ni-STM tip are brought a few hundred microns of each other. The magnification is increased to 50x and MWNT cartridge is scanned to find a solitary MWNT sticking out roughly perpendicular to the cartridge. The desired MWNT is brought into focus and the Ni-STM tip is brought within close proximity using the nanomanipulators. The shallow focal plane of the darkfield microscope ensures that if both the MWNT and Ni-STM tip are in focus, they must be in the same plane. The Ni-STM tip is then brought alongside the MWNT with 5–10 μms of overlap. At this point van der Waals attraction causes the MWNT to snap in contact with the Ni-STM tip. The Ni-STM tip position is adjusted slightly, if necessary, so that the MWNT contacts the Ni-STM tip along the tip's length and not just at one point. An HP 6234A Dual Power Supply, applies a 10–30 V voltage pulse to the MWNT (anode) and Ni-STM tip (cathode). This voltage pulse breaks the MWNT off of the SEM tape and firmly bonds the MWNT to the Ni-STM tip. Figure 4.4 is a darkfield image of a typical MWNT-Ni STM tip.

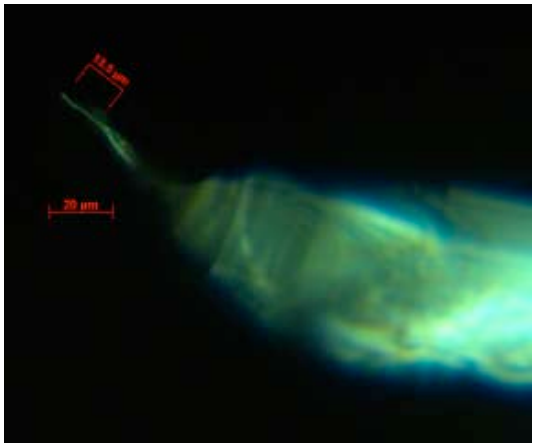

Figure 4.4. Darkfield image of a 13.5 μm MWNT affixed to a nickel STM tip. The magnification is 50x.

4.4 Ultimate measurement limits for LDV calculated using Mie scatting theory

When a cylinder (such as a nanowire) is illuminated by light, the amount of light scattered and absorbed depends in a complicated way on the geometry and optical properties of the cylinder, the index of refraction of the surrounding medium, and the wavelength and polarization of the

incident light beam. When the incident wavelength becomes comparable to the dimensions of the cylinder, Mie scattering theory rather than geometrical optics is applicable. In Mie theory, the scattering cross section per unit length of the cylinder, C_{sca}, depends on the diameter of the cylinder d_o, the complex index of refraction of both the cylinder (N) and surrounding medium (N_{med}), and the wavelength (λ) and angle of incidence of the light beam. From these parameters, expressions for C_{sca} far from the cylinder can be derived [70]. A particularly useful quantity is the scattering efficiency $\mathscr{Q}_{sca}$, which is defined as $\mathscr{Q}_{sca} = C_{sca}/d_o$. If $\mathscr{Q}_{sca}$ is greater than 1, then light is effectively scattered from an apparent object that is larger in cross-section than the actual scattering object.

Following Bohren and Huffman [70], $\mathscr{Q}_{sca}$ is calculated for the case of light (of wavenumber k) normally incident on a cylinder,

$$\begin{aligned} \mathscr{Q}_{sca}^{TM} &= \tfrac{2}{\chi}(|b_o|^2 + 2\textstyle\sum_n^\infty |b_n|^2) \\ \mathscr{Q}_{sca}^{TE} &= \tfrac{2}{\chi}(|a_o|^2 + 2\textstyle\sum_n^\infty |a_n|^2), \end{aligned} \tag{4.6}$$

where the dimensionless size parameter, χ, equals ka [70]. In the case of circularly polarized light, the transverse magnetic (TM) and electric (TE) modes contribute equally, so $\mathscr{Q}_{sca} = \frac{1}{2}(\mathscr{Q}_{sca,TM} + \mathscr{Q}_{sca,TE})$ [71]. The coefficients a and b are a function of the ratio of the index of refraction of the surrounding medium (N_{med}) to that of the cylinder (N_{cyl}) and the size parameter x.

$$\begin{aligned} a_n &= \frac{\eta J_n'(\chi) J_n(\eta x) - J_n(\chi) J_n'(\eta x)}{m J_n(\eta\chi) H_n^{(1)'}(\chi) - J_n'(\eta\chi) H_n^{(1)}(\chi)} \\ b_n &= \frac{J_n(\eta\chi) J_n'(\chi) - \eta J_n'(\eta\chi) J_n(\chi)}{J_n(\eta\chi) H_n^{(1)'} - \eta J_n'(\eta\chi) H_n^{(1)}(\chi)}, \text{ where } n = 0, 1, 2, ... \end{aligned} \tag{4.7}$$

where H_n^1 is a Hankel function ($H_n^1 = J_n + iY_n$), J_n and Y_n respectively are Bessel functions of the first and second kind, and $\eta = |N_{cyl}|/|N_{med}|$.

We use Mie theory to calculate the scattering efficiency $\mathscr{Q}_{sca}$ of graphite, silver, and silicon nanowires, which are modeled as dielectric cylinders of diameter d_o. This calculation allows us to better understand the limits of light scattering from a nanowire and to estimate the smallest diameter nanowire whose oscillation might be detected. A FORTRAN program for calculating $\mathscr{Q}_{sca}$ as a function of incident angle was modified to calculate $\mathscr{Q}_{sca}$ as function of d_o, N, and N_{med} [70]. This modified FORTRAN program and a sample output are given in Appendix D. Calculations of $\mathscr{Q}_{sca}$ are plotted in Fig. 4.5 and were performed for the case of circularly polarized 633-nm light to match the conditions of our experiments.

Optical constants for MWNTs and Ag_2Ga nanoneedles are not well established. However, a MWNT is similar in structure to pyrolitic graphite for which the optical constants are known. With this in mind, any light reflected from the front surface of a MWNT scatters from graphitic planes similar in orientation to the [0001] basal plane of graphite. Any light scattered from the outer edge of a MWNT reflects from graphitic planes similar in orientation to the $[11\bar{2}0]$ plane of graphite. Following this logic, realistic limits on $\mathscr{Q}_{sca}$ can be obtained using the appropriate optical constants of pyrolytic graphite [72]. The index of refraction for silver ($N_{Ag} = 0.135 + i3.99$) is used as a rough approximation for the N of Ag_2Ga nanoneedles [73].

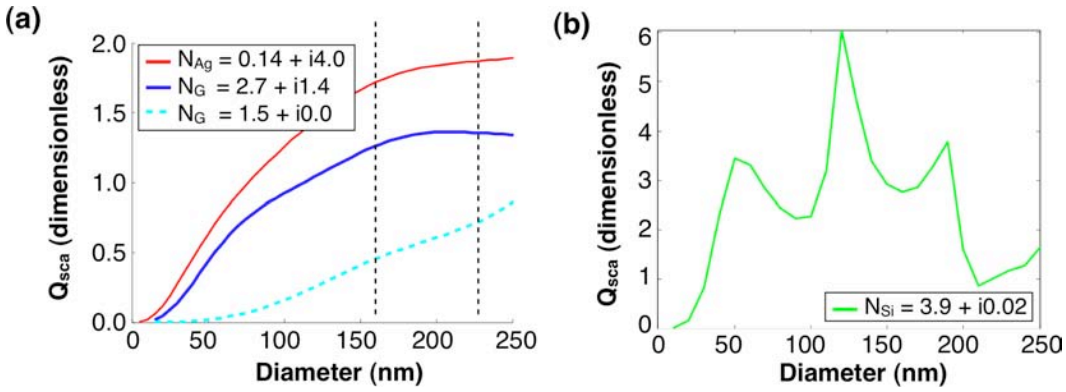

Figure 4.5. The calculated $\mathscr{Q}_{sca}$ for circularly polarized 633 nm light normally incident on a cylindrical nanowire in air as a function of diameter. In (a), the case of light scattering off of metallic silver ($N_{Ag} = 0.135 + i3.99$; solid red line) and graphitic nanowires. For the graphitic nanowires, light scattering off the [0001] plane ($N_G = 1.5 + i0$; dotted cyan line) and the $[11\bar{2}0]$ plane ($N_G = 2.7 + i1.4$; solid blue line) are considered. The diameters of MWNTs studied fall within the range indicated by the dashed vertical lines. In (b), the case of light scattering off of a semiconducting silicon nanowire ($N_{Si} = 3.877 + i0.019$).

We conclude from Fig. 4.5(a) that for diameters less than ~250 nm, the edges of the MWNT will more effectively scatter light. Assuming that the signal-to-noise ratio (*SNR*) of the vibrational resonance peak is proportional to the amount of light scattered, we can estimate the smallest diameter MWNT that reflects just enough light so that its oscillation might be detected. From our measured data, we typically find a *SNR* at resonance of 5:1. We define the smallest diameter MWNT whose oscillation spectra can be measured as a MWNT that scatters light at resonance with a *SNR* of 1:1. From the calculations leading to Fig. 4.5(a), we estimate that MWNTs with diameters between 70 and 100 nm meet the *SNR* criterion of 1:1. This suggests that MWNTs with diameters in the range between 70 and 100 nm are the smallest diameter MWNTs that can be studied using the Polytec MSA-400 scanning LDV. To date, the smallest diameter Ag_2Ga nanoneedle studied had a diameter of 60 nm. This nanoneedle still reflected sufficient light so that its oscillation spectra could be recorded.

Since $\mathscr{Q}_{sca}$ depends strongly on the index of refraction N of the cylinder, nanowires of other materials might scatter light more effectively, thereby allowing the vibrational spectra of smaller diameter nanowires to be detected. Consider the case of Si(111) nanowires which have $N = 3.9 + i0.02$ [74]. Calculations give a $\mathscr{Q}_{sca}$ one to two orders of magnitude higher than MWNTs of the same diameter, suggesting that the oscillation of silicon nanowires can be measured to diameters less than 50 nm [Fig. 4.5(b)].

Chapter 5

Measured vibration spectra, elastic modulus, and quality factors of MWNTs and Ag_2Ga nanoneedles

5.1 Qualitative MWNT vibration spectra

Our first experiments to measure the vibration spectra of MWNTs were low-resolution qualitative measurements to estimate the resonant frequency of individual MWNTs. [1] *A priori* we had assumed that the elastic modulus of the PECVD-grown MWNTs was ∼1 TPa, as it is for SWNTs and pristine arc-discharge MWNTs. Using E=1 TPa and approximate MWNT dimensions of 5-10 μm, d_o = 100 nm, and $d_i = 0.5d_o$, the resonant frequency was estimated to be in the 10s of MHz.

To obtain rough estimates for f_1, we electostatically excited MWNTs affixed to nickel STM tips and observed the oscillation in a darkfield microscope. The design of the electrostatic excitation experiment was inspired by the work of J. Galliard *et al.* [34] and by conversations with Dr. Steve Howell of Sandia National Laboratories. Both the MWNT, mounted on a Ni STM tip, and an etched Ni STM tip counter electrode were held in alligator clips. Using nanomanipulators, the MWNT and counter electrode were positioned nearly perpendicular to each other, approximately 2–4 μm apart, as shown in Fig 5.1(a). This perpendicular configuration was chosen to maximize the electric field on the MWNT. Care was taken to ensure that the gap distance was large enough to prevent the MWNT from snapping into contact with the MWNT; such contact would cause the MWNT to spark shorten.

The MWNT tip was biased by 30 V_{DC} to draw charge to the tip of the MWNT. A DC bias applied between the MWNT and electrode caused the MWNT to bend toward the Ni electrode. If the point of attachment were weak, the MWNT would pivot at MWNT-Ni tip junction. As the electrostatic drive frequency was increased, the magnitude of the oscillation was monitored in the darkfield microscope. At low excitation frequencies (∼2-20 Hz), the MWNT would oscillate with amplitude 1–2 μm. As the drive frequency was increased past ∼50 Hz, the amplitude of oscillation decreased to near zero. The frequency response remained flat until the drive frequency approached

[1] Portions of this chapter were previously published in Ref. [75], L. B. Biedermann, R. C. Tung, A. Raman, and R. G. Reifenberger, "Flexural vibration spectra of carbon nanotubes measured using laser Doppler vibrometry," *Nanotechnology* 20:3 035702 (2009). Please see the copyright statement in Appendix F.

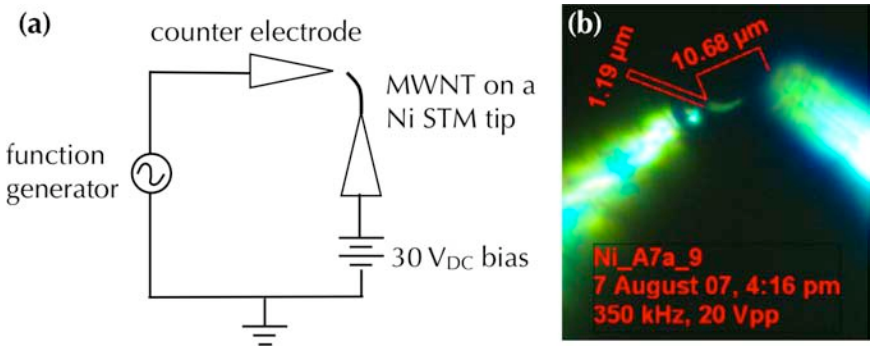

Figure 5.1. In (a), a schematic of the experimental set-up for electrostatic excitation of a MWNT. In (b), the electrostatic excitation of MWNT $A7a-9$ at resonance. The E for this MWNT was calculated to be 4.1 GPa.

the resonant frequency. At resonance, the approximate vibration amplitude was 1–2 μm with a drive voltage of 20 V_{pp}, as shown in Fig. 5.1(b).

The oscillation amplitude depends strongly on the distance between the MWNT and the counter-electrode to which the AC electric potential was applied. Decreasing the MWNT-electrode distance increased both the oscillation amplitude and the risk of the MWNT contacting the electrode and spark shortening. We noted the resonant frequency by an increase in the oscillation amplitude, but the resolution of our frequency measurements was low, ~50 kHz.

Figure 5.2 shows the calculated E for seven MWNTs whose resonant frequencies were estimated using electrostatic excitation. By inverting Eq. 3.7, E is written as

$$E = \frac{(8\pi)^2\rho}{\alpha_j^4(d_o^2+d_i^2)} f_j^2 L^4. \tag{5.1}$$

For these calculations of E, d_o was assumed to be 180 nm and $d_i = 0.5d_o$. Two MWNTs, $A7a-2$ and $A7b-2$, had exceptionally low moduli of 0.2 and 1.1 GPa respectively. These two MWNTs showed an unusually high degree of freedom at the attachment point to the Ni STM tip and are thus excluded from the calculation of the average E. The average E for the remaining five MWNTs was 17 GPa with a standard deviation of 17 GPa. Despite the low frequency resolution of this method, these electrostatic excitation experiments clearly demonstrated that the E for PECVD-grown MWNTs was much lower than we originally assumed. Furthermore, the wide resonance peak indicated that the quality factor of these oscillations was low.

5.2 Quantitative MWNT spectra measured using LDV

In order to accurately determine E of PECVD-MWNTs, we used a laser Doppler vibrometer to measure their thermal vibration spectra. This work was done in collaboration with Ryan Tung

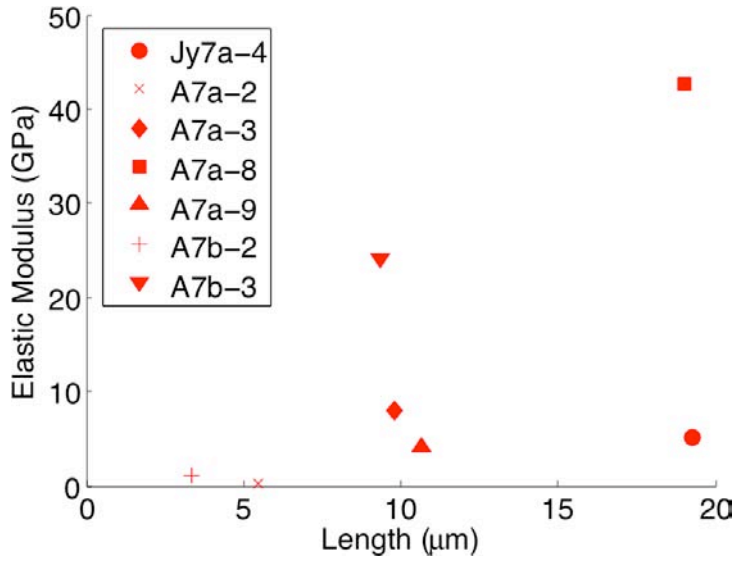

Figure 5.2. The E calculated for seven PECVD-MWNTs based on the resonant frequencies measured in the electrostatic excitation experiments. Lengths were measured in the darkfield microscope; d_o was estimated to be 180 nm for all MWNTs.

and Prof. Arvind Raman of the School of Mechanical Engineering at Purdue. As described in section 4.1, the high frequency resolution (100 Hz) of the LDV allows accurate measurements of the vibration spectra, and thus determination of the elastic modulus.

The vibrational spectra of both bare MWNTs and MWNTs with glass beads affixed to the end were recorded. While the diameters (176 and 230 nm) of the bare MWNTs studied were well above the theoretical small diameter limit predicted by Mie scattering (section 3.6), identifying and focusing the laser beam on such small structures was difficult. MWNTs with glass beads affixed to the end had greater laser signal return and were easier to focus in the 50× bright-field optical microscope.

For each MWNT studied, 5-10 thermal oscillation spectra were acquired and averaged to produce a resultant spectrum that was used for further analysis. For each MWNT, a background spectrum with the laser beam focused on the Ni tip was also acquired. The mass of the Ni tip was great enough that there should be no measurable thermal oscillations and indeed, measurements of a background spectra were uniformly featureless.

After the thermal vibration spectra from an individual MWNT were recorded, the MWNT dimensions (L, d_o, and bead diameter, d_{bead}, if applicable) were measured using a Hitachi S-4800 field emission scanning electron microscope (FESEM). The inner diameters, d_i, were assumed to be $d_i = 0.5d_o$. This assumption was based on parallel studies of TEM micrographs of representative MWNTs.

The eigenfrequencies and corresponding quality factors, Q_{meas}, of the MWNTs (both bare

MWNTs and MWNTs with beads) was found by fitting the measured resonance to Eq. 5.2, which is of the same form as Eq. 3.13,

$$Z(\omega) = \frac{G}{\sqrt{\left[1-\left(\frac{\omega}{\omega_j}\right)^2\right]^2 + \left(\frac{\omega}{\omega_j Q}\right)^2}} + Noise, \tag{5.2}$$

In Eq. 5.2, $Z(\omega)$ is the normalized amplitude of the MWNT oscillation, ω is the frequency at which $Z(\omega)$ was measured, G is the overall gain, ω_j is the resonant frequency ($\omega_j = 2\pi f_j$), and *Noise* is the noise offset. To fit the velocity spectrum, the displacement spectrum is differentiated with respect to time, which, in the frequency domain, amounts to multiplying the displacement spectrum by ω. After a least squares fit of the resonance data to Eq. 5.2 was performed, the Q-factor was calculated from the 3dB points determined by the fit.

5.2.1 Vibration spectra of bare MWNTs

The vibration spectra of two bare MWNTs were measured. One such spectrum taken from MWNT $NT1$ is shown in Fig. 5.3(a). We attempted to measure the vibrational spectra of other bare MWNTs, but their small diameter prevented us from accurately focusing them in the 50× bright-field microscope of the LDV. The elastic modulus was calculated using Eq. 5.1. Vibration spectra

Table 5.1. Experimentally measured elastic modulus for the MWNTs studied. The calculations in this table assume $d_i = 0.5d_o$. The estimated estimated errors are ±10 nm for d_o, ±0.2 μm for L, and ±2 kHz for f_j.

Bare MWNT	d_o (nm)	L (μm)	f_1 (kHz)	f_2 (kHz)	E_1 (GPa)	E_2 (GPa)
NT1	230	14.4	285	1930	6.2 ± 0.8	7.3 ± 1.0
NT2	176	12.6	929	6730	66.0 ± 9.8	88.2 ± 13.2

from the MWNTs studied revealed peaks at both the first and second bending mode eigenfrequencies, f_1 and f_2. Table 5.1 summarizes the dimensions, resonant frequency peaks, and E for two bare MWNTs. We note the f_2/f_1 ratio for sample $NT2$ is 7.2, somewhat higher than the theoretical value of 6.3. However, the Euler-Bernoulli beam theory assumes straight, homogenous beams while the MWNTs studied are curved, have carbonaceous deposits on the exterior, and, in some cases, exhibit non-uniform mass density along their length (see Fig. 5.3(c)). Any of these reasons might explain why the f_2/f_1 ratio does not exactly match the expected value of 6.3.

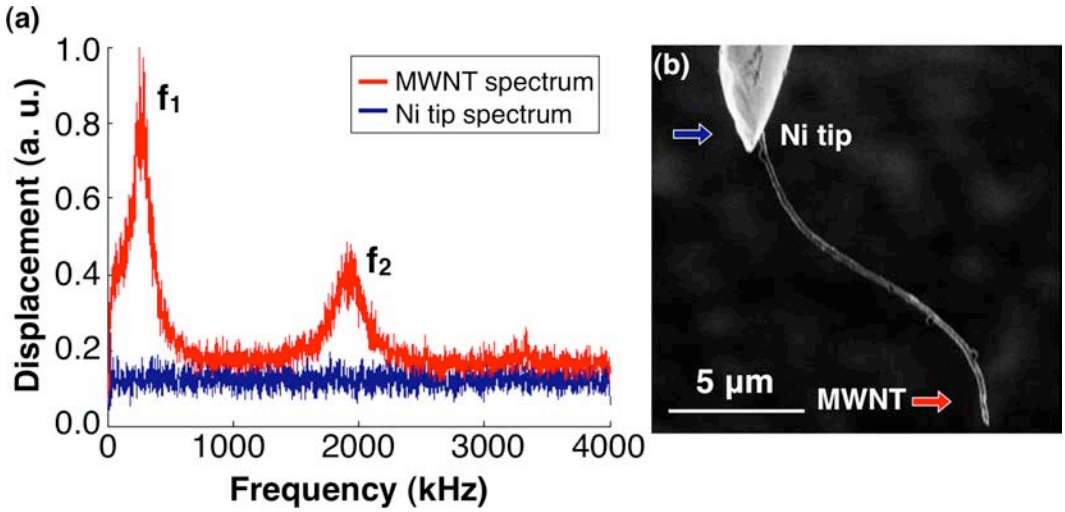

Figure 5.3. In (a), the displacement frequency spectrum from MWNT NT1 shows eigenmode peaks at 285 and 1930 kHz attributed to the 1st and 2nd bending modes of the MWNT. In (b), an SEM micrograph shows the MWNT affixed to the Ni tip. The red and blue arrows represent where the laser vibrometer was focused on the MWNT and Ni tip, respectively. (Reprinted with permission from Ref. [75]. Copyright 2009 by IOP Publishing.)

5.2.2 Extension to smaller diameters: vibration spectra of MWNTs with beads

The lower diameter limit of 70–100 nm for detecting MWNT oscillations restricts this optical technique to relatively large diameter MWNTs. An additional complicating factor is that MWNTs and nanowires with a diameter of only 100 nm are not visible in the 50× bright-field optical microscope used to focus the laser light of the vibrometer. As a first step to measuring the vibration spectra of MWNTs and nanowires with smaller diameters, we developed a technique to add a small glass bead to the end of an individual MWNT. An advantage of adding a glass bead is the additional light that scatters from the bead makes the bead easier to align with the focused laser beam.

Partially gold-coated glass beads (Duke Scientific 9002 borosilicate glass spheres with diameter $2.0 \pm 0.5\,\mu m$) were prepared and transferred to a MWNT using a 0.25 mm diameter Ni wire under the magnification of a 50× dark-field microscope. The Ni wire was first inserted into a vial containing the glass beads. Upon withdrawal, hundreds of glass beads were attached to the Ni wire. One side of each bead was then partially coated with a thin layer of gold after inserting the Ni wire into a thermal evaporator. An STM tip was then used to transfer an individual glass bead from the Ni wire to a MWNT by repeatedly pushing and pulling the MWNT against the bead, as illustrated in Fig. 5.4.

In the case of a large mass added to the end of the MWNT ($m_{bead} \gg m_{MWNT}$), the mass of

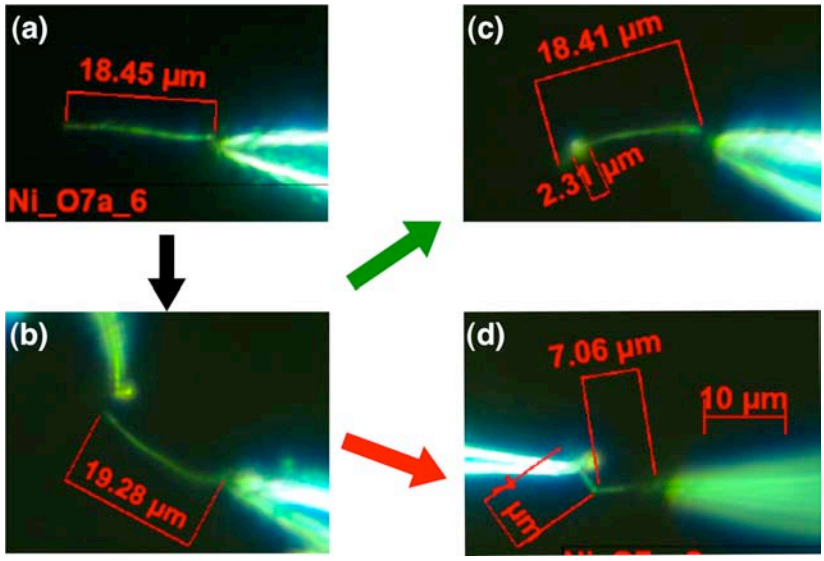

Figure 5.4. In (a), a 50× darkfield image of a MWNT affixed to an Ni STM tip. In (b), a gold-coated glass bead is on the tip of an etched wire. By repeatedly pushing and dragging the MWNT against the bead, the bead can be transfered to the MWNT, as seen in (c). In (d), if the MWNT has a "kink" defect along its length, the MWNT will bend when pushed against the glass bead. Such MWNTs with "kink" defects were excluded from further study.

the MWNT can be neglected and the fundamental bending frequency f_{bend} can be approximated as $f_{bend} = \frac{1}{2\pi}\sqrt{k/m_{bead}}$. For a cantilevered beam $k_c = 3EI/L^3$, so the bending frequency is

$$f_{bend} = \frac{1}{2\pi}\sqrt{\frac{3EI}{L^3 m_{bead}}}. \tag{5.3}$$

Thermal oscillation spectra were recorded and averaged for several MWNTs with attached beads. Again, the background vibrational spectrum from the Ni tips was uniformly featureless. One such spectrum taken from MWNT $NT5$ is shown in Fig 5.5(a). Figure 5.5(b) shows an SEM micrograph of the MWNT with an Au-coated glass bead. Table 5.2 summarizes the dimensions, resonance frequency peaks, and E calculated for three MWNTs with glass beads affixed. The values of E are within the range of modulus values, $\bar{E}$=3-600 GPa, previously reported for CVD-grown MWNTs [26, 34, 36, 25].

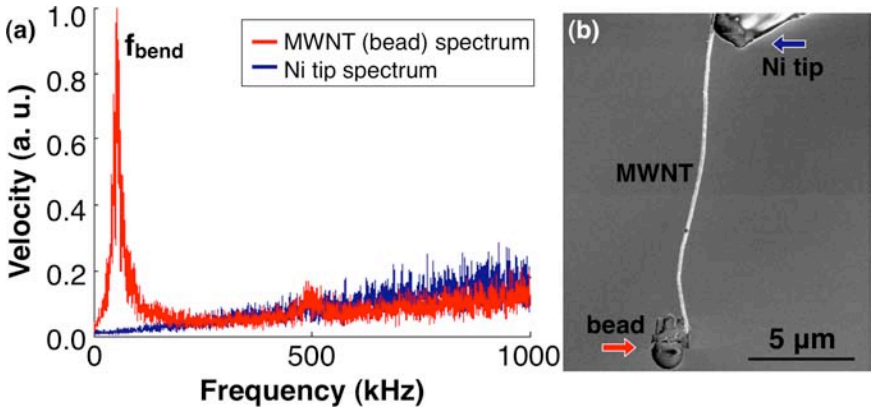

Figure 5.5. In (a), the velocity spectrum of a MWNT showing a vibration peak at 53.3 kHz that is attributed to the bending oscillation of the MWNT. In (b), an SEM micrograph of the MWNT with gold-coated glass bead affixed to the MWNT tip. The red and blue arrows represent where the laser vibrometer was focused on the bead and Ni tip respectively. (Reprinted with permission from Ref. [75]. Copyright 2009 by IOP Publishing.)

Table 5.2. Experimentally measured elastic modulus for MWNTs with beads. The calculations in this table assume $d_i = 0.5d_o$. The estimated estimated errors are ± 10 nm for d_o, $\pm 0.2\,\mu$m for L, and ± 2 kHz for f_j. Bead diameters (not listed, estimated error ± 20 nm) were measured in the FESEM and used to estimate the mass of the bead.

MWNT with bead	d_o (nm)	L (μm)	m_{bead} (pg)	f_{bend} (kHz)	E (GPa)
NT3	160	14.0	12.1	44.9	29.3 ± 8.6
NT4	177	15.1	4.88	68.4	22.9 ± 6.0
NT5	176	14.7	17.1	53.3	60.8 ± 16.6

5.3 Ag_2Ga nanoneedle results

A key advantage of the LDV technique is that it is completely general and can be used to measure the vibration spectra of any nanowire that reflects sufficient light. After hearing our presentation on the above research on MWNTs at the 2008 APS March Meeting, Dr. Mehdi Yazdanpanah asked us to collaborate with him to measure the E and Q of Ag_2Ga nanoneedles.

During the course of this research, the vibrational spectra of eight Ag_2Ga nanoneedles with diameters 65–300 nm and lengths 4–60 μm were measured using laser Doppler vibrometery. The dimensions of these nanowires are tabulated in Table 5.3. As described in section 2.2, the nanoneedles are faceted with a nearly-circular cross-section. Since the number of facets is not known, the nanoneedle cross-section is approximated as circular. These nanoneedles, grown by Dr. Yazdanpanah, were grown on both etched W STM tips and conventional AFM cantilevers, using the methods described in section 2.2.1. No characteristic difference was observed for the nanoneedles grown on STM tips versus AFM cantilevers.

Table 5.3. Dimensions of the eight Ag_2Ga nanoneedles studied as determined from SEM micrographs. In what follows, nanoneedles *NNB*, *NND*, *NNE*, *NNG*, and *NNB*2 are discussed in more detail.

Designation	Length (μm)	Diameter (nm)	Comments
NNA	23 & 30	115 & 194	two conjoined nanoneedles of unequal diameter and length
NNB	60	206	long, straight nanoneedle
NNC	9.6	163	short, stiff nanoneedles
NND	4.3	96	flat frequency response <2 MHz
NNE	6.2	106	flat frequency response <1 MHz
NNF	22	65	very soft cantilever ($k_c \sim 10^{-5}$)
NNG	10	301	high Q_1 = 50 in atmosphere
NNB2	16.6 & 17	140	two conjoined nanoneedles of nearly equal diameter and length

The vibration spectra was primarily measured using the displacement decoder (frequency range 0.05–20 MHz) so that the higher eigenfrequencies could be detected. The vibration spectra of a few long nanoneedles with $f_1 \sim$ 10s kHz were also measured with the velocity decoder (frequency range 0–1.5 MHz).

All the spectra presented in this section were measured in the time domain; an autocorrelation algorithm implemented using Matlab's PWelch function was used to transform the time signal (displacement or velocity) into a power spectra density in the frequency domain. The Matlab code used to analyze the vibration spectra is given in Appendix E.

Since the Ag_2Ga nanoneedles are more reflective than the MWNTs, the scanning feature of

the LDV could be used to measure the vibration spectra along the entire length of the nanoneedle. To measure the operating deflection shape (ODS), the nanoneedles were mounted on top of a piezoelectric plate and excited using the "PsuedoRandom" excitation mode of the LDV. With the phase information obtained from the drive signal, the ODS could be measured.

5.3.1 Eigenfrequencies f_1–f_9 measured from the vibration spectra of a long Ag_2Ga nanoneedle

The vibration spectra of an exceptionally long nanoneedle, *NNB*, ($L = 60\,\mu$m, d_o = 205.5 nm) were measured using both the velocity decoder and the displacement decoder. Both decoders were used since the first eigenfrequency, f_1=0.026 MHz, was below the frequency limit, 50 kHz, of the displacement decoder. From these spectra the f_j and associated quality factors, Q_j, were determined by curve fits of the PSD. The displacement spectra is fit by

$$S_{zz}(f) = \frac{A_j}{Q_j f_j^3} \frac{1}{\left[1-(\frac{f}{f_j})^2\right]^2 + \left(\frac{f}{Q_j f_j}\right)^2} + Noise_j, \tag{5.4}$$

which is the extension of Eq. 4.3 for multimode oscillations. To fit the velocity spectra, Eq. 5.4 is multiplied by $(2\pi f)^2$; that is,

$$S_{zz,\,vel}(f) = \frac{A_j}{Q_j f_j^3} \frac{(2\pi f)^2}{\left[1-(\frac{f}{f_j})^2\right]^2 + \left(\frac{f}{Q_j f_j}\right)^2} + Noise_j. \tag{5.5}$$

Since the velocity PSD $S_{zz,\,vel}(f)$ is only fit to the eigenfrequency peaks, a constant noise offset is assumed. Figure 5.6 shows the velocity (b) and displacement spectra (c) of *NNB* with overlaid curve fits, as well as an SEM micrograph of *NNB* (a).

The eigenfrequency peaks were identified by the comparing the measured ratio f_j/f_k to the theoretical ratio $(\alpha_j/\alpha_k)^2$. From this comparison (see Table 5.4), the spectral peaks were identified as corresponding to the 1st through 4th eigenmodes of vibration for the velocity spectra and the 2nd through 9th eigenmodes for the displacement spectra. This identification of the eigenfrequencies was confirmed by observing the ODS; Fig. 5.6(d) shows the ODS of the eighth eigenmode. The low error (less than 1 percent) of the frequency ratio demonstrates that the motion of this straight, high-aspect ratio nanoneedle is well described by Euler-Bernoulli beam theory.

Figure 5.6

In (a), an SEM micrograph of NNB, which was grown on a Ag-coated W STM tip. (b) The 1st through 4th eigenfrequencies are observed in the velocity PSD. (c) The displacement PSD shows the 2nd through 9th eigenfrequencies. The tick marks above the spectra peaks indicate the theoretical location of each eigenfrequency peak. In (b) and (c), the curve fits to Eqs. 5.4 and 5.5 indicate the frequency range of the integral used to calculate $\langle z_j^2 \rangle$. In (d), the measured operating deflection shape at 3.8 MHz has eight extrema, as is expected for the eighth eigenmode.

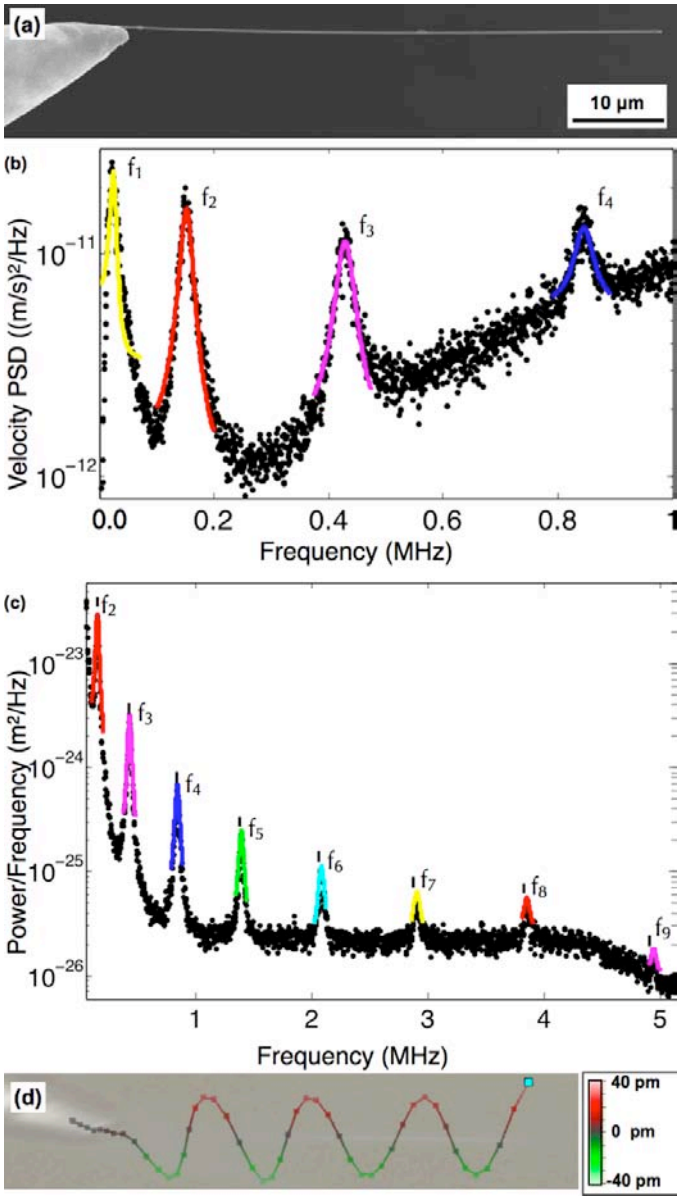
(a)
10 μm
(b)
f1
f2
f3
f4
Velocity PSD ((m/s)²/Hz)
10⁻¹¹
10⁻¹²
0.0
0.2
0.4
0.6
0.8
1
Frequency (MHz)
(c)
f2
f3
f4
f5
f6
f7
f8
f9
Power/Frequency (m²/Hz)
10⁻²³
10⁻²⁴
10⁻²⁵
10⁻²⁶
1
2
3
4
5
Frequency (MHz)
(d)
40 pm
0 pm
-40 pm

Figure 5.6.

Table 5.4. The measured eigenfrequencies, f_j, of *NNB* and mean square displacements, z_j^2, of the 1st–9th eigenmodes, as determined from both the velocity and displacement spectra. The percent error is calculated from the frequency ratios. The scaling factor γ_j is calculated from Eq. 5.10.

	Measured frequencies					Areas of peaks		
j	f_j (MHz)	f_j/f_2	$(\alpha_j/\alpha_2)^2$	% error	$K^j_{eq,\,freq}$ (N/m)	$\langle z_j^2 \rangle$ (nm^2)	$K^j_{eq,\,area}$ (N/m)	γ_j
Values measured from *NNB*'s velocity spectra								
1	0.0256	—	—	—	1.2×10^{-4}	32	1.27×10^{-4}	0.83
2	0.153	1.000	1.000	0	0.0041	0.67	0.0060	0.69
3	0.423	2.809	2.800	0.30	0.033	0.079	0.052	0.63
4	0.846	5.528	5.486	0.76	0.13	0.033	0.12	1.0
Values measured from *NNB*'s displacement spectra								
2	0.152	1.000	1.000	0	0.0042	0.84	0.0048	0.84
3	0.428	2.822	2.800	0.78	0.032	0.10	0.041	0.80
4	0.838	5.528	5.486	0.77	0.12	0.024	0.17	0.74
5	1.388	9.156	9.070	0.94	0.34	0.0098	0.41	0.82
6	2.079	13.71	13.55	1.2	0.76	0.0054	0.75	1.0
7	2.900	19.13	18.93	1.1	1.5	0.0036	1.1	1.3
8	3.846	25.37	25.20	0.69	2.6	0.0032	1.3	2.1
9	4.938	33.57	32.36	0.65	4.3	0.0011	3.8	1.1

The first eigenfrequency, $f_1 = 0.0256$ MHz, is higher by 4.8 percent than the value expected from Euler-Bernoulli beam theory. Assuming that f_2 is as predicted using Euler-Bernoulli beam theory, then

$$f_1 = \frac{f_2}{(\alpha_2/\alpha_1)^2} = \frac{0.153 \text{ MHz}}{6.27} = 0.0244 \text{ MHz}. \tag{5.6}$$

This frequency shift of 1.2 kHz could be caused by a small force on the free end of *NNB*. A small force on the free end of the nanoneedle would (1) raise the eigenfrequencies and (2) have the greatest effect on the least stiff eigenmode, j=1. The incident laser light exerts a small optical force on the nanoneedle, as discussed in Section 5.3.4.

From the measured f_j and the dimensions of *NNB*, E is calculated using Eq. 5.1. From the displacement data for *NNB*, $E = 84.4 \pm 0.6$ GPa, where the error in the measurement is due to the variance in the eight measured f_j. (The larger variance in the f_j determined from the velocity spectra yields $E = 87.2 \pm 3.9$ GPa.) The equation for the static bending stiffness from Section 4.2 ($k_c = 3EI/L^3$) gives $k_c = 1.02 \times 10^{-4}$ N/m for this nanoneedle, where the value of E was determined from the eigenfrequencies of the displacement spectra. The equivalent spring constant ($K^j_{eq,\,freq} = k_c \alpha_j^4/12$) is tabulated for each eigenmode in Table 5.4.

Following the method of Section 3.2.3, the mean square displacement (MSD) is calculated from $z_{meas}(t)$ (displacement spectra only). As mentioned earlier, this method overestimates $\langle z^2 \rangle$

for the first eigenmode because the contributions of the higher modes can not be discarded. After correcting for the offset, the MSD in the time domain is $\langle z_{time}^2 \rangle$ = 44.6 nm^2. Using the value of k_c from above, the potential energy measured in the time domain is 2.27×10^{-21} J. By the equipartition theorem, the thermal energy is equated to the potential energy,

$$\frac{1}{2}k_B T = \frac{1}{2}k_c \langle z_{time}^2 \rangle, \tag{5.7}$$

At T = 293 K, $E_{thermal}$ = 2.0×10^{-21} J. The good agreement between $E_{thermal}$ and $E_{potential}$ suggest that there is no significant heating of the nanoneedle by the laser.

The equivalent spring constant, K_{eq} can also be calculated from the peak areas of each eigenmode. By the equipartition theorem,

$$K_{eq,\,area}^{j} = \frac{k_B T}{\langle z_j^2 \rangle} \tag{5.8}$$

From the measured PSD, $\langle z_j^2 \rangle$ is calculated for each eigenmode. For the displacement spectra, $\langle z_j^2 \rangle$ are calculated by numerically integrating the area under each eigenfrequency peak, as described previously. To calculate $\langle z_j^2 \rangle$ from the velocity PSD, the measured $S_{zz,\,vel}$ is converted to frequency units before integrating over the width of the frequency peak, $2\Delta f$. For the velocity spectra,

$$\langle z_j^2 \rangle = \int_{f_j-\Delta f}^{f_j+\Delta f} df \frac{S_{zz,\,vel}(f)}{(2\pi f)^2} \tag{5.9}$$

The calculated $K_{eq,\,area}^{j}$ and $\langle z_j^2 \rangle$ for each eigenmode are given in Table 5.4.

The spring constant should be the same whether it is derived from the eigenfrequencies and nanoneedle dimensions, as is $K_{eq,\,freq}^{j}$, or the area under the PSD, as is $K_{eq,\,area}^{j}$. For this reason, a scaling factor γ_j is introduced where

$$\gamma_j = \frac{K_{eq,\,freq}^{j}}{K_{eq,\,area}^{j}}. \tag{5.10}$$

Ideally, $\gamma_j = 1$. In practice, $\gamma_j < 1$ indicates that the $\langle z_j^2 \rangle$ inferred from the PSD underestimates the actual MSD. An underestimation of the MSD is expected for objects much smaller than the 0.9 μm spot size of the LDV's laser beam (cf. Fig. 4.2). Only for the highest eigenmodes (j=7-9) is $\gamma_j > 1$. The signal-to-noise ratio decreases for higher eigenmodes; values of $\gamma_j > 1$ likely indicate increased noise contributions to the calculated $\langle z_j^2 \rangle$.

5.3.2 Vibrational spectra of short nanoneedles show flat frequency response below 1 MHz

For sensing applications, a flat frequency response over a large frequency bandwidth is ideal. Short nanoneedles are thus ideal, since $f_j \propto L^{-2}$. To investigate this further, the thermal vibration spectra of two short nanoneedles [NND, ($L = 4.3\,\mu$m, d_o = 96 nm) and NNE, ($L = 6.2\,\mu$m, d_o = 106 nm)]

were measured. Both spectra show a flat frequency response below ∼1 MHz [Fig. 5.7(a,b)]. Nanoneedle *NND* has a pair of first eigenfrequency peaks at 2.17 MHz and 2.44 MHz; the slightly longer *NNE* has a pair of eigenfrequency peaks at 1.18 MHz and 1.51 MHz (see Table 5.5). For both nanowires, k_c ∼0.01 N/m. As described in the following section, these split eigenfrequency peaks are due to an asymmetrical nanoneedle cross-section. A close examination of Fig. 5.7(d) reveals a second nanoneedle, only 1.5 μm long, grown parallel to the 6.2 μm long nanoneedle.

Table 5.5. The measured eigenfrequencies and quality factors of nanoneedles *NND* and *NNE*. Only a single second eigenfrequency above the noise floor was observed for *NNE*.

	$f_{1,a}$	$f_{1,b}$	$f_{2,a}$	$f_{2,b}$	$Q_{1,a}$	$Q_{1,b}$	$Q_{2,a}$	$Q_{2,b}$
NND	2.17	2.44	12.7	14.4	17	28	56	65
NNE	1.18	1.51	8.67		7.4	16	75	

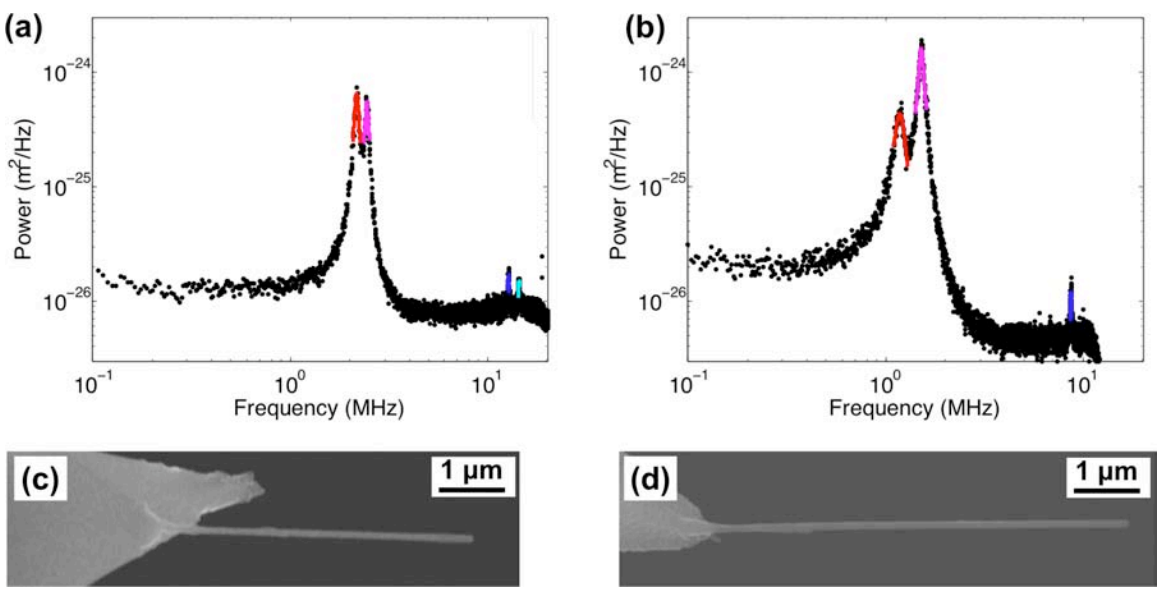

Figure 5.7. In (a) and (b), log-log plots of the power spectra densities of NND and NNE, respectively, show a flat frequency response below ∼1 MHz. In (c) and (d), SEM micrographs of NND and NNE, respectively.

5.3.3 Non-degenerate eigenfrequency peaks caused by asymmetrical nanoneedle cross sections

The vibrational spectra can be used to identify the degree of asymmetry of the nanoneedles. Circularly symmetric nanoneedles, such as *NNB* [Fig. 5.6(c)] have degenerate eigenfrequencies in the perpendicular directions $\hat{x}$ and $\hat{y}$, where $\hat{x}$ and $\hat{y}$ are normal to the long axis of the nanoneedle. A pair of eigenfrequency peaks, such as seen in Fig. 5.7, occurs when the areal moment of inertia, I, is no longer degenerate. In this case, Eq. 3.6 leads to a pair of eigenfrequencies, $f_{j,a}$ and $f_{j,b}$:

$$f_j = \frac{\alpha_j^2}{2\pi L^2}\sqrt{\frac{EI}{\rho_L}} \Rightarrow \begin{array}{l} f_{j,a} = \frac{\alpha_j^2}{2\pi L^2}\sqrt{\frac{EI_x}{\rho_L}} \\ f_{j,b} = \frac{\alpha_j^2}{2\pi L^2}\sqrt{\frac{EI_y}{\rho_L}} \end{array} \tag{5.11}$$

Elliptical nanowires

It is possible that the cross-sectional area of a single nanoneedle is out of round, resembling an ellipse rather than a circle. The areal moment of inertia of an ellipse is $I_o = \frac{\pi}{4}\mathsf{ab}^3$, where a is the semimajor axis and b is the semiminor axis. The two inertias Is are $I_x = \frac{\pi}{4}\mathsf{ab}^3$ and $I_y = \frac{\pi}{4}\mathsf{a}^3\mathsf{b}$. For a nanowire with an elliptical cross-section, one might expect two closely spaced frequency peaks, with the ratio of the frequency peaks given by Eq. 5.13,

$$\frac{f_{j,a}}{f_{j,b}} = \sqrt{\frac{I_y}{I_x}} = \frac{\mathsf{a}}{\mathsf{b}}. \tag{5.12}$$

Consider Table 5.5. The implication is that $\mathsf{a}/\mathsf{b} \simeq 1.12$–$1.28$, indicating that the needles are "out of round" by 10–30 percent.

Conjoined cylindrical nanowires

An extreme example of a non-symmmetric nanoneedle is nanoneedle *NNB*2, which consists of two parallel nanoneedles, 16.6 μm and 17 μm long, each with a diameter of $\sim$140 nm, as shown in Fig. 5.8(b)]. The average length of these nanoneedles is $L_{avg} = 16.8$ μm. These nanoneedles are joined together and oscillate in unison in the perpendicular directions $\hat{x}$ and $\hat{y}$, as shown in Fig. 5.8.

The vibrational spectra of *NNB*2 (as shown in Fig. 5.9) has a pair of first eigenfrequency peaks at $f_{1,a} = 0.22$ MHz and $f_{1,b} = 0.46$ MHz and a pair of second eigenfrequency peaks at $f_{2,a} = 1.42$ MHz and $f_{2,b} = 2.79$ MHz. As before, these eigenfrequencies are identified by their ratios, $f_{2,a}/f_{1,a} = 6.40$ and $f_{2,b}/f_{1,b} = 6.03$, both of which are close to the theoretical value of 6.27. This frequency splitting is attributed to the asymmetric I. Following Eq. 5.11, the measured moment of inertia ratio can be calculated from the ratio of the eigenfrequency pairs,

$$\frac{I_y}{I_x} = \left(\frac{f_{j,a}}{f_{j,b}}\right)^2. \tag{5.13}$$

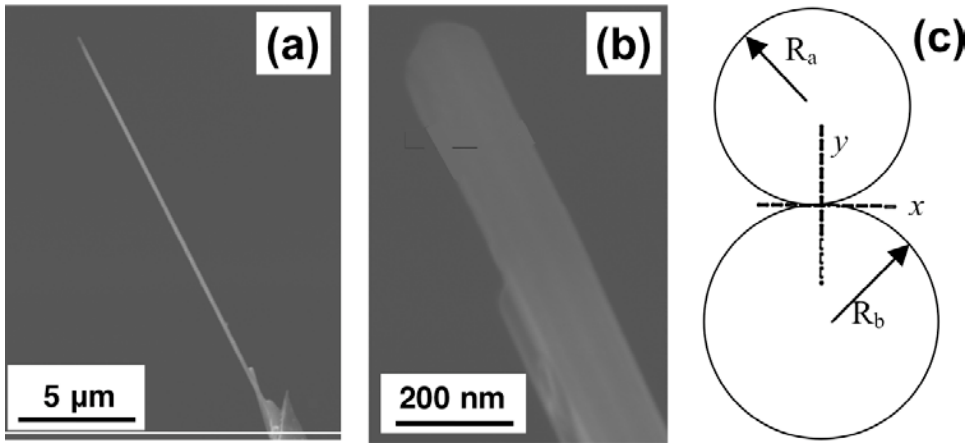

Figure 5.8. In (a) and (b), SEM micrographs of nanoneedle B2 show two parallel nanoneedles, 16.6 μm and 17 μm long. In (c), an illustration of the cross-sectional area.

For $NNB2$, the ratio I_y/I_x is 0.23 for the first eigenmode and 0.26 for the second eigenmode.

For the conjoined nanoneedle pair $NNB2$, I_x and I_y are calculated using the parallel axis theorem. The parallel axis theorem gives the areal moment of inertia through an axis parallel to the object's center of mass:

$$I_{\parallel} = I_{cm} + Ad^2, \tag{5.14}$$

where $I_{cm} \equiv I$, the areal moment of inertia for a cylinder, A is the cross-sectional area of the nanowires, and d is the perpendicular distance from the parallel axis to the object's center of mass. For conjoined nanoneedles, $A = \pi(R_a^2 + R_b^2)$. Following the convention of diagram Fig. 5.8(c), I_x and I_y are given by

$$\begin{aligned} I_x &= \left(\tfrac{\pi}{4}R_a^4 + R_a^2 \cdot \pi R_a^2\right) + \left(\tfrac{\pi}{4}R_b^4 + R_a^2 \cdot \pi R_b^2\right) = \tfrac{5\pi}{4}(R_a^4 + R_b^4) \\ I_y &= \tfrac{\pi}{4}(R_a^4 + R_b^4) \end{aligned} \tag{5.15}$$

where R_a and R_b are the radii of the two nanoneedles. The theoretical ratio of the moment of inertia is $I_y/I_x = 0.2$ for conjoined nanoneedles. The measured I_y/I_x ratios, 0.23 and 0.26, are in good agreement with the theoretical ratio.

Recall that the elastic modulus is

$$E = \frac{\rho A}{I}\left(\frac{f_j 2\pi L^2}{\alpha_j^2}\right)^2. \tag{5.16}$$

For the case of two parallel nanoneedles of equal radius, R, and length, L_{avg}, substitutions of

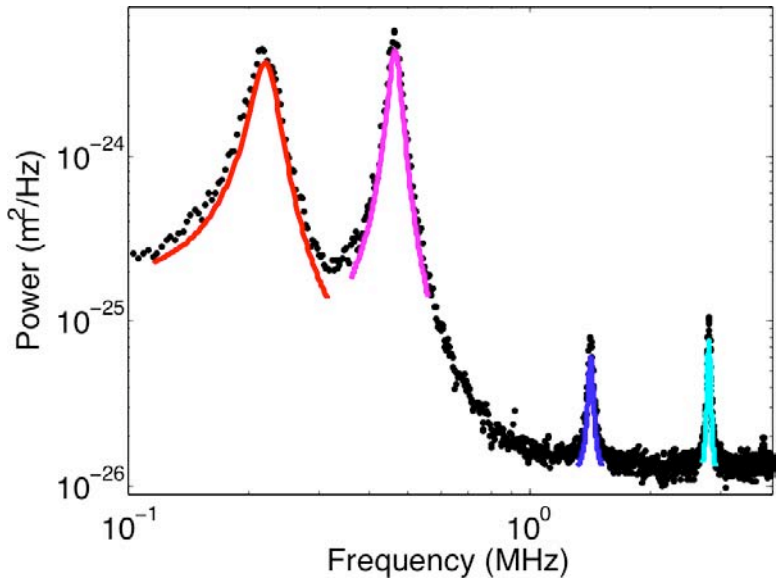

Figure 5.9. The vibrational spectra of nanoneedle pair *NNB*2 shows two first eigenfrequency peaks at $f_{1,a} = 0.22$ MHz and $f_{1,b} = 0.46$ MHz and two second eigenfrequency peaks at $f_{2,a} = 1.42$ MHz and $f_{2,b} = 2.79$ MHz.

I_x, I_y, and $A = 2(\pi R^2)$ yields

$$E_x = 4\rho \left(\frac{f_{j,b} 2\pi L_{avg}^2}{R\alpha_j^2} \right)^2$$
$$E_y = \frac{4\rho}{5} \left(\frac{f_{j,a} 2\pi L_{avg}^2}{R\alpha_j^2} \right)^2, \tag{5.17}$$

where the higher $f_{j,b}$ eigenfrequencies are associated with the larger I_x.

The above analysis was used to calculate E for nanoneedle *NNB*2. Both of the component nanoneedles were assumed to have the same diameter, 140 nm, and length L_{avg} = 16.8 μm. Table 5.6 gives the possible values of E, which are calculated from Eq. 5.17 and the eigenfrequencies of Fig. 5.9. The mean value of E is $E = 85 \pm 10$ GPa for this coupled nanoneedle pair.

Table 5.6. Calculated elastic moduli for *NNB*2.

	$f_{1,a}$ (kHz)	$f_{1,b}$ (kHz)	$f_{2,a}$ (kHz)	$f_{2,b}$ (kHz)
E_x (GPa)	—	—	80	74
E_y (GPa)	91	95	—	—

The alternative possibility that the two nanoneedles oscillated independently was also considered. However, that condition led to the unlikely value of $E \sim 370$ GPa and was thus discarded.

5.3.4 Optical forcing and trapping of a Ag_2Ga nanoneedle

Brief literature review of optical trapping

Optical trapping of a spherical particle by a single laser beam was first demonstrated in 1986. Ashkin *et al.* trapped spherical dielectric silica and glass particles of diameter ~25 nm to 10 μm in water using a 514.5 nm Gaussian laser beam [76]. Cylindrical particles can also be manipulated and moved in an optical trap. Depending on the aspect ratio of the cylinder, the cylinders may align either parallel to or perpendicular to the direction of propagation of the laser beam. Gauthier *et al.* trapped glass cylinders, $d_o = 5\,\mu$m, with a 515-nm laser. They found that long cylinders ($L = 26\,\mu$m) aligned with propagation axis of a laser beam while short cylinders ($L = 5\,\mu$m) aligned transverse to the propagation axis [77].

The ability of a particle, such as a nanowire, to be caught in an optical trap depends on the refractive index, $N = n + i\kappa$, and, to a lesser degree, the cross-section of the nanowire. Pauzauskie *et al.* stably trapped semiconducting wires having circular and polyhedral cross-sections (Si, GaN, SnO_2) with n varying between 1.9 and 3.6 and d_o between 10 nm and 600 nm. The semiconducting SnO_2 nanowires with asymmetric (ribbon) cross-sections oscillated between two and six states. However Ag nanowires (d_o = 50 nm) could not be trapped; instead the Ag nanowires were repelled from the laser focal spot [78]. [Please note, the value of n = 6.1 at λ = 1064 nm (1.16 eV) quoted by Ref. [78] is an order of magnitude greater than reported by other sources. For example, Ref. [73] gives $N = 0.226 + i * 6.99$ for Ag at 1.2 eV. Despite this numerical discrepancy, I believe the results Pauzauskie *et al.* reported are valid.]

Optical forces relevant to trapping

The optical force on a particle in a laser beam can be decomposed into three components, $\mathbf{F}_{sca}$, $\mathbf{F}_{abs}$, and $\mathbf{F}_{grad}$. The scattering force, $\mathbf{F}_{sca}$, and the absorption force, $\mathbf{F}_{abs}$, both act parallel to the direction of propagation of the beam [79]. The gradient force, $\mathbf{F}_{grad}$, has two components, one parallel ($\|$) and one perpendicular ($\perp$) to the beam. The condition for stably optically trapping a particle is that the parallel forces must be equally balanced, so that $|\mathbf{F}_{grad}|_{\|} = -\left(|\mathbf{F}_{sca}| + |\mathbf{F}_{abs}|\right)_{\|}$ [80]. These forces in turn depend on the polarizability, α, of the particle and the scattering and absorption cross sections, C_{sca} and C_{abs}. The optical forces are

$$\begin{aligned} \mathbf{F}_{sca} &= \tfrac{n_{med}}{c}\langle\vec{S}\rangle C_{sca} \\ \mathbf{F}_{abs} &= \tfrac{n_{med}}{c}\langle\vec{S}\rangle C_{abs} \\ \mathbf{F}_{grad} &= \tfrac{1}{2}|\alpha|\nabla\langle\vec{E}^2\rangle \end{aligned} \tag{5.18}$$

where n_{med} is the index of refraction of the medium, c is the speed of light, $\mathbf{E}$ is the electric field, and $\mathbf{S}$ is the Poynting vector [81, 82].

The polarizability, α is a function of the dielectric constant of the particle, $\tilde{\varepsilon}$, and the surround-

ing medium, $\tilde{\varepsilon}_{med}$. The polarizability of a particle of effective volume V_{eff} is [79]

$$\alpha = 3V_{eff}\frac{\tilde{\varepsilon}-\tilde{\varepsilon}_{med}}{\tilde{\varepsilon}+2\tilde{\varepsilon}_{med}}, \text{ where } \tilde{\varepsilon} = \varepsilon_1(\lambda)+i\varepsilon_2(\lambda). \tag{5.19}$$

The dielectric constant, $\tilde{\varepsilon}$, is directly related to the index of refraction by [83]

$$\varepsilon_1 = n^2-\kappa^2 \text{ and } \varepsilon_2 = 2n\kappa. \tag{5.20}$$

For the relevant case of silver particles in air illuminated by 633 nm laser, $\tilde{\varepsilon}_{Ag} = -16.0+i1.12$ [73] and $\tilde{\varepsilon}_{med} = 1$. Thus $\alpha/(3V_{eff}) = 1.21+0.017\,i$. The effective volume of a cylinder of length L and radius a is [79]

$$V_{eff} = 2\pi L\int_0^a dr\,r\,e^{(r-a)\delta} = 2\pi L\delta^2[e^{-a/\delta}+a/\delta-1], \tag{5.21}$$

where the skin depth is $\delta = \lambda/(2\pi\kappa)$.

The scattering efficiencies, $\mathscr{Q}$, defined in section 4.4, are proportional to the cross sections, C;

$$\mathscr{Q}_{sca} = \frac{C_{sca}}{G}, \quad \mathscr{Q}_{abs} = \frac{C_{abs}}{G}, \tag{5.22}$$

where G "is the particle cross-sectional area projected onto a plane perpendicular to the incident beam" [70]. For a spherical particle of radius a, $G = \pi a^2$. Since the nanowires are modeled as infinite cylinders illuminated by a laser beam of radius r_o, $G = 2d_or_o$ for cylinders (assuming $d_o < r_o$). For an Ag nanowire, $C_{sca} = 2d_or_o\mathscr{Q}_{sca}$; the values of $\mathscr{Q}_{sca}$ for circularly-polarized 633-nm light are plotted in Fig. 4.5(a).

Optical forces exerted on cylindrical Ag nanowires

The optical forces (Eq. 5.18) can be estimated for the case of a cylindrical nanowire placed at the beam waist of a focussed laser beam. At the beam waist, the power P_o of a Gaussian beam is proportional to the intensity, I_o, at the center of the beam, $P_o = (1/2)\pi I_o r_o^2$. The radial intensity, $I(r)$ of such a Gaussian beam is

$$I(r) = I_o\exp[-r^2/(2r_o^2)], \tag{5.23}$$

where r is the radial distance perpendicular to the propagation direction of the beam. The optical forces will then be [79]

$$\begin{aligned} |\mathbf{F}_{sca}(r)| &= \frac{\tilde{\varepsilon}_{med}C_{sca}}{c}I(r) \\ |\mathbf{F}_{abs}(r)| &= \frac{\tilde{\varepsilon}_{med}C_{abs}}{c}I(r) \\ |\mathbf{F}_{grad}(r)| &= \frac{e^{1/2}|\alpha|}{\tilde{\varepsilon}_{med}cr_o}I(r), \end{aligned} \tag{5.24}$$

where $e = 2.718$. The maximum forces $|\mathbf{F}_{sca}|$ and $|\mathbf{F}_{grad}|$ are plotted in Fig. 5.10 as a function of the nanowire diameter for P_o = 1 mW and $r_o = 0.5\,\mu$m. Since $\mathbf{F}_{sca} > \mathbf{F}_{grad}$ for Ag nanowires of $d_o < 300$ nm, we conclude that Ag nanowires can not be stably optically trapped.

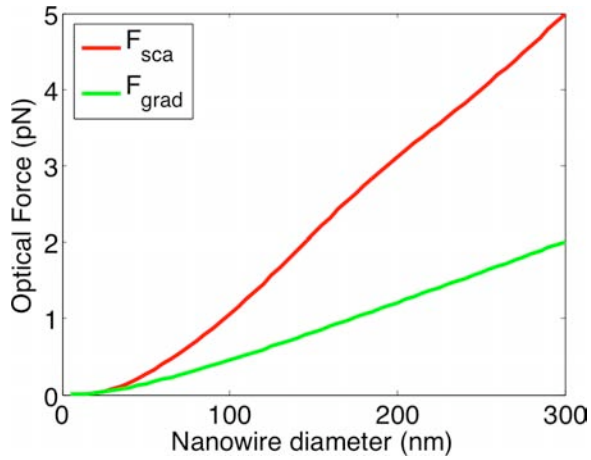

Figure 5.10. The optical forcing on a Ag nanowire from a 633 nm, 1 mW Gaussian laser beam as a function of nanowire diameter.

Experimental observations of optically forced nanoneedles

Optical forcing of nanoneedles was observed for both small diameter (NNF, d_o = 65 nm) nanoneedles in air and large diameter (NNB, d_o = 205.5 nm) nanoneedles in low vacuum (600 mTorr). Both quasi-static bending and oscillatory forcing were observed.

For the case of quasi-static bending, as the laser beam was scanned along the length of the nanoneedle, from the fixed end to the free end, the nanoneedle would bend away from the laser spot. The distance the nanoneedle would bend was often sufficient to bend it out of the spot depth of the interferometer, thus making measurements of the vibration spectra difficult. An example of quasi-static bending caused by optical forcing is shown in Fig. 5.11, an optical microscope image of nanoneedle NNF. Based on the dimensions of NNF and assuming E = 85 GPa, k_c for this nanoneedle is estimated to be 2×10^{-5} N/m. The force required to bend the NNF a distance $\Delta = 2\,\mu$m from the equilibrium position, $F_{spring} = k_c\Delta$, is 0.2 pN. From Eq. 5.24, for a 65-nm diameter Ag nanowire, the radial force F_{grad}, is 0.2 pN and the axial force, F_{sca} is 0.5 pN. These optical forces are approximately equal to the measured F_{spring}.

Optical forcing in atmospheric pressure was only observed for nanoneedle NNF, which had a spring constant an order of magnitude smaller than any other nanoneedles studied. As the pressure is decreased, the damping due to the air molecules no longer is sufficient to damp out the oscillations due to optical forcing. At lower pressures ($P < 1$ Torr), other nanoneedles were also optically forced in a similar manner as NNF.

Less commonly observed was an oscillatory motion that could be excited by positioning the laser beam on a "lucky" resonant position on the nanoneedle. In low vacuum, 650 mTorr, a 200 nm diameter nanoneedle, NNB, was optically forced into resonance. The envelope of the resonance could easily be seen in the 50× optical microscope. Reifenberger also witnessed this oscillatory

Figure 5.11. A 50× optical microscope image of nanoneedle *NNF* (d_o=65 nm, L=21.5 μm), bent $\Delta = 2\,\mu$m away from the equilibrium position due to the optical forcing. The dotted blue line indicates the original, unbent position of the nanoneedle.

forcing effect while I was taking data. By tuning the the focus and location of the LDV laser spot, we were able to quasi-statically bend *NNB*. If the laser spot was focused in a "lucky" position near, but not at, the free end of *NNB*, *NNB* could be driven into optical resonance. We speculate that *NNB* was at a slight angle and the "lucky" position was where the focus of the optical beam was coincident with *NNB*.

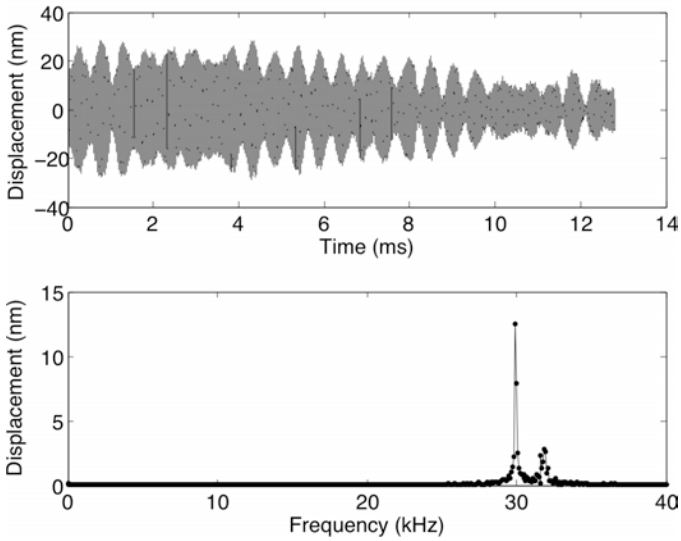

Figure 5.12. (a) The time series measurement of the fundamental (j=1) oscillations of NNB shows sinusoidal oscillations with an amplitude of ∼25 nm and a beat frequency of 2.0 kHz. In (b), the Fourier transform of the time series signal has two low-frequency peaks at 29.9 kHz and 31.9 kHz.

The time series measurements of the oscillations of *NNB* show a resonance with a beat frequency of 2.0 kHz resulting from oscillations at 29.9 kHz and 31.9 kHz (Fig. 5.12). These resonant frequencies are slightly higher than the $f_1 = 0.026$ MHz first eigenfrequency measured in atmosphere. The optical force on the end of *NNB* likely changes the boundary conditions of the Euler-Bernoulli beam equation. A clamped-clamped beam has higher eigenfrequencies than a cantilevered beam. So it is reasonable that the optical forcing tends to increase the resonant frequency of *NNB*.

5.3.5 Nanoneedle vibration spectra measured in low vacuum

Due to optical forcing, nanoneedle spectra measured under vacuum conditions can be more difficult to interpret than spectra measured under atmospheric conditions. The vibration spectra of nanoneedle *NNB*, measured at 650 mTorr, is shown in Fig. 5.13. So that the high Q eigenfrequency peaks could be resolved, the displacement spectrum was measured with a high frequency resolution. 131,072 data points were recorded in 12.8 ms, resulting in a frequency resolution of 78 Hz. Following the method of section 5.3.1, curve fits to Eq. 5.4 were used to determine f_j^{vac} and Q_j^{vac}.

Table 5.7. A comparison of the eigenfrequencies and quality factors of *NNB* at 760 Torr (f_j^{atm}) and 650 mTorr (f_j^{vac}). Split eigenfrequency pairs are observed for f_2^{vac} and f_3^{vac}. An undetermined eigenfrequency peak is observed at 0.53 MHz. No peak attributed to the fifth eigenmode was observed. The percent error is calculated from the difference of f_j^{vac}/f_2^{vac} and $(\alpha_j/\alpha_2)^2$.

j	f_j^{atm} (MHz)	f_j^{vac} (MHz)	$(\alpha_j/\alpha_2)^2$	f_j^{vac}/f_2^{vac}	% error	Q^{atm}	Q^{vac}
1	0.0256					2.2	
2	0.152	0.14	1.000	1.00	0	5.0	200
		0.1542	1.000	1.10	10		420
3	0.428	0.3147	2.800	2.25	20	13	270
		0.3902	2.800	2.79	0.46		260
?		0.5326	?	3.80	?		310
4	0.838	0.7667	5.486	5.48	0.18	21	250
5	1.388		9.070			34	
6	2.079	1.810	13.559	12.9	4.6	67	180
7	2.900	2.328	18.925	16.6	12	100	370

The eigenfrequencies in vacuum, f_j^{vac} (tabulated in Table 5.7) are slightly lower than the atmospheric f_j^{atm} measured for this nanowire. The quality factor of these oscillations, $Q = \sim$200–400 at 650 mTorr, is one to two orders of magnitude greater than in atmosphere. Furthermore, split eigenfrequency peaks are now observed for f_2^{vac} and f_3^{vac}. At atmospheric pressures, split eigenfrequency peaks were not observed in the *NNB* spectra. The split f_2^{vac} and f_3^{vac} eigenfrequency peaks indicate a slight degree of asymmetry for *NNB*. The high Q_j in vacuum allows the split eigenfrequency peaks to be resolved. To understand the degree of asymmetry for *NNB*, *NNB* is modeled as an elliptical beam. Following Eq. 5.12, the ratio $f_{2,a}^{vac}/f_{2,b}^{vac}$ = 0.14 MHz/0.15 MHz =0.9. Thus the ratio of the semimajor and semiminor axes of the beam is 0.9.

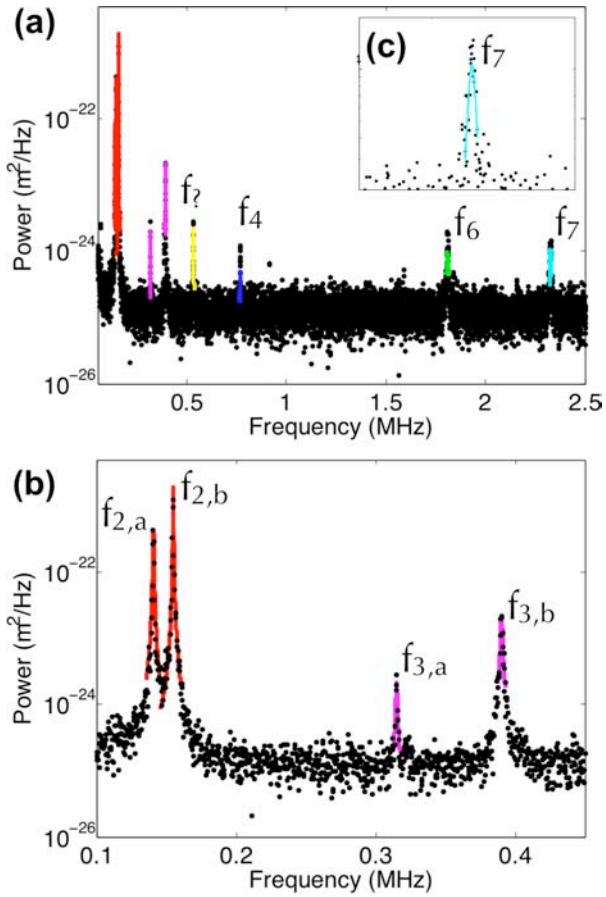

Figure 5.13. (a) The thermal spectra of nanoneedle *NNB*, measured at 650 mTorr, shows f_2–f_4, f_6, and f_7. In (b) the split eigenfrequency peaks f_2^{vac} and f_3^{vac} are visible in this smaller frequency range. Inset (c) highlights the high quality factor of these vibrations, Q_7^{vac} = 370. The PSD was calculated using eight Hamming windows with a 50 percent window overlap.

5.4 Measured quality factors of nanowire oscillations

The quality factor of a specific eigenmode quantifies how much energy is dissipated during one oscillation cycle. High Q (small energy dissipation) is desirable for many applications. Reliable estimates for Q are often difficult to obtain since the measured shape of the resonance as a function of frequency is required for accurate Q determination.

We first report the Q-factors for the MWNTs previously discussed in Section 5.2. The measured Q-factors for our MWNT spectra are reported in Table 5.8. A notable feature of these Q values is they are considerably smaller when compared to micron-sized resonators. For example, Si microcantilevers commonly used in AFM applications typically have Q values of 100-500 when

measured in air. Referring to Table 5.8, we find that for the bare MWNTs, the Q of the second eigenmode is higher than the first. This result is due to the increased stiffness of the second eigenmode, since the Q-factor is proportional to the square root of the modal stiffness [56]. Thus the increased Q is a direct consequence of the increased modal stiffness of the higher eigenmodes.

Table 5.8. Quality factors for the MWNTs studied were determined by fitting Eq. 5.2 to the oscillation resonance spectrum.

Bare MWNT	f_1 (kHz)	Q_1	f_2 (kHz)	Q_2
NT1	285	2.8	1930	9.9
NT2	929	3.3	6730	18
MWNT with bead	f_{bend} (kHz)		Q	
NT3	44.9		5.9	
NT4	68.4		5.0	
NT5	53.8		6.2	

From Table 5.8, we also observe that Q increases with the added mass of the beads. This increase in Q with added mass was recently reported for silicon cantilevers [84] and occurs because Q is also proportional to the square root of the modal mass. When a bead is added, the modal stiffness of the MWNT is unchanged, but the MWNT's modal mass increases which leads to an increase in Q.

The Q-factors for the Ag_2Ga nanoneedles were also measured, as reported in Tables 5.5 and 5.7. At atmospheric pressure, the Q_j of the MWNTs were a factor of five higher than the Q_j of the MWNTs. At low vacuum, Q_j of the Ag_2Ga nanoneedles was 200–400. The Q_j of *NNB*, measured at atmospheric pressure for the 2nd to 9th eigenmodes, are plotted in Fig. 5.14. In atmosphere, the measured Q-factors increased linearly from Q_2=5.0 to Q_9=103.

5.5 Theoretical basis for understanding Q-factors

To quantitatively understand the measured Q values, we note that the measured Q-factor is given by an effective Q (Q_{eff}), where

$$\frac{1}{Q_{eff}} = \frac{1}{Q_{gas}} + \frac{1}{Q_{clamp}} + \frac{1}{Q_{intrinsic}} + \cdots . \tag{5.25}$$

In Eq. 5.25, Q_{gas} accounts for the damping of the oscillating nanowire due to air, Q_{clamp} is the damping due to energy lost at the interface of the nanowire and its support (STM or AFM tip), and $Q_{intrinsic}$ represents the energy lost due to intrinsic defects in the MWNT itself.

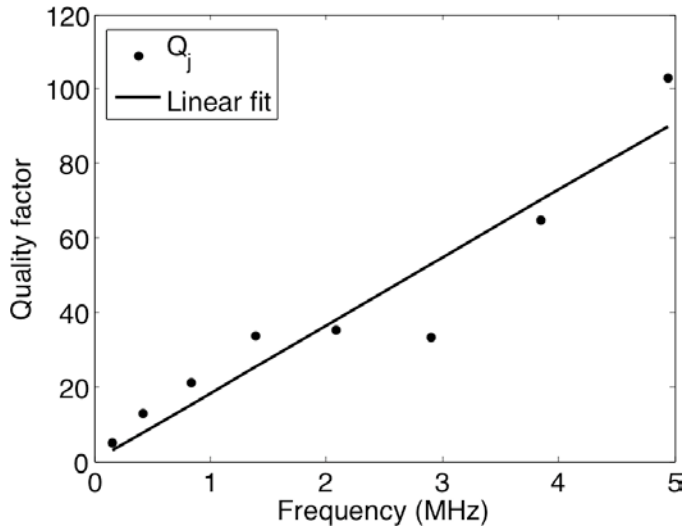

Figure 5.14. The measured Q_j of *NNB* increased linearly with frequency.

The displacement of the MWNT at the Ni tip is several orders of magnitude smaller than the oscillation amplitude of the free end of the MWNT; thus we can treat the clamp as a rigid support, and therefore, $1/Q_{clamp}$ is negligible. From other experiments on MWNTs conducted in UHV, we estimate $Q_{intrinsic} \sim O(10^2)$ [3, 4]. We conclude that when a MWNT is vibrating in air, the majority of the energy is dissipated through gas damping. Using the same arguments, we expect gas damping will also dominate energy loss for Ag_2Ga nanoneedles when measured in air at ambient pressures.

To further check that gas damping is responsible for the small Q values of nanowires oscillating in air, we calculate the Knudsen number, $Kn = l_{mfp}/d_o$, where l_{mfp}, the mean free path of air molecules, is 65 nm for air at STP. Thus the nanowires we have studied have $Kn \approx 0.4$ indicating they are in a cross-over regime ($0.1 < Kn < 10$) [58] for which only approximate gas damping models are available (see section 3.4.1). However at slightly greater Kn numbers ($Kn > 10$) the damping is in the free molecular regime and published theories can be used to estimate Q_{gas}.

In the free molecular regime, the primary source of damping is momentum transfer due to collisions with the surrounding gas molecules. Assuming a flexible beam and following Christian's model [85] for momentum transfer mediated gas damping in the free molecular regime, we find that an expression for gas damping of the jth eigenmode of the MWNT is given by

$$(Q_{gas})_j = \frac{\omega_j \rho A}{4bP}\sqrt{\frac{\pi R_o T}{2M_m}}, \tag{5.26}$$

where P, R_o, and M_m, are the pressure, universal gas constant, and molar mass, respectively. In the case of a cylindrical beam, the effective area for damping per unit length, b, is $\pi d_o/4$ [86]. From Eq. 5.26, we calculate Q_{gas} at atmospheric pressure for (bare) MWNTs and Ag_2Ga nanoneedles

of representative diameters. In Fig 5.15, the measured quality factors corresponding to the first eigenmodes of vibration are superimposed on the calculated Q_{gas}.

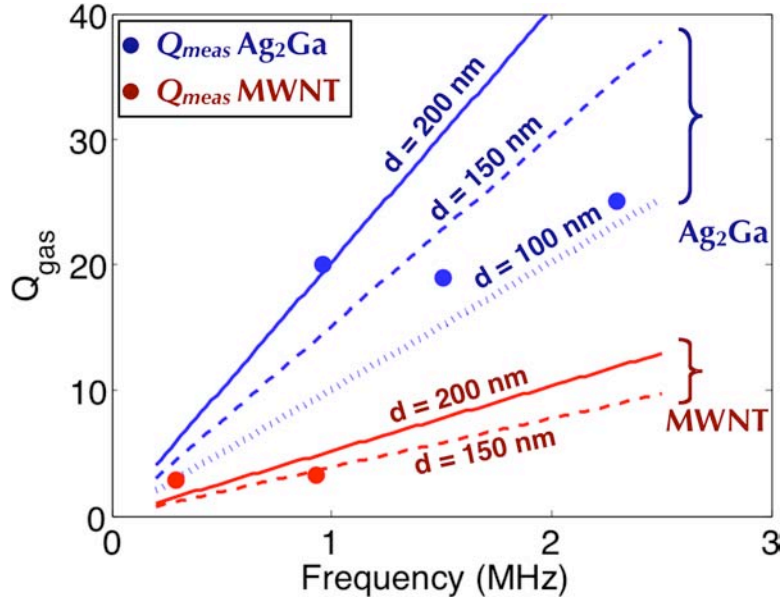

Figure 5.15. The calculated Q_{gas} for nanowires oscillating at atmospheric pressure, using the calculations of the free molecular flow regime. Q_{gas} is calculated for Ag_2Ga nanoneedles (red) and MWNTs (blue) of representative diameters. Measured Q_{meas} corresponding to the first eigenmode of vibration are superimposed on the calculated Q_{gas}

These calculations of the gas damping confirm that the small Q of nanowires oscillating under ambient conditions arises naturally from gas damping. Since the density of Ag_2Ga nanoneedles is approximately three times that of MWNTs ($\rho_{Ag_2Ga} = 8960$ kg/m^3 versus $\rho_{MWNT} = 2300$ kg/m^3), the nanoneedles have a greater Q at atmospheric pressures.

5.6 Proposed application: nanowires as mass sensors

Microscale and nanoscale cantilevers are being investigated as chemical sensors. In the case that an analyte with mass δm binds to a cantilever of mass m, the resonance frequency ω_0 of the cantilever will be downshifted by an amount $\delta\omega$ where

$$\delta\omega = \frac{\omega_0}{2m}\delta m, \tag{5.27}$$

assuming the presence of the analyte does not change the stiffness of the cantilever [87]. Since m is small for MWNTs, the mass of a virus (10^{-15} g) will cause a frequency shift on the order of 10s of

kHz. However, the low quality factor of MWNTs in air limits the minimum detectable frequency shift. For this reason, it is interesting to compare the minimum detectable mass for cantilevered MWNTs and Ag_2Ga nanoneedles. Since Si microcantilevers are currently used as mass sensors, the minimum detectable mass for a standard microcantilever is also calculated.

Thermomechanical noise due to cantilever oscillations limits the minimum detectable mass. The mean-square frequency modulation, $\langle(\delta\omega)^2\rangle$, is given by

$$\langle(\delta\omega)^2\rangle = \frac{\omega_o}{Q}\frac{k_B T}{k_c\langle z_{osc}^2\rangle}B, \tag{5.28}$$

where B is the detection bandwidth and $\langle z_{osc}^2\rangle$ is the mean square amplitude of the self-oscillating cantilever [88]. For multimode oscillations, $k_c = 12K_{eq}^j/\alpha_j^4$; the mean-square frequency modulations are then

$$\langle(\delta\omega_j)^2\rangle = \frac{\alpha_j^4}{12}\frac{\omega_j k_B T B}{Q_j K_{eq}^j\langle z_{j,\,osc}^2\rangle}, \tag{5.29}$$

To calculate $\langle(\delta\omega_j)^2\rangle$, assume that $\langle z_{j,\,osc}^2\rangle$ is proportional to the thermal displacement, $\langle z_{j,\,thermal}^2\rangle$,

$$\langle z_{j,\,osc}^2\rangle = A_j\langle z_{j,\,thermal}^2\rangle = A_j\frac{k_B T}{K_{eq}^j}, \tag{5.30}$$

where $A_j = 1$ for thermally-excited oscillations and $A_j > 1$ for driven oscillations. The mean-square frequency modulation is thus

$$\langle(\delta\omega_j)^2\rangle = \frac{\alpha_j^4}{12}\frac{\omega_j B}{Q_j A_j}. \tag{5.31}$$

The thermomechanical-noise limited minimum detectable mass, $\delta m_{j,\,min}$, is

$$\delta m_{j,\,min} = \frac{2m\delta\omega_j}{\omega_j} = \frac{2m}{\omega_j}\sqrt{\frac{\alpha_j^4}{12}\frac{\omega_j B}{Q_j A_j}}. \tag{5.32}$$

The minimum bandwidth possible while still avoiding aliasing is $B = 2\omega_j$. Thus the minimum detectable mass is proportional to the mass of the cantilever,

$$\delta m_{j,\,min} = \frac{2\alpha_j^2}{\sqrt{6}}\frac{m}{\sqrt{Q_j A_j}}. \tag{5.33}$$

Recall Eq. 3.37 from section 3.4, $Q_j = m\omega_j/(c_f + c_s)$. The minimum detectable mass is proportional to the damping, c, and inversely proportional to the resonant frequency,

$$\delta m_{j,\,min} = 2\frac{\alpha_j^2}{\sqrt{6}}\sqrt{\frac{m(c_f + c_s)}{A_j\omega_j}} \tag{5.34}$$

Recalling Eq. 3.32, the fluid damping, c_f, is proportional to the cantilever dimensions, L and w_{rep}, and the pressure, P. The representative width, w_{rep}, is the width of a rectangular cantilever or the diameter of a cylindrical nanowire. In all fluid damping regimes, $c_f \propto Lw_{rep}P$. At atmospheric pressure, $c_f \gg c_s$, so the minimum detectable mass is proportional to

$$\delta m_{j,\,min} \propto \alpha_j^2 \sqrt{\frac{mLw_{rep}}{A_j\omega_j}P}. \tag{5.35}$$

Thus short, low mass nanowires with high resonant frequencies are ideal for mass sensors. Furthermore, consideration of ω_j suggests that a larger elastic modulus is also desirable.

The mass resolution, $\delta m_{j,\,min}/SA$, is frequently used to characterize and compare mass sensors. The surface area, SA, of the mass sensors is assumed to be functionalized to provide binding sites for the analyte mass. To enable comparison with existing sensors, the mass resolution is calculated for four representative, thermally-excited cantilevers: an Si microcantilever, two MWNTs, and *NND*. The dimensions, mass, first and second eigenfrequency, and associated quality factors for these four cantilevers are tabulated in Table 5.9. These calculated f_j and Q_j agree with experimentally measured values for cantilevers of similar dimensions (cf. Table 5.5 for the eigenfrequencies of *NND*).

Table 5.9. Dimensions and calculated f_j and Q_j of four representative cantilevers. The silicon microcantilever has a width of 35 μm and a thickness of 2 μm. The MWNT dimensions are representative of typical values. *NND* is a Ag_2Ga nanoneedle whose vibrational spectra was measured (see Section 5.3.2).

Cantilever	d_o (nm)	L (μm)	SA (cm^2)	m (pg)	f_1 (MHz)	f_2 (MHz)	Q_1	Q_2
Si μcantilever	—	110	8.1×10^{-5}	2.5×10^{5}	0.21	1.3	270	670
long MWNT	150	20	9.4×10^{-8}	0.81	0.19	1.2	2.2	11
short MWNT	75	5.0	1.2×10^{-8}	0.051	1.5	9.5	4.4	23
NND	96	4.3	1.3×10^{-8}	0.28	2.2	14	37	200

The minimum detectable masses for the first and second eigenmodes were calculated using Eq. 5.34 and $Q = Q_1$ as given in Eq. 3.37; these $\delta m_{1,\,min}$ are tabulated in Table 5.10. As expected, the mass sensitivity increases with decreasing cantilever mass. Despite the much lower Q_1 for the MWNTs, the minimum $\delta m_{1,\,min}$ detectable is a factor of 10^6 smaller for the short MWNT than for a standard Si microcantilever. The associated δf_1 frequency shifts, 0.1–1.0 MHz, due to the presence of the analyte are readily detectable using the LDV (δf_1 are calculated from Eq. 5.27).

Next, the mass resolution is calculated for thermally-excited (A_1=1) cantilevers at atmospheric pressure (Table 5.10). The calculated $\delta m_{1,\,min}/SA$ values represent a worst case scenario for mass sensing. Driving the cantilever would enhance the mass resolution; an order of magnitude increase in A_1 would yield a factor of three decrease in $\delta m_{1,\,min}$. Decreasing the pressure and detecting the frequency shift at higher eigenmodes would also enhance the mass resolution.

Table 5.10. At atmospheric pressure (760 Torr), the calculated minimum detectable mass, mass resolution, and expected frequency shift for four representative thermally-excited cantilevers.

	First eigenmode		
Cantilever	$\delta m_{1,\,min}$ (pg)	$\delta m_{1,\,min}/SA$ (pg/cm^2)	δf_1 (MHz)
Si μcantilever	43 000	5.3×10^8	0.019
long MWNT	1.6	1.7×10^7	0.18
short MWNT	0.070	5.9×10^6	1.03
NND	0.13	1.0×10^7	0.53

We think that the derivation presented in Eqs. 5.28–5.34 is an overly conservative estimate for heavily damped oscillations. A quick, back-of-the-envelope assumption of $\delta f_{j,est} = f_j/Q_j$ yields smaller minimum detectable masses of $\delta m_{j,\,est} = 2m/Q_j$. For *NND*, this estimate yields $\delta m_{1,\,est}$ = 0.015 pg, which represents a factor of 10 improvement in mass sensitivity.

The mass resolution of these thermally-excited cantilevers is not as good as that of driven oscillation mass sensors such as quartz crystal microbalances (QCMs) and surface acoustic wave (SAW) sensors. At atmospheric pressure, a driven QCM with f_1 = 2 MHz and Q_1 = 8660 was found to have a resolution of 6.7×10^3 pg/cm^2 [89]. A driven SAW has an even greater mass sensitivity, 10 pg/cm^2 [90]. The greater mass sensitivities of the QCM and SAW are due to their much larger quality factors and the enhancement of the driven amplitude (cf. Eq. 5.34).

Chapter 6

A brief review of methods for fabricating graphene and the properties of graphene

My interest in graphene dates to a proposal I wrote to the National Science Foundation's Graduate Research Fellowship Program (NSF-GRFP) in Fall 2004. I had proposed to use STM and AFM to measure the normal and lateral conductance of few-layer graphene (FLG) sheets. Since graphene can be conceptualized as an "un-zipped" single wall carbon nanotube (SWNT), the conductance of graphene was to have been compared to that of the well-studied SWNTs. Novoselov and Geim's paper reporting the fabrication of exfoliated graphene was published just before I submitted the NSF-GRFP application [91]. This application was not funded, although I did receive an honorable mention from the NSF.

As my research on MWNT vibrations progressed, interest in graphene by the scientific community ignited. Furthermore, alternative methods of preparing graphene were discovered. Researchers at the Birck Nanotechnology Center at Purdue University who had experience in growing SiC for high-power device applications began investigating epitaxial graphene grown on SiC. Scanning probe microscopy studies were needed to understand the nature of the graphene growth. I took advantage of this opportunity to study epitaxial graphene and performed the following STM studies detailed in Chapter 7.

Section 6.1 briefly introduces the fundamental physics of graphene and a presents few proposed applications utilizing graphen. As I studied only epitaxial graphene, a literature review on the growth methods of epitaxial graphene is given in section 6.2. Section 6.3 briefly describes other methods of graphene formation, namely graphene exfoliation, chemical vapor deposition (CVD) of carbon on transition metals, and reduction from graphene oxide.

6.1 Motivation for studying graphene: fundamental physics and applications

Graphene is unique in that it is a stable, one-atom thick, zero-band gap semi-metal [92]. Since the chemical potential of graphene exactly crosses the Dirac point, electrons in ideal graphene behave as massless Dirac fermions. The Fermi velocity, v_F, of the electrons is only 300 times slower than the speed of light [93]. Due to the relativistic Fermi velocity, a number of fundamental

physics properties can be observed in graphene. Those properties observed include the ambipolar electric field effect, the anomalous integer quantum hall effect [92, 93], and the Shubnikov-de Hass effect [94]. The above physical properties are primarily observed in pristine exfoliated graphene in ultra-high vacuum, liquid helium temperature, and/or large magnetic fields. A number of practical applications for graphene, such as its use in high-speed transistors and as a transparent, conductive electrode, also drive graphene research.

Because electrons in graphene travel so rapidly, graphene can be used to fabricate transistors which operate at GHz frequencies. Lin *et al.* recently fabricated transistors from exfoliated graphene deposited on SiO_2/Si substrates. By decreasing the width of the gate from 500 nm to 150 nm, the cut-off frequency was raised from 3 to 26 MHz. Transistors have also been fabricated from epitaxial graphene [95] and from CVD-graphene grown on Ni [96].

One near-term potential application for graphene is its use as transparent, conductive electrodes for LCDs and dye-synthesized solar cells. Currently, most transparent electrodes are made of indium tin oxide (ITO), however, indium is a limited resource.

Blake *et al.* fabricated a liquid crystal device using a 1 ML flake of exfoliated graphene as one of the two conducting electrodes; the transparency of this device decreased from 98 percent to nearly 0 percent as the voltage across the cell was increased from 8 to 100 V [97]

Wang *et al.* fabricated solid state dye-synthesized solar cells using a electrodes composed of overlapping graphene flakes with a net thickness of 10 nm. These graphene electrodes were created by depositing graphene oxide (GO) flakes onto transparent substrates such as quartz, then annealing the GO to form graphene flakes. The power conversion efficiency of these graphene solar cells was 0.26 percent, a factor of three smaller than the 0.84 percent efficiency of similar solar cells with fluorine tin oxide electrodes [98].

6.2 Epitaxial graphene growth on SiC

Silicon carbide is composed of planes of Si and C atoms arranged such that each Si atom is tetragonally bonded to four C atoms and each C atom is tetragonally bonded to four Si atoms. This tetragonal bonding results in a SiC bilayer with one plane composed of Si atoms and the other plane composed of C atoms. At least 75 polytypes of SiC exist; these polytypes are distinguished by slight variations in the stacking of the tetragonal bilayers [99]. The most commonly-studied polytypes of SiC are the cubic (zinc blende) 3*C*-SiC polytype and the hexagonal 4*H*-SiC and 6*H*-SiC polytypes [100]. The naming of the polytypes reflects the structure; the crystalline structure of the polytype repeats every three, four, or six bilayers aligned along the c-axis. The *'C'* and *'H'* refer to a cubic or hexagonal structure [101]. For the purposes of this thesis, it is important to note that all three of these polytypes have a polar faces; one basal plane is composed of C atoms, the other of Si atoms. For the hexagonal polytypes, SiC(0001) is the Si-face and SiC($000\bar{1}$) is the C-face. Epitaxial graphene is primarily grown on the hexagonal polytype.

Epitaxial graphene is grown on SiC by annealing the SiC to high temperatures (1100 – 1600°C)

in low vacuum or UHV vacuum environments. Since Si has a lower vapor pressure than C, the Si atoms sublime and the remaining C atoms reconstruct to form graphitic films on the SiC. Epitaxial growth of graphitic films on SiC(0001) was reported in 1975 by van Bommel *et al.* [102]. Forbeaux *et al.* reported a higher rate of graphitization for the C-face, 6*H*-SiC(000$\bar{1}$) than for the Si-face, 6*H*-SiC(0001). The C-face graphitic films were polycrystalline with significant azimuthal disorder; the Si-face graphitic films were single-crystalline [100, 103].

Despite nearly thirty years of research on epitaxial graphite growth, until exfoliated monolayer graphene was reported in 2004 epitaxial graphite was of only moderate interest. The Web of Science citation record for Forbeaux *et al.*'s 1998 report of heteroepitaxial graphite on SiC received 23 citations through December 2004 but 95 citations for January 2005 – 26 April 2009. The report of monolayer epitaxial graphene formation on the Si-face of SiC in 2006 [104, 105] spurred further epitaxial graphene research. Recent epitaxial graphene research has yielded methods to produce monolayer and few-layer graphene. The monolayer and few-layer graphene grown on SiC have similar structures and disorder as the ultra-thin epitaxial graphite films.

Epitaxial graphene growth on both the C-face and Si-face of SiC occurs first at low binding energy locations, namely step edges and point defects. The rate of graphene growth is governed by the detail balance equation,

$$\mathrm{SiC} \rightleftharpoons \mathrm{Si(vapor)} + \mathrm{C(graphene)}.$$

The rate of graphene growth increases with increasing growth temperature and decreasing Si vapor pressure. Ideally, as the growth temperature or growth time is increased, the small initial patches of graphene growth would merge into a continuous, uniform 1-ML thick graphene film. However a number of defects, including the formation of graphene pits [106] on the Si-face, limit the quality of the graphene growth.

Recent reports show that slowing the rate of graphene growth leads to higher quality graphene. Epitaxial Si-face graphene, grown either with a disilane back pressure [107] or an argon atmosphere of $\sim$760 Torr [108], has larger graphene domains and higher Hall mobilities than Si-face graphene grown under UHV conditions. Epitaxial C-face graphene, 5 ML thick, has been grown in UHV [109] and pressures of 0.1 mTorr [110]. The UHV-grown graphene had high azimuthal disorder and showed signs of stretched and otherwise deformed graphene lattices, as evidenced by variable periodicity moiré regions [109]. While the graphene grown at 0.1 mTorr also had some regions of rotational disorder, there were also many few μm^2 areas of uniform graphene [110].

6.3 Other methods of producing graphene: exfoliation, chemical vapor deposition, and reduction from graphene oxide

Mechanical exfoliation was the first method used to produce individual graphene sheets [91]. To form mechanically-exfoliated graphene, adhesive tape is used to cleave bulk graphite or HOPG. Initially, tens to hundreds of graphene monolayers may stick to the adhesive tape. The graphite sample is repeatedly cleaved using the adhesive tape. This resulting flakes are then deposited onto

an SiO_2/Si wafer. Using optical microscopy, the location and thickness of the graphene flakes are identified by the color of the flakes. Since the optical detection method relies on an interference-like contrast between the graphene and the SiO_2/Si substrate, the thickness of the SiO_2 layer – 300 nm – is critical [92]. Exfoliated graphene has the highest electron mobilities of any form of graphene, greater than 15,000 $cm^2/(V\ s)$ [111], but is clearly not suitable for mass-production.

Chemical vapor deposition (CVD) can be used to grow graphene on transition metal substrates, such as Ni. A thin fim, 500 nm thick, of Ni is evaporated onto an SiO_2/Si substrate. The Ni is then annealed to promote single-crystal domains. The CVD growth on the Ni/SiO_2/Si substrate occurs at 900–1000°C; the precursor gas is a mixture of methane and hydrogen. At the growth temperature, the methane molecules crack and the C atoms become saturated in the Ni. As the sample cools to room temperature, the C atoms precipitate out of the Ni and a graphene film, 1–12 ML, forms on the Ni surface. The thickness of the graphene layers is proportional to the thickness of the Ni film. However, thinner Ni films also have smaller Ni grain sizes, which leads to more defects in the graphene layers [96].

A wet transfer technique can be used to transfer the graphene films to nonspecific substrates. Prior to transfer, a PMMA layer is deposited on top of the graphene films; the Ni is then dissolved using hydrochloric acids. These graphene films, optimally 1–2 ML thick and a few cm^2 can be transfered to other substrates. Raman and electron diffraction studies show that these films have a slightly disordered stacking of graphene layers. The optimum films produced in this manner are 1–2 ML thick, a size of a few cm^2, and have an electron mobility of 100–2000 $cm^2/(V\ s)$ [96].

Lastly, sheets composed of overlapping graphene flakes can be prepared by chemically reducing graphene oxide (GO). Eda *et al.* used a vacuum filtration method to deposit thin films, 1–2 nm thick, of GO onto glass and plastic substrates. After deposition, the GO was reduced to graphene by exposing the GO films to hydrazine vapor and annealing the fils in vacuum at 200 C. An advantage of this technique is that graphene flakes can be deposited over large areas of flexible, transparent, and/or insulating substrates. However the electron mobilities of these graphene films is low, only 0.2 $cm^2/(V\ s)$[112].

Chapter 7

Insights into Few-Layer Epitaxial Graphene Growth on 4H-SiC(000$\bar{1}$) Substrates from STM Studies

7.1 Introduction

The production of high-quality materials with nanoscale size and reduced dimensionality is desirable for many advanced electronic applications. [1] Materials like two-dimensional (2D) graphene, one-dimensional (1D) carbon nanoribbons, and 1D carbon nanotubes represent a class of new materials that may well serve as the building blocks for future carbon-based nanoelectronics. Because of the reduced dimensionality of these emerging new materials, electron transport properties are expected to be strongly affected by disorder introduced by impurities, topological defects, or long range deformation modes [113]. In nanomaterials, such disorder will cause unwanted quantum interference effects leading to increased scattering, unwanted localization, and an overall degradation in electronic performance. For this reason there is a pressing need to better characterize defects in any carbon-based nanomaterial.

A promising large area technique for graphene synthesis is to anneal in high vaccum a (000$\bar{1}$) silicon carbide (SiC) substrate to produce epitaxial carbon layers. Graphene-like sheets form in a complex process initiated by the sublimation of Si atoms and the formation of a carbon-rich surface containing mobile carbon atoms. Surface diffusion of carbon at elevated temperatures produces stacked sheets of planar, six-fold coordinated carbon atoms.

A priori, it is possible to imagine a myriad of problems that may limit the quality of graphene layers that form on SiC. To begin, a high quality SiC substrate is needed since a substrate surface full of step edges, localized defects, and microstructures will likely hinder atomic diffusion and thereby degrade the quality of the graphene layers formed. To obtain the highest quality single or bilayer graphene, a growth temperature that optimizes carbon atom diffusion with respect to Si atom sublimation must be determined. Because of the weak interaction between layers in stacked graphene, it is likely that shifts in atom stacking can develop between two adja-

[1] Portions of this chapter were previously published in Ref. [110], L. B. Biedermann, M. L. Bolen, M. A. Capano, D. Zemlyanov, and R. G. Reifenberger, "Insights into few-layer epitaxial graphene growth on 4H-SiC(000$\bar{1}$) substrates from STM studies," *Phys. Rev. B* 79, 125411 (2009). Please see the copyright statement in Appendix F.

cent graphene layers. To produce large areas of high quality graphene, carbon grain boundaries must be reduced by both controlling and optimizing the number of C-rich seed regions. Identifying optimal growth conditions that i) minimize the number of atomic scale defects in a graphene sheet [114], ii) minimize the presence of grain boundaries [115], and iii) eliminate interstitial carbon atoms [116, 117, 118, 119, 120] between the graphene sheets presents a formidable challenge. Before fabricating high quality graphene-based electronic devices on an industrial scale, many of these important questions must first be addressed.

Traditional surface characterization tools such as low energy electron diffraction (LEED), Raman, and X-ray photoelectron spectroscopy (XPS) are capable of providing structural and chemical information spatially averaged across the carbon-rich SiC substrate at the millimeter length scale. Low energy electron microscopy (LEEM) can provide structural information with a spatial resolution of $\sim$10 nm. Atomic force microscopy (AFM) can provide useful topographic information for length scales ranging from tens of microns down to nanometers, but cannot address local atomic or electronic structure. To obtain useful information about the quality of the carbon layers at the nanoscale, techniques capable of imaging individual carbon atoms are required. For this purpose, only scanning tunneling microscopy (STM) techniques seem suitable since STM techniques can reveal the atomic rearrangements produced by strains and defects as well as probe the local electronic properties of the graphene layers.

In what follows, we use ambient STM to characterize the atomic-scale structures found on epitaxial few-layer graphene (FLG) grown by heating $(000\bar{1})$ SiC to high temperatures (1450–1600 °C) in vacuum. Such a study is warranted since historically, the C-face is seldom studied because of the wide-spread use of the Si-face in the production of SiC power devices [121]. By careful study of the the atomic-scale STM images for different growth conditions, useful information about the quality of the FLG is obtained and valuable insights into the likely processes influencing the growth of graphene layers can be inferred.

7.2 Superlattices in layered carbon

7.2.1 Defects in highly orientated pyrolitic graphite

The defects likely to occur in epitaxial graphene layers can be inferred from the extensive prior literature on highly orientated pyrolitic graphite (HOPG). Since the mid-1980s, STM has been used to extensively characterize defects in as-prepared HOPG that include (i) monolayer pits, step edges, stacking faults and microholes [122, 123], (ii) pentagonal/heptagonal defective unit cells, (iii) the $\sqrt{3} \times \sqrt{3}R30^o$ superstructure caused by perturbation of the electronic charge density produced by point defects and adsorbed species [124, 125], (iv) 1D superlattices attributed to grain boundaries in HOPG [126], and (v) moiré superlattices [127, 128, 129].

Of particular interest to the current work are the high quality moiré superlattices observed in STM images of HOPG surfaces [127, 128, 129]. The moiré superlattices on HOPG are characterized by a well-defined hexagonal superlattice with periodicities considerably larger than the atomic

spacing between carbon atoms. Moiré regions observed on HOPG frequently have a sharp 1D transition, often described as a "string of beads" [128], between the area supporting a superlattice and an adjacent area characterized by the 0.246 nm atomic periodicity of HOPG. The bead-like features demarcating the sharp boundary between the two regions typically have the same periodicity as the superlattice [129].

The presence of moiré superlattices on HOPG is usually attributed to the rotation of the top graphene sheet with respect to the second layer, which can result from purely mechanical means [128, 130]. In the case of a rotation, the moiré superlattice has a constant periodicity across the moiré region. Alternatively, a screw dislocation can cause a gradual rotation of the top graphene layer in HOPG; the superlattice periodicity around such a dislocation continuously varies with distance [129]. While the origins and manifestations of these superlattices on HOPG are interesting in their own right, the observation of moiré superlattices on FLG grown epitaxially on SiC is relatively new [109].

7.2.2 Superlattices observed in graphene

Three types of superlattices have been reported on epitaxial graphene formed on a SiC substrate. First, for epitaxial graphene grown on the Si-face of SiC, the SiC susbtrate reconstruction can be observed using STM, LEED, or surface x-ray diffraction (SXRD) [131, 132, 133, 104, 134, 135, 136, 137]. As observed by STM and LEED studies of Si-face graphitized SiC, this reconstruction is manifest as a 6×6 or a $(6\sqrt{3} \times 6\sqrt{3})R30^o$ structure [102, 100, 103, 138].

A second type of fixed-periodicity superlattice is the dilation moiré superlattices observed on chemical vapor deposition (CVD) grown graphene on substrates such as Ir(111), Ni(111), Ru(0001), and Pt(111) [139, 140, 98, 141]. In this case, the superlattice is attributed to differences between the lattice constants of the graphene and substrate, not to a rotation between graphene layers.

A third type of superlattice with variable periodicity has been observed on FLG grown on the C-face of SiC. This moiré superlattice is due to the rotation or dislocation of the top graphene layers. Such superlattices were recently reported on epitaxial graphene by Varchon *et al.*, who found six distinct moiré regions within a 150×150 nm^2 STM scan with periodicities ranging from 2.5 to 3.8 nm [109]. The separate moiré regions were bounded by either ridges (called pleats by Varchon *et al.*) or a "string of beads" [109]. By contrast, the C-face reconstructions are not as well studied; J. Hass *et al.* have reported a $(\sqrt{13} \times \sqrt{13})R46.1^o$ superlattice on 4H-SiC(000$\bar{1}$) with STM [142].

7.2.3 Atomic arrangement of moiré superlattices

The origin of the moiré superlattices are an enhancement in the density of states (DOS) which occurs when the topmost layer of graphene is rotated with respect to the underlying layer(s) [143].

The relevant atomic-scale shift between layers of C atoms is illustrated in Fig. 7.1(a) which shows the relevant atomic stacking arrangement for HOPG.

For HOPG with **ABAB** stacking, two types of carbon atoms can be denoted. The α carbon atoms sit above a carbon atom in the underlying layer while the β carbon atoms sit above a hole in the underlying layer. In STM scans of ideal (Bernal stacked) HOPG, only the β atoms, which have a higher density of states (DOS) around the Fermi level, are imaged [144]. When the topmost layer of graphene is rotated with respect to the underlying substrate, a range of atomic arrangements are possible. Three key stacking sequences are shown in Fig. 7.1(b). In **AAB** stacking, each atom in the top layer is directly above an atom in the next lower layer. In **BAB** stacking, the rotation preserves the standard Bernal arrangement. An intermediate case is referred to as the **slip B** stacking. In this case, the **BAB** stacking is offset slightly such that neither atom in the top layer is directly above an atom in the next lower layer.

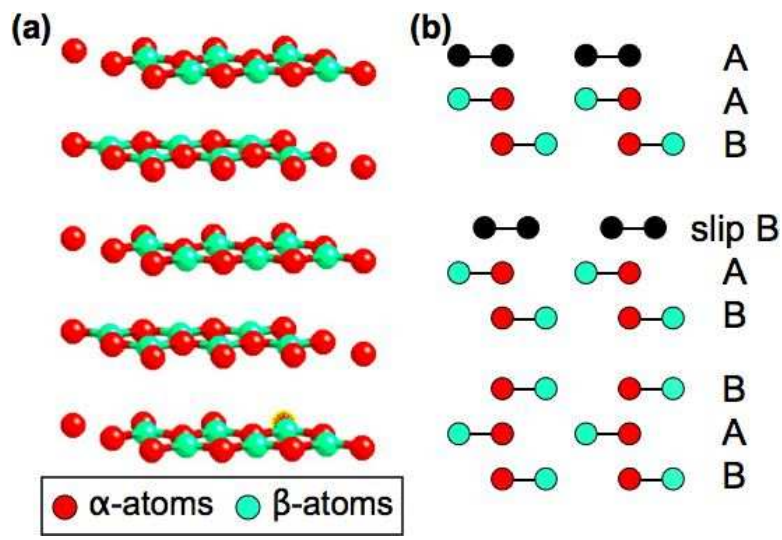

Figure 7.1. In the Bernal stacking of HOPG (a), the layers alternate **ABAB**. (b) A rotation of the top graphene layer of the HOPG can lead to **AAB**, **slip B**, or **BAB** stacking sequences.

Using density functional calculations, Campanera *et al.* found that the moiré superlattices observed by STM could be replicated by a model using four layers of *BA*-stacked graphite, where the top layer was rotated with respect to the bottom layers [143]. The brightest features observed in STM images of the moiré patterns correspond to the **AAB** stacking, which was found to have the highest DOS. Dim features correspond to the **slip B** stacking, while the darkest features correspond to the standard **BAB** Bernal stacking of HOPG. Furthermore, Campanera *et al.* calculated a relative formation energy cost of a few meV/atom, with a higher energy cost corresponding to larger observed periodicities [143].

The superlattice periodicity can be characterized by a length $\mathscr{D}$ given by

$$\mathscr{D} = \frac{a}{2\sin(\Theta/2)}, \tag{7.1}$$

where a is the basal lattice constant (0.246 nm for HOPG) and Θ is the rotation angle between two layers of the hexagonal lattice. The orientation of the moiré lattice with respect to the atomic orientation of the top graphene layer is given by ϕ, where [129]

$$\phi = 30^o - \Theta/2. \tag{7.2}$$

As evident from Eq. 7.1, a small rotation angle, Θ, corresponds to a large superlattice periodicity, $\mathscr{D}$.

It is important to note that the moiré superlattices are atomically flat; the apparent enhanced corrugation is an DOS effect. The presence of moiré superlattices implies that electrons in FLG traversing a region containing the superlattice are subjected to a sinusoidal potential with a periodicity determined by the relative angle of rotation between the top two graphene sheets. Since the moiré superlattice is a DOS effect, the prominence of this superlattice depends on the bias voltage and tunneling current. The moiré superlattice is most prominent when the STM tip is closest to the sample, which corresponds to small bias voltage and large tunnel currents.

7.3 Experimental considerations

7.3.1 Graphene growth

Three inch diameter *4H*- SiC wafers (Cree, high purity, semi-insulating) with a nominal off-cut angle of 0° were used throughout this study. The as-received SiC wafers were polished by NovaSiC to remove scratches and other surface defects. The wafers were then diced into 8×8 mm^2 substrates and cleaned.

The FLG samples were grown on the carbon face of the SiC(000$\bar{1}$) substrates in an Epigress VP508 hot-wall chemical vapor deposition reactor. The temperatures reported in this study were determined using a Heitronics KT81R two-color rationing pyrometer (spectral bands 0.7 μm and 1.2 μm) with a calibration traceable to the melting temperature of Si, 1410 °C.

Prior to carbon growth, the SiC substrates were hydrogen annealed at 1600 °C to etch residual polishing damage. The temperature was reduced to 700 °C and the pressure was reduced to 2×10^{-7} mbar. The temperature was then ramped up to a growth temperature between 1475 °C and 1600 °C to form continuous carbon layers. The SiC substrate was held at the growth temperature for 10 minutes before the sample was cooled under vacuum [95] and prepared for characterization by XPS and STM.

7.3.2 XPS considerations

The XPS data were obtained with a Kratos Ultra DLD spectrometer using monochromatic Al Kα radiation (hν = 1486.58 eV). Survey and high-resolution spectra were collected at fixed analyzer

pass energies of 160 eV and 20 eV, respectively. The spectra were collected at 0, 30, 45, 52, 60° with respect to the surface normal (photoemission angle θ). All binding energy (BE) values refer to the Fermi level. The charge shift was corrected to the C 1s peak set at 284.5 eV for the graphitic component [105]. The standard deviation of the peak position associated with the charge reference procedure was $\pm$0.05 eV. The data were analyzed with commercially available software, CasaXPS (version 2313Dev64). The spectra were fitted by a Gaussian-Lorentzian function after linear or Shirley type background subtraction.

7.3.3 STM considerations

Ambient STM scans were performed using a Nanotec Electronica STM. The scans were performed under a bell jar that was back-filled with dry nitrogen to atmospheric pressure. The X, Y, and Z piezos were calibrated using the known atomic lattice (0.246 nm) and mono-step height (0.335 nm) of HOPG.

In order in increase the stability of the STM, the sample was frequently placed in the STM, under dry nitrogen, 3–12 hours before scanning. Placing the sample in the STM ahead of scanning allowed the piezo and sample to come to a thermal equilibrium, which minimized drifts. The STM head was withdrawn 1–3 mm from the sample to protect the STM tip. A scan range of $\sim 1 \times 1\,\mu\text{m}^2$ is set to exercise the tube piezo which controls the sample's motion. (In the Nanotec Electronica STM, the STM head is fixed and the sample is rastered beneath it.) When the tube piezo is exercised in such a manner, the scan size should be $\sim$10 percent of the maximum scan range. Larger scans, which correspond to large voltages on the piezo, can lead to break-down of the piezo. Smaller scans are not as efficient at the aligning domain boundaries within the piezo that can cause non-linear piezo motion.

In practice, the graphene-STM samples were often scanned for two or three consecutive days. The first day was spent identifying representative regions of the sample and/or searching for moiré regions. To check the quality of the STM tip, particular attention was paid to the shape of step edges. The sample was also rotated 90° to check for multiple-tip effects. At the end of the day, the STM tip was positioned over an interesting region and withdrawn 1–3 mm before exercising the piezo overnight. The following day, the STM would be extraordinarily stable and the region of interest could be readily scanned with atomic resolution.

Typical scan parameters included a 0.1–5 nA tunnel current (I_{set}) and a bias voltage of 0.05–5 V (V_{bias}). STM scan sizes ranged from 2×2 nm^2 to $5 \times 5\,\mu\text{m}^2$. Typical image acquisition times ranged from 30 s to 10 mins. All STM scans presented were obtained using a cut PtIr tip. The majority of the scans were taken in the constant-current mode; a few of the atomic-resolution scans were taken in the constant-height mode (Fig. 7.10). Nanotec Electronica's WSxM software program was used for both data acquisition and image processing [145]. The STM scans of epitaxial graphene presented in this chapter represent only a small fraction of the few thousand of STM scans acquired and analyzed. Table 7.1 correlates the STM scans with the sample number and growth temperature.

Table 7.1. Five C-face epitaxial graphene samples were studied in depth with STM and AFM. Only AFM scans are presented for samples 924 and 926, which had incomplete graphene coverage. The growth temperatures and figures acquired from these samples are tabulated below.

Sample	Growth Temp. (°C)	Figures
926	1350	7.3(a) (AFM scan)
924	1450	7.3(b) (AFM scan)
985	1475	7.3(c), 7.5
976	1500	7.3(d), 7.4(b), 7.6–7.8, 7.10–7.12
971	1500	—
927	1550	7.3(e), 7.4(a), 7.13, 7.14
9xx	1600	7.3(f), 7.9

7.3.4 Preparation of epitaxial graphene samples for STM

The most important criteria for sample preparation of the graphene-SiC samples were (1) to minimize surface contamination and oxide formation by always storing and scanning the samples under dry nitrogen and (2) to use vacuum-compatible sample mountings so that the samples could later be examined via XPS. To avoid contaminating the samples with finger oils, nitrile gloves were always worn while handling the samples.

The graphene-SiC samples were mounted on 15-mm diameter steel mounting disks (SPI supplies, part number 07620-AB) with a piece of 3M double-sided copper tape (SPI supplies, part number 05085-AB) sandwiched between the sample and mounting disk. Both the steel mounting disk and copper tape are compatible with the vacuum environment of the XPS. In order to ground the surface of the graphene-SiC sample, one or two short pieces of copper tape placed across a top corner(s) of the sample provided a conductive path between the top surface of the graphene-SiC and the grounded mounting disk.

7.4 XPS confirmation of graphitic carbon and estimation of graphene thickness

Systematic angle-resolved XPS studies were performed on FLG samples. Of prime interest were confirmation of graphene growth and a non-intrusive estimate of FLG thickness. For this reason, we focus on the FLG samples grown at 1475°C, and 1500°C. Figure 7.2 shows an example of the C 1s core level spectrum obtained from a FLG sample grown at 1500 °C; the spectrum from a reference HOPG sample is shown for comparison as well. The spectra from both HOPG and the 1500 °C FLG sample show a main peak at 284.5 eV, indicating the presence of sp^2 hybridized C-C

bonds. This peak at 284.5 eV is a signature of graphitic carbon [146]. The small peak at 283.0 eV in the XPS spectrum from graphene-SiC sample is assigned to carbon bound to silicon [147, 146].

Another signature of graphitic carbon is a weak peak at ca. 291 eV, which is identified as a shake-up satellite of the peak at 284.5 eV. The shake-up satellite is a well-established characteristic of the photoemission process in aromatic and graphitic systems [148]. The shake-up is a two electron phenomenon; the emitted photoelectrons with energy 284.5 eV can excite a $\pi \rightarrow \pi^*$ transition resulting in an additional peak at higher BE. Aromatic and graphitic systems show a shake-up peak shifted towards higher BE from the main peak by ca. 6.5-7 eV with an intensity ranging up to 5–10 percent of the graphitic peak [148].

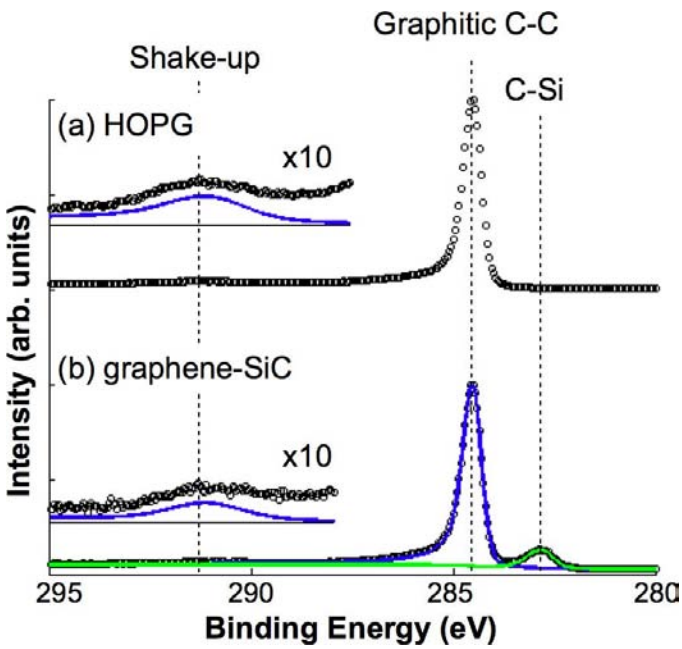

Figure 7.2. The C-1s XPS spectra, collected at $\theta = 0^o$, from a reference HOPG substrate (a) and from a FLG sample grown at 1500 °C on SiC (b). The similarity of the two XPS spectra indicates the presence of graphitic carbon on SiC. Both spectra were obtained at a photoemission angle of 0°. A closer examination of the region between 288 eV and 295 eV from both samples provides evidence for shake-up satellites (insets). (Reprinted with permission from Ref. [110]. Copyright 2009 by APS.)

In order to estimate the thickness of the graphitic carbon from XPS data, we utilized the approach proposed by Fadley [149]. Assuming the graphene-SiC sample can be modeled as a semi-infinite SiC substrate with a uniform graphene overlayer of thickness t, t can be calculated from the ratio between the intensity of the graphitic component at 284.5 eV from the graphene overlayer,

$N_G(\theta)$, and the intensity of the SiC component at 283.0 eV from the SiC substrate, $N_{SiC}(\theta)$:

$$\frac{N_G(\theta)}{N_{SiC}(\theta)} = \frac{\rho_G \Lambda_e^G(E_{C1s})}{\rho_{SiC}\Lambda_e^{SiC}(E_{C1s})} \left(\frac{1 - exp(\frac{-t}{\Lambda_e^G(E_{C1s})\cos\theta})}{exp(\frac{-t}{\Lambda_e^G(E_{C1s})\cos\theta})} \right). \tag{7.3}$$

Here ρ_G and ρ_{SiC} are the densities of carbon atoms in graphene and SiC in atoms per cm^3, respectively. Λ_e^G and Λ_e^{SiC} are the attenuation lengths for the C 1s photoelectron with kinetic energy E_{C1s}. The quantities Λ_e^G =3.10 nm and Λ_e^{SiC}=2.58 nm were calculated using NIST SRD-82 [150]; details of this calculation and the derivation of Eq. 7.3 are explained in the supporting information of Ref. [110]. The peak intensities, $N(\theta)$ also depend on physical parameters of the spectrometer and electron analyzer, but these parameters are the same for both $N_G(\theta)$ and $N_{SiC}(\theta)$ and thus cancel.

The XPS spectra can be fit by two components, as shown in Fig. 7.2, and the ratio between the graphene and SiC components, $N_G(\theta)/N_{SiC}(\theta)$, can be accurately measured. Since $N_G(\theta)/N_{SiC}(\theta)$ was measured over a range of θ between 0° and 60°, a least-squares fit to Eq. 7.3 was used to determine t. For more information on the thickness calculation, please see the supplementary information. Since the XPS spot size is 0.4×0.7 mm, the thickness estimate represents an average value characterizing the FLG thickness across a few hundreds of microns. In this way, the average thickness of the FLG grown at 1500 °C was found to be 2.4 ± 0.2 nm, or approximately 7 monolayers (ML) of graphene. Using the same XPS analysis method, the average thickness of the FLG grown at 1475 °C was found to be 1.8 ± 0.1 nm, or approximately 5 ML of graphene. These thickness values provide a convenient benchmark to qualitatively estimate the thickness of FLG formed at different growth temperatures.

7.5 STM study of the C-face growth

In what follows, we discuss in turn the nanoscale features that have been found on FLG using STM. These features are useful for providing insight into graphene growth.

7.5.1 General observations

AFM studies [151] show the SiC substrate (carbon face) to be stepped, with flat terraces a few hundred nanometers wide. The terraces are terminated by steps ranging in height from ~0.5 nm to ~2 nm. The flat terraces occasionally show rough features, presumably due to inadequate chemo-mechanical polishing.

A wide growth temperature range, 1350—1600 °C, was investigated to better understand the growth mechanisms of graphene on SiC. Parallel XPS and AFM studies [151] provided evidence that at temperatures below 1475 °C, the carbon coverage was sufficiently sparse that continuous FLG was not formed [Fig. 7.3(a and b)]. The samples grown at these lower temperatures were not extensively studied by STM since the low electrical conductivity of the exposed SiC substrate led to an unstable tunnel current.

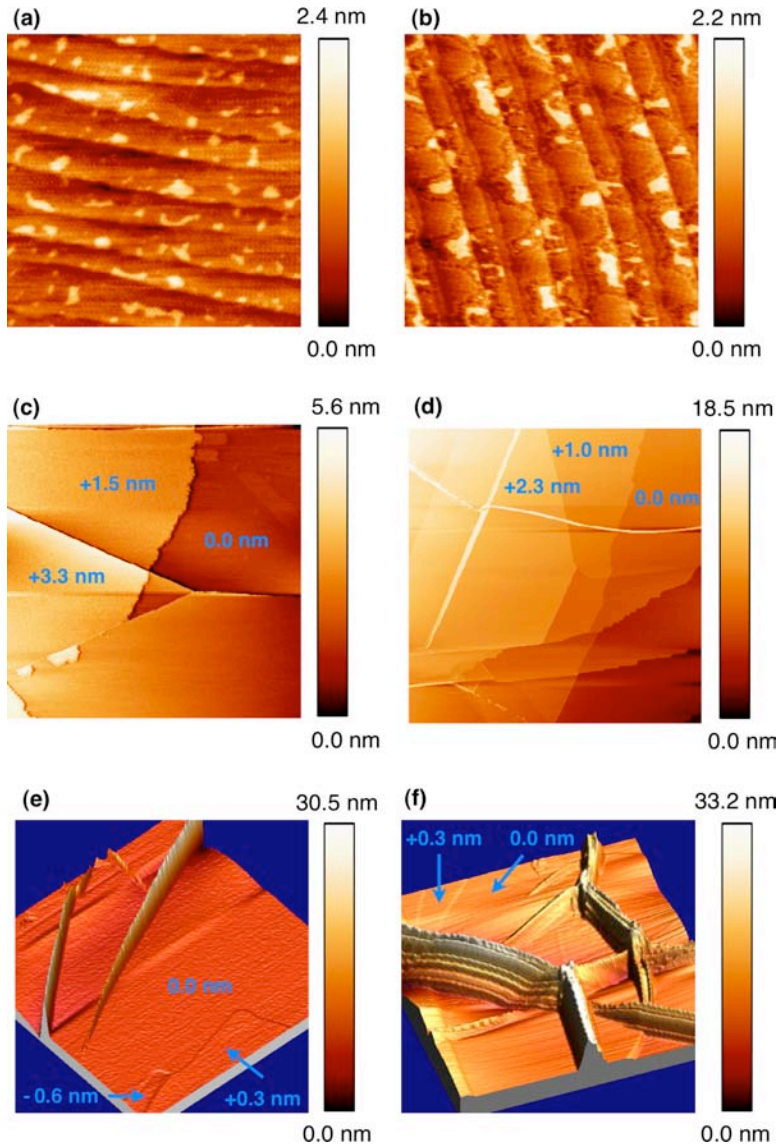

Figure 7.3. A gallery of $2 \times 2\,\mu\text{m}^2$ AFM (a-b) and STM (c-f) scans showing the stages of graphene growth. In (a) and (b), sparse patches of graphene growth on the SiC step edges are observed at 1350°C and 1450°C. At 1475°C (c), the SiC substrate is entirely covered with graphene. At 1500°C (d) and 1550°C (e), a network of ridges and wrinkles appears. At 1600°C (f), faceted ridges, intersecting at angles near 120°, separate regions of smooth FLG.

At growth temperatures of 1475°C [Fig. 7.3(c)] and above, the SiC surface was continuously covered with graphene; STM was extensively used to image these samples. Intersecting networks of graphene ridges were found at growth temperatures of 1500°C [Fig. 7.3(d-f)] and above. In what follows, the above observations are discussed in detail.

Pits in the substrate

Occasionally, large pits (∼0.3–1.0 μm wide) surrounded by multiple graphene ridges were found. These defects were rare and are thought to be formed from screw or edge dislocations in the SiC substrate. It is likely that the hydrogen etching procedure enhanced these defects [152]. If a such a pit as in Fig. 7.4(b) were found, the tip would be moved to a new region of the sample. These pit defects show the variability of the epitaxial graphene grown on the C-face. Figure 7.4(a) and fig. 7.13 are from the same sample 927, grown at 1550°; fig. 7.4(b), fig. 7.8, and 7.9 are from the same sample 976, grown at 1500°. Excepting Fig. 7.4, all STM scans presented were taken away from such pits.

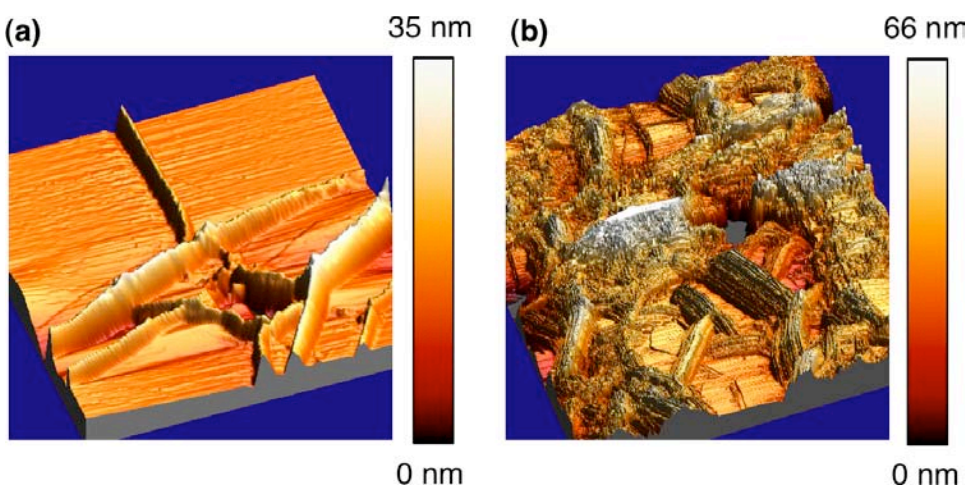

Figure 7.4. Two examples of ridges surrounding pits in the substrate. In (a), a $2 \times 2\,\mu m^2$ region showing a small pit completely surrounded by ridges (sample 927, grown at 1550°). In (b) a $7.5 \times 7.5\,\mu m^2$ region showing the highest ridge density observed on these epitaxial graphene samples (sample 976, grown at 1550°). Scan parameters are I_{set} = 1.0 nA for (a) and (b) and V_{bias} = 300 mV for (a) and 500 mV for (b).

7.5.2 Rough Graphene

At growth temperatures of 1475 °C, smooth graphene-like surfaces of $t = 1.8 \pm 0.1$ nm (XPS measurement) allowed reliable and reproducible STM studies. The graphene that formed at this growth temperature showed two morphologies that we name smooth graphene and rough graphene. An STM image of these two regions is provided in Fig. 7.5(a). A step edge of 1.4 nm separates the smooth and rough regions. The smooth graphene, as confirmed by atomic resolution scans, was atomically flat and provided evidence for monolayer C step heights of 0.3 nm. The rough graphene had an rms roughness of typically 0.15–0.20 nm and showed peak to valley heights of ∼0.2–0.5 nm (Fig. 7.5(b)). In spite of the roughness, it was possible to obtain atomic resolution scans over small 4–10 nm^2 regions. Fourier transforms (FFT) of atomic resolution scans yielded a hexagonal periodicity of 0.22 ± 0.01 nm, indicating the presence of graphene.

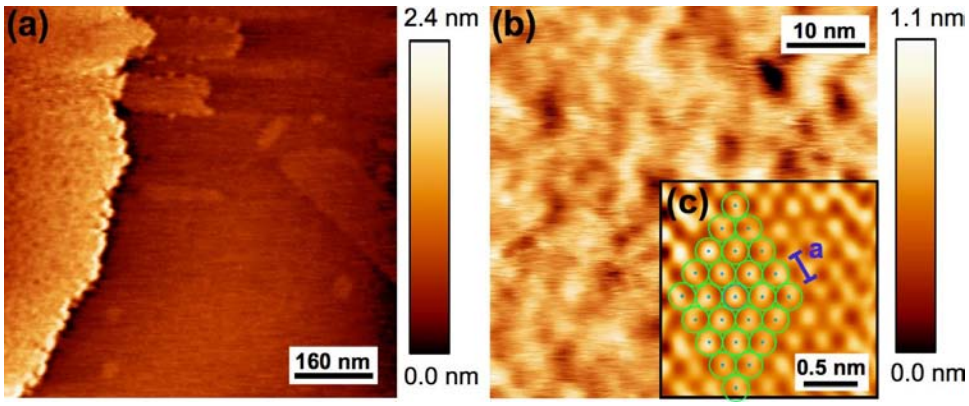

Figure 7.5. STM images of graphene grown at 1475 °C shows the two growth morphologies. In (a), an 800 × 800 nm^2 region, the rough graphene region is on the left while the smooth graphene region is on the right. In (b), a 50 × 50 nm^2 image showing the detailed morphology of the rough graphene. In (c), a 2 × 2 nm^2 atomic resolution image of the rough region in (b) reveals a hexagonal lattice. The lattice parameter, $a = 0.245$ nm of the hexagonal lattice indicates the presence of graphene. The original STM scan was processed with wavelet analysis [153]. Scan parameters are I_{set} = 5.0 nA and V_{bias} = 72 mV for (a) and I_{set} = 3.0 nA and V_{bias} = 100 mV for (b) and (c). (Reprinted with permission from Ref. [110]. Copyright 2009 by APS.)

We find evidence for grain boundaries in rough graphene formed at a growth temperature of 1500 °C ($t = 2.4 \pm 0.2$ nm, XPS measurement). This is illustrated in Fig. 7.6(a) which shows a grain boundary separating two regions of rough graphene. The width of the boundary is ∼50 nm. A more detailed STM image of the boundary region is provided in Fig. 7.6(b). This figure shows randomly oriented parallel 1D features with a periodicity of ∼4 nm. These localized, 1D features have only been observed in the rough graphene regions of the substrate.

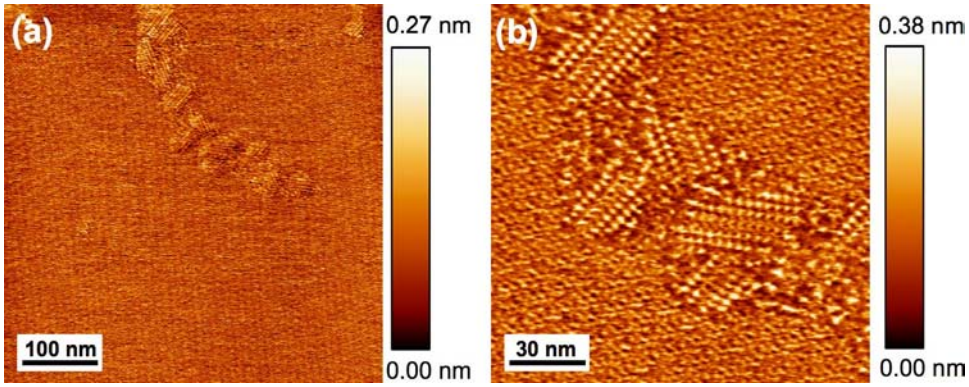

Figure 7.6. STM images of a region from the graphene grown at 1500°C. In (a), a 500 × 500 nm^2 image showing the presence of a grain boundary in the upper half of the image. In (b), a 150 × 150 nm^2 image showing the parallel 1D features within the grain boundary. Scan parameters are I_{set} = 2.0 nA and V_{bias} = 100 mV for (a) and (b). (Reprinted with permission from Ref. [110]. Copyright 2009 by APS.)

7.5.3 1D superlattice on smooth FLG

We have observed 1D superlattices that cut across smooth regions of FLG. An example of such a defect on sample 2, grown at 1500°C, is shown in Fig. 7.7(a). Two fiducial lines *AB* and *CD* are drawn parallel to each other. The resulting angles between the fiducial lines are $\angle ABC = 141^o \pm 5^o$ and $\angle CDE = 136^o \pm 5^o$, indicating that the 1D superlattice is bent from a straight line by an average angle of about $42^o \pm 5^o$ The periodicity of the 1D superlattice is well-defined and equal to 7.0 nm between points A and B (see Fig. 7.7(b)). This 1D feature resembles a 1D moiré superlattice reported on HOPG that contained a 30° bend and was attributed to a grain boundary in the graphene layer [126].

7.5.4 Ridges and wrinkles on FLG

As the epitaxial graphene cools from the growth temperature, the SiC substrate contracts more than the FLG. This contraction leads to the formation of graphitic ridges and wrinkles. Ridges are contractions of multiple graphene layers and terminate in nodes. Wrinkles terminate into the smooth portion of the graphene [151]. As seen in Fig. 7.3, the ridges become wider and more pronounced as the growth temperature increases.

At growth temperatures of 1500°C, the FLG ($t = 2.4 \pm 0.2$ nm, XPS measurement) exhibited atomically smooth surfaces across large regions of the underlying SiC substrate. In addition, fine ridge-like features, up to ∼10 nm tall, begin to form boundaries around the atomically smooth, FLG domains. In many cases, the ridges cross step edges in the underlying SiC substrate with

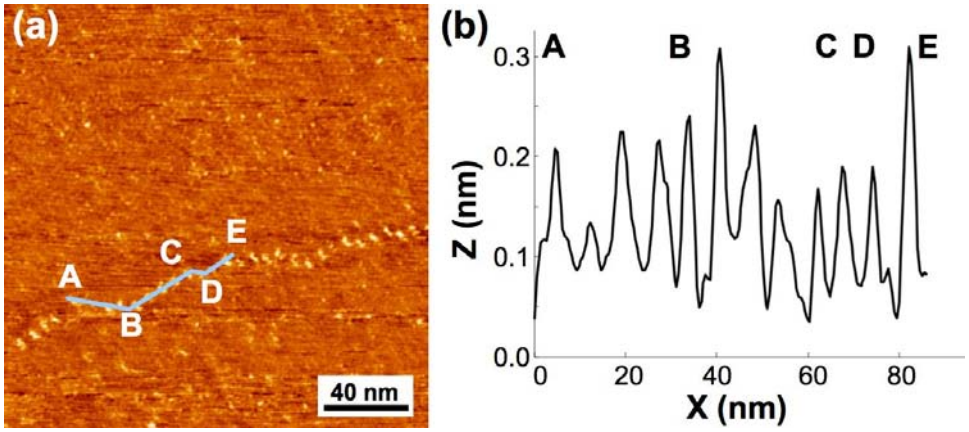

Figure 7.7. (a) An STM image of a 200 × 200 nm^2 region shows a 1D superlattice. (b) A line profile along the line *ABCDE*, which follows the profile of the 1D superlattice. Scan parameters are I_{set} = 2.0 nA and V_{bias} = 300 mV. (Reprinted with permission from Ref. [110]. Copyright 2009 by APS.)

no change in height or direction (see Fig. 7.8(a)). Occasionally, ridges form on step edges, as is the case for the 6-nm high ridge, which is located on a 4.5-nm step edge (see Fig. 7.8(b)). The formation of a ridge that exactly follows a step edge suggests that step edges in the underlying SiC substrate might provide a diffusion barrier to mobile carbon atoms at 1500 °C.

As the growth temperature increases beyond 1500 °C, the ridges appear to coalesce into much taller, wider folds (up to ∼20 nm high) that form boundaries encompassing larger areas of smooth FLG [see Fig. 7.3(f)]. Buckled ridges, characterized by parallel features 10s of nanometers wide, are common at the higher growth temperatures [see Fig. 7.8(d-f)]. STM I(V) measurements on the ridges show a linear behavior that is indistinguishable from I(V) data acquired on the nearby flat regions of the FLG. Frequently, the ridges intersect with angles near $\sim 120^o$ [Fig. 7.3(f)]. These ridges of graphene are thought to be caused by the thermal expansion mismatch between graphene and SiC [142, 151]. Similar ridges are observed on CVD-graphene grown on Ni [140].

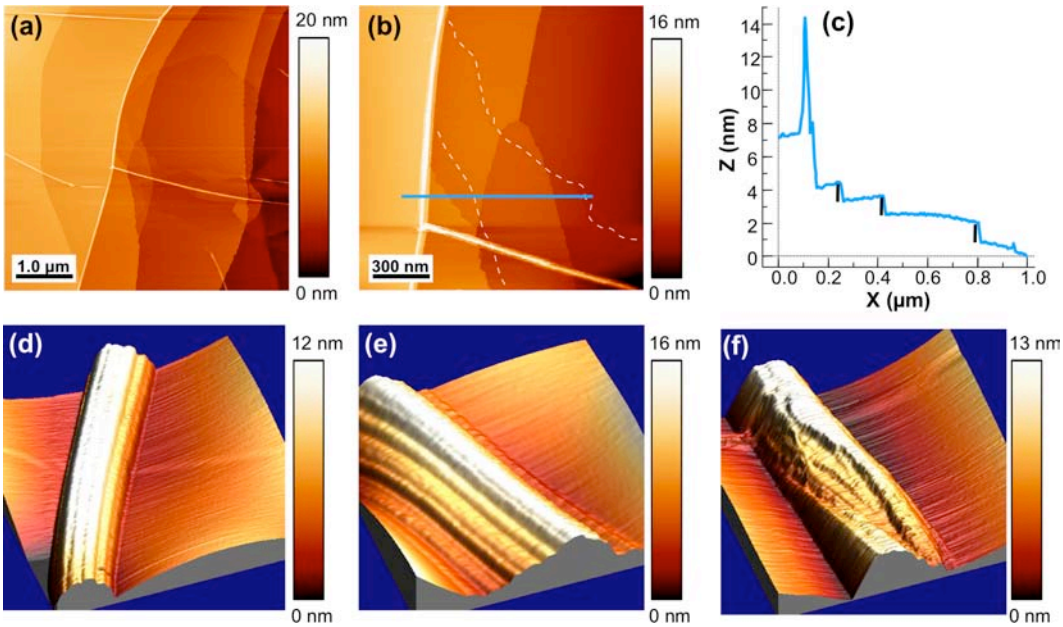

Figure 7.8. STM images of epitaxial graphene grown at 1500 °C (a-c) and 1600 °C (d-f). (a) An STM image (a) of a $5 \times 5\,\mu m^2$ region shows fine ridges, 5–10 nm high, crossing the sample. (b) A $1.5 \times 1.5\,\mu m^2$ region, located in the center of (a), reveals a superlattice, the boundaries of which are indicated by the dashed lines. This superlattice is bounded by the ridge on the left-hand side and is discussed further in Fig. 7.11. A profile (b) across (c) shows a 6-nm high, 40-nm wide ridge. Steps in the underlying SiC substrate are indicated by vertical black bars, 1.1-nm tall. Scan parameters are I_{set} = 5.7 nA and V_{bias} = 72 mV for (a) and I_{set} = 1.0 nA and V_{bias} = 300 mV for (c). (Images (a-c) are reprinted with permission from Ref. [110]. Copyright 2009 by APS.)

7.5.5 Moiré superlattices on FLG

Moiré superlattices were observed on 4H-SiC(000$\bar{1}$) FLG samples grown at 1500 °C and 1550 °C. Interestingly, no moiré superlattices were observed on samples grown at either 1475 °C or 1600 °C. An example of a moiré region is provided in Fig. 7.8(b) (growth temperature of 1500 °C). These superlattices were confined to regions adjacent to ridges; the superlattices were found either on one or both sides of the ridge. It was often observed that the FLG regions adjacent to the ridges were no longer flat, but exhibited a pronounced curvature that persisted over $\sim 0.5\,\mu$m distance from the ridge. Superlattices were never found as isolated islands surrounded entirely by a flat FLG region. By randomly sampling well-separated regions of the FLG surface, Moiré regions with different superlattice periodicities were found at different positions across the same FLG sample. These results are summarized in Table C.1, which indicates that periodicities of the superlattices from three FLG samples range between 4 and 13 nm.

Table 7.2. Samples with moiré superlattice regions and their measured periodicity

Sample	Growth Temp. (°C)	$\mathscr{D}$ (nm)	Θ (degrees)
971	1500	5.6 ± 0.3	2.5 ± 0.1
971	1500	4.2 ± 0.2	3.3 ± 0.1
		4.7 ± 0.3	3.0 ± 0.2
		9.4 ± 2.2	1.5 ± 0.3
		12.7 ± 2.1	1.1 ± 0.2
927	1550	6.4 ± 0.7	2.2 ± 0.3
		7.2 ± 0.5	2.0 ± 0.2
		9.0 ± 0.6	1.6 ± 0.1

7.5.6 Atomic resolution within a moiré superlattice

Atomic-resolution STM images of a moiré superlattice are given in Fig. 7.9(a,c). Distinct regions of apparently different heights are clearly visible as dark, dim, and bright areas. As a guide to the eye, two lines are drawn on top of the STM image; the dashed line follows the superlattice bright areas while the solid line follows the atomic lattice of the carnon atoms.

By resolving the atomic positions in the FLG layer, two independent ways of determining the relative rotation angle of the top graphene layer with respect to the underlying layers become possible. First, using the measured periodicity of the superlattice from the 2D-FFT (4.44 ± 0.31 nm in Fig. 7.9(b)), the angle $\phi = 28.4 \pm 0.2^o$ can be calculated from Eqns. 7.1 and 7.2. Second, the angle can be measured directly from the atomically resolved STM image in Fig. 7.9(a), giving a value of $\phi = 26 \pm 2^o$. These two results are in good agreement with each other. As indicated by the fiducial lines in Figs. 7.9(b,d)), the same relative rotation, ϕ, observed in Fig. 7.9(a)) is seen between the Fourier components in the superlattice scale and atomic scale 2D-FFTs.

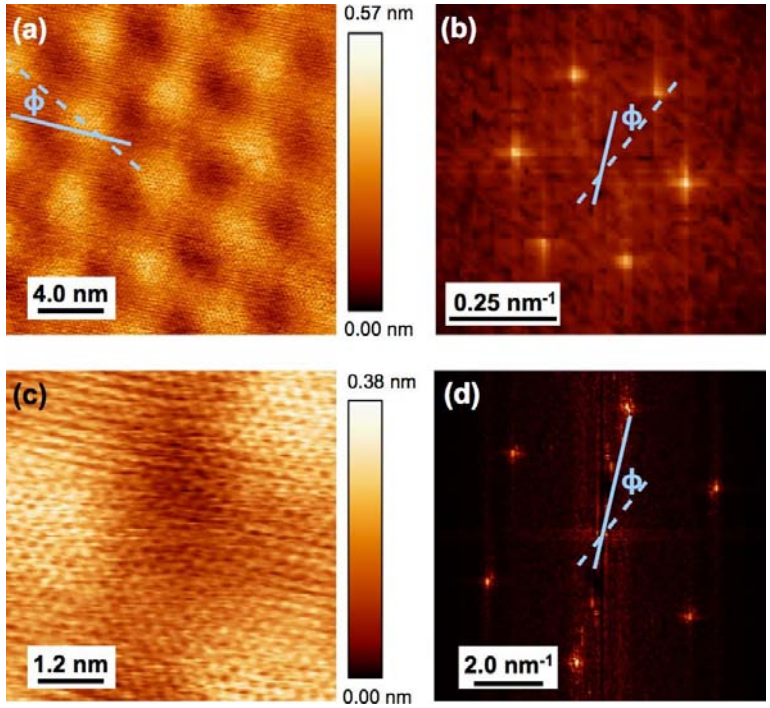

Figure 7.9. (a) An STM image of a 20×20 nm^2 region shows a moiré superlattice. The 2D-FFT of the moiré superlattice (b) shows the hexagonal superlattice ($D = 4.44 \pm 0.31$ nm). Image (b) is a 2D-FFT of a 60×60 nm^2 region; the larger image is necessary for a high-resultion FFT. (c) A 6×6 nm^2 zoom of (a) shows the hexagonal lattice of the top graphene layer. (d) From the 2D-FFT of (a), the atomic lattice is found to be 0.23 ± 0.09 nm, close to the accepted value of 0.246 nm. The scale bars in (b) and (d) are the length of the k-vector where $1/k$ is the lattice periodicity. Scan parameters are I_{set} = 5.7 nA and V_{bias} = 72 mV. (Reprinted with permission from Ref. [110]. Copyright 2009 by APS.)

7.5.7 I(V) across a moiré region

Since the moiré superlattice is an DOS effect, the tunnel current in the moiré region should reflect the variation in the DOS. Campanera *et al.* calculate that the DOS of AA-stacked graphite (bright areas) is 0.0082 states/eV atom, while the DOS of BA-stacked graphite (dark areas) is 0.0040 states/eV atom [143]. This variation in DOS should influence the I(V) data at low bias voltages, at which the tunnel current is roughly proportional to the substrate DOS.

In order to measure the DOS across the moiré patterns, a 3D-mode STM experiment was performed on the FLG sample 976 grown at 1500°C. First, an atomically flat moiré region was scanned in constant-height mode [Fig. 7.10(a)]. In this scan, the bright features (indicated by blue triangles) correspond to a larger measured tunnel current, while the dark features (indicated by red

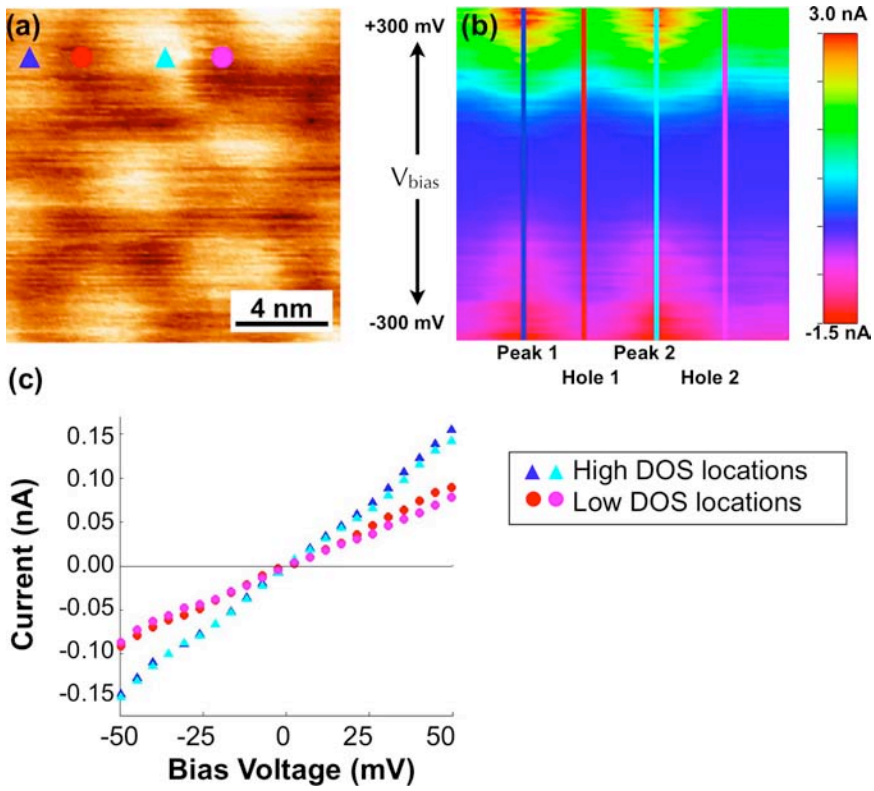

Figure 7.10. (a) A constant-height STM scan of a 14.5 × 14.5 nm^2 region with a moiré superlattice having a periodicity of 4.8 ± 0.3 nm (V_{bias} = 300 mV). In (b), a 3D-mode STM scan of the same superlattice region. The y-axis varies linearly from +300 mV bias to -300 mV bias. The x-axis is 15 nm. The four vertical lines represent the location of the I(V) curves plotted in (c). In the low-bias (±50 mV) range, the I(V)s obtained from the 3D-mode STM scan in (b) are linear.

circles) correspond to a smaller measured tunnel current. In this 3D-mode STM experiment the fast scan direction ($\hat{x}$) is the position of the STM tip and the slow scan direction ($\hat{y}$) is the bias voltage applied to the sample. As is the case for constant-height STM scans and I(V) curves, the feedback is disabled and the instantaneous tunnel current recorded. In Fig. **??**, the measured tunnel current is plotted as a function of tip position and sample bias.

The conductivity, G, is calculated as the slope of the $I(V)$ curve [Fig. **??**]. For the high DOS (bright) regions of the moiré pattern, G_{high} = 2.9 nS; for the low DOS (dark) regions of the moiré pattern, G_{low}= 1.7 nS. The ratio of the conductivities, $G_{high}/G_{low} = 1.7$ is consistent with the theoretical ratio of 2.0 calculated by Campanera *et al.* [143].

7.5.8 A moiré superlattice across a SiC step edge with constant periodicity

The long lateral range over which the moiré superlattices were observed permits an exquisitely sensitive way to map carbon atomic positions across localized defects such as a step edge in the underlying SiC substrate. One such example is illustrated in Fig 7.11(a) which is an image from the FLG sample 2 grown at 1500°C. In Fig. 7.11(b), the superlattice is observed to persist across a 1.1 nm step edge associated with the SiC substrate.

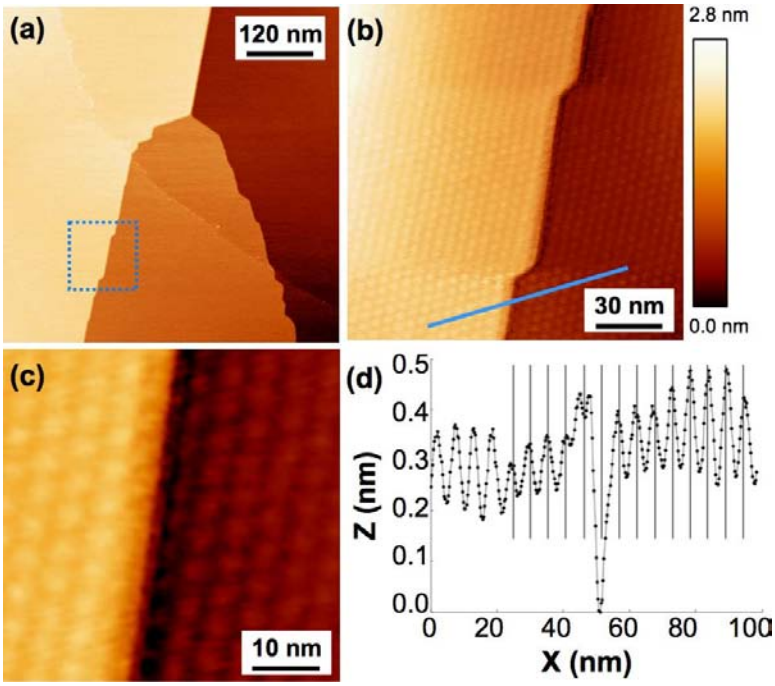

Figure 7.11. (a) An STM image of a 600 × 600 nm^2 region shows a moiré superlattice continuing across two step edges (both 1.1 nm high) in the SiC substrate. The dashed box in (a) indicates the 150 × 150 nm^2 region in (b), which was scanned at a higher resolution. The superlattice is clearly visible in (c), a 50 × 50 nm^2 magnified region of the center of (b). A profile (d) drawn across the step edge in (b) illustrates that no apparent row of atoms is missing at the step edge. To enhance the apparent periodicity, the height of the step edge was subtracted from this profile. Scan parameters are I_{set} = 1.0 nA and V_{bias} = 300 mV for (a) and I_{set} = 1.5 nA and V_{bias} = 50 mV for (b) and (c). (Reprinted with permission from Ref. [110]. Copyright 2009 by APS.)

The measured periodicity of the superlattice in Fig 7.11(b) was determined to be $\mathscr{D} = 4.7 \pm 0.3$ nm. In Fig 7.11(d), the phase of the superlattice is tracked across the step edge. This topography profile illustrates that the superlattice exhibits a constant value of $\mathscr{D}$ and remains in phase as it

traverses the step edge, indicating that the relative rotation between the top two layers of graphene is constant across the step. The observation of a commensurate moiré superlattice spanning a step edge in the substrate supports the suggestion that FLG growth follows a carpet-like growth mechanism proposed by Seyller *et al.* [154].

7.5.9 Termination and energetics of a small moiré region

Typically, the moiré regions in the FLG grown samples studied were large enough that the entire pattern could not be imaged within a single scan of dimension $1 \times 1\,\mu\text{m}^2$. While larger STM scans are possible, the decreased lateral resolution obscures the moiré superlattice (*cf.* Fig. 7.11(a,b)). An unusually small moiré region that could be imaged in a single STM scan was found on sample 2, which was grown at 1500 °C. This superlattice is characterized by a periodicity $\mathscr{D} = 12.7 \pm 2.1$ nm and spans an area of 2.3×10^5 nm^2. As shown in Fig. 7.12(a), this moiré region is bordered by two tall ridges (8–10 nm high) located on the right and bottom of the image.

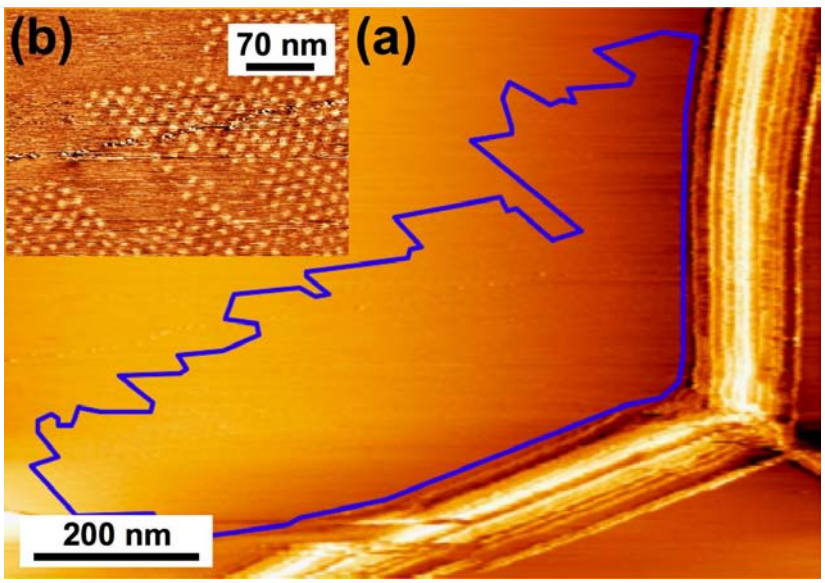

Figure 7.12. (a) An STM image (1000×700 nm^2) shows the extent of the moiré region with a periodicity of $\mathscr{D} = 12.7 \pm 2.1$ nm, as indicated by the solid line. The exceptionally jagged edge of the moiré region is illustrated by the 350×250 nm^2 inset. Scan parameters are I_{set} = 1.0 nA and V_{bias} = 300 mV for (a) and I_{set} = 2.0 nA and V_{bias} = 100 mV for (b). (Reprinted with permission from Ref. [110]. Copyright 2009 by APS.)

While the boundaries between moiré regions and Bernal stacked (**BAB**) graphene are rarely straight, the boundary of this superlattice is unique for the number of jagged protrusions it reveals (see Fig. 7.12(b)). The ragged termination of the superlattice suggests that the relative rotation

between the top two layers of graphene is relaxed by local defects in one of the two layers. The origin of the superlattice is likely high strain fields produced during ridge formation. Evidently the graphene lattice relaxes away from the ridge, causing the superlattice to disappear. The moiré periodicity remains constant up to the superlattice boundary, indicating that the graphene lattice does not appear to be stretched or otherwise distorted.

The minimum relative formation energy of a moiré superlattice is calculated to be 2.5 meV/atom [143]. At the 1500 °C growth temperature, the thermal energy per atom confined to 2D, $k_B T$, is 0.15 eV, where k_B is the Boltzmann constant. At this growth temperature, there is more than sufficient thermal energy to anneal this rotational defect, if the rotation occurs at 1500 °C. This suggests the rotational defect is pinned by an energy barrier that requires significantly more than thermal energy before the rotational defect is relaxed. If the rotation occurs while the FLG sample is cooling, there may not be sufficient thermal energy to anneal the defect. Since the moiré regions are predominately found near ridges, it seems likely that the formation of a ridge causes a rotation of a few graphene layers, resulting in a moiré superlattice that is both created and pinned by the upward lift of individual graphene layers during the ridge formation.

7.5.10 Moiré superlattices coexistent with wave-like features

Wave-like features or ripples with a height of about 1 nm have been reported in TEM images of suspended exfoliated graphene sheets [155] as well as in STM studies of graphene [156, 157]. The existence of ripples have implications for charge transport, since curved regions of graphene are expected to modify the local density of electron states due to a potential that develops that is proportional to the square of the local mean curvature [158, 159, 160]. The precise origin of these ripples, with a focus on the structural integrity of a 2D graphene membrane, has been extensively discussed [161, 162, 163, 164, 92, 165, 166].

We find evidence for rippling in FLG grown on SiC as shown in Fig. 7.13(a), on sample 3, grown at 1550 °C. The ripple-like features emanate from a 1-nm high line defect and are aligned roughly perpendicular to this line defect. The ripples are approximately parallel to each other with a height of 0.1 to 0.2 nm and an apparent width of 20–50 nm (see Fig. 7.13(b,d)). The ripples continue across a 0.65 nm step edge in the substrate. While usually found on flatter regions of FLG, a moiré superlattice has also been observed on this rippled region. A superlattice with an area of ~ 500 nm $\times$ 1000 nm floods the surface spanning the ripples. This superlattice is not disrupted by the ripples in the FLG surface.

Careful analysis of the FFT from Fig. 7.13(a) shows that the superlattice is actually a superposition of two moiré superlattices, implying that at least the top two, if not more, graphene layers are rotated with respect to each other. The relevant FFT is given in Fig. 7.13(c) and shows one periodicity with $\mathscr{D} = 9.3$ nm and $\Theta = 1.5^o$ (highlighted by white circles in Fig. 7.13(c)), corresponding to the bright, inner hexagonal pattern in the FFT. A second moiré superlattice (highlighted by white ellipses in Fig. 7.13(c)) is characterized by FFT spots that are dimmed and blurred slightly, but still clearly resolved. The periodicity and rotation of this second superlattice are measured to be $\mathscr{D}$ = 6.4 nm and Θ = 2.2^o.

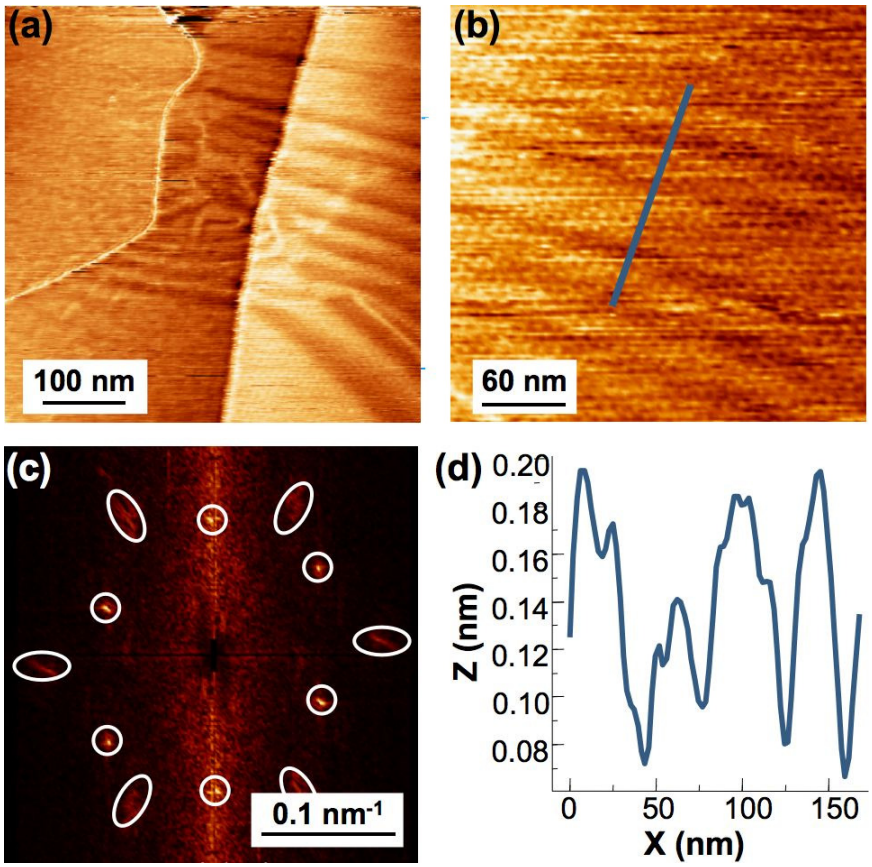

Figure 7.13. (a) An STM image, 500 × 500 nm^2, shows a 1 nm high line defect that runs parallel for ∼200 nm of its length to a 0.65 nm step edge. Carbon ripples emanate from the line defect and are found to cross over the step edge. In (b), an STM image of a 300 × 300 nm^2 zoom of the rippled region of (a) reveals that a superlattice is coexistent with the ripples. In (c), the hexagonal periodicity of the superlattice is confirmed by a 2D-FFT of (b). The superlattice is a superposition of two moiré patterns, with periodicities of $\mathscr{D} = 9.3 \pm 1.2$ nm (bright inner spots) and $\mathscr{D} = 6.4 \pm 0.7$ nm (dim outer spots). In (d), a profile of the ripples along the blue line in (b). Scan parameters are I_{set} = 1.0 nA and V_{bias} = 500 mV. (Reprinted with permission from Ref. [110]. Copyright 2009 by APS.)

7.6 Implications for epitaxial graphene growth on SiC

Taken together, the results of the STM studies presented above are consistent with a non-uniform and heterogenous environment for the growth of FLG on 4H-SiC(000$\bar{1}$) substrates. *A priori*, there are many reasons why a spontaneous and unseeded growth of a truly uniform, perfectly periodic FLG layer over an area larger than a few square micrometers of a 4H-SiC(000$\bar{1}$) substrate might be difficult to achieve. First, the basal plane lattice constant of graphene is $\sim$30% smaller than SiC. As a consequence, in one layer of SiC, there are 12.2 C atoms/nm^2. To form one layer of graphene, 38.2 C atoms/nm^2 are required. Therefore, to free enough C atoms to form a continuous layer of graphene requires the sublimation of more than three layers of SiC [142, 136]. Second, it is reasonable to expect that graphene growth nucleates at many sites across the SiC wafer. Lastly, there is a mismatch in thermal expansion between graphite and SiC. Our STM data provides evidence which suggests that all these issues hinder uniform graphene growth.

It is likely the growth of FLG nucleates at step edges or terrace defects on SiC. Our studies show that at growth temperatures of 1475 °C, any localized patches of FLG that form on the C-face of SiC have already merged to completely cover the SiC substrate. The observation of rough graphene in FLG could reflect a deficit in the supply of C atoms required to form a continuous layer of graphene. Owing to its random nature, sublimation is an uncontrollable process on the atomic scale that inherently roughens the substrate surface. Since the sublimation of more than three layers of SiC are required to free sufficient carbon to form one continuous graphene layer, it is likely that for the thinnest layers of FLG, the underlying roughness created by the uneven evaporation of the SiC substrate seeds the rough graphene growth. Compounding this stoichiometric issue is the reported rapid oxidation rate of the C-face [167]. Oxidation of the SiC surface might also significantly contribute to the roughening of the first few layers of graphene. XPS data show the presence of SiO_2 decreases as the growth temperature increases from 1475 °C to 1550 °C.

The presence of grain boundaries between advancing graphene layers might be anticipated if graphene growth is heterogeneously seeded across the SiC substrate. Indeed, we find evidence in the top FLG layer of 1D boundaries separating two graphene regions (see Fig. 7.7). The presence of these boundaries suggests that graphene sheets, seeded at different nucleation sites across the SiC substrate, do not always uniformly merge into one continuous graphene layer. An alternative explanation for the 1D boundaries is the formation of pentagonal/heptagonal defects during graphene growth, causing local buckling of the FLG.

As the growth temperature increases, we observe a transition between rough graphene layers (seen regularly at 1475 °C) to uniform, atomically smooth FLG having an atomic periodicity identical to HOPG (seen regularly at 1550 °C). The increase in temperature increases the rate of Si sublimation, which occurs most rapidly at step edges, thereby providing more free carbon atoms. The higher growth temperature also increases the surface carbon atom mobility. As a consequence, at higher temperatures, thicker graphene films form with carbon atoms more readily forming sp^2 bonds, thus mitigating the surface roughness inherent at the SiC-graphene interface. Both the greater number of available carbon atoms and the increase in mobility contribute to the atomic smoothing of the graphene film.

As smooth FLG forms, our STM studies suggest that both 1D ridges and moiré superlattices develop. It is likely the ridges form due to the difference in thermal contraction between the basal plane of graphite and the SiC substrate [151]. The exact location of a ridge could be seeded by lines of defects in the FLG layer. Based on I(V) data, we have evidence that the 1D ridges (see Fig. 7.8) are as conducting as the surrounding flatter regions, suggesting that the ridges are graphitic. The height of the ridges is found to increase with the graphene layer thickness. Two ridges often intersect at a point, forming a subtended angle near 120°.

While ridges frequently traverse 1–2 nm high step edges at random angles, the ridges can also be aligned along step edges in the SiC substrate, such as the ridge parallel to the 4.5-nm step edge seen in Fig. 7.8(a). The co-location of a ridge perfectly aligned along a step edge suggests the graphene layers located at step edges contain a number of atomic-scale defects which seed buckling under the compressive stress of cooling.

The formation of ridges in turn cause a rotation in the top layer(s) of the FLG, resulting in a moiré superlattice. We estimate that moiré regions are found near ridges in about 20 percent of our images. Moiré regions are never found as isolated regions surrounded by flat graphene layers. Moiré regions are common on FLG samples grown at 1500 °C, rare on 1550 °C samples, and never found on 1600 °C samples. The ridges, next to which the moiré regions are usually found, have high aspect ratios at 1500 °C, but are smoother and more rounded at 1600 °C. These observations suggest that high stresses in the graphene layer, which are proportional to the aspect ratio of the ridges, can produce localized rotation of graphene layers.

It is possible that the moiré superlattices form when two disparate growth regions of graphene layers merge and overlap. If this is the explanation for the 2D moiré superlattices, then the likelihood of finding a moiré region would be roughly the same as the number density of graphene seed regions. However, we find that the moiré regions are the exception, not the norm, suggesting that they are produced by a relatively rare set of circumstances.

It is possible that the moiré superlattice form when graphene growth encounters a SiC step edge. If, for example, the graphene growing on the top terrace has a different rotation from that growing on the lower terrace, then the growth of an overlayer across a step edge could cause a moiré superlattice to form. However, graphene growth near many of the step edges in FLG exhibits a standard Bernal stacking, with no evidence for a moiré superlattice. Also, it is possible to find examples (see Fig. 7.11) that indicate graphene growth must be commensurate *across* both upper and lower terraces to account for the same periodicity and orientation of the moiré superlattice on both sides of a step edge. These observations all argue against overlayer growth as a possible cause of the moiré superlattices.

It is also possible that atomic-scale defects in the graphene layers, such as the formation of pentagonal-heptagonal defects, nucleate a moiré superlattice. It is well established that a pentagonal-heptagonal defect produces a localized upward puckering of the graphene layer, accompanied by a rotation of the graphene lattice. As a result, the graphene lattice would be highly rotated near the pentagonal-heptagonal defect and would relax to an undeformed lattice as a function of distance from the defect. The resulting moiré superlattice formed by the growth of a pristine graphene layer over such a pentagonal-heptagonal defect would have a radially varying periodicity, similar to that

around a screw dislocation. The moiré superlattices found in our STM study all have a constant periodicity across their entire area, eliminating the possibility that they are formed by localized pentagonal-heptagonal defects.

Since there is sufficient thermal energy at the growth temperature to anneal any moiré superlattices that might develop during growth, we believe that the 2D moiré superlattices in FLG must be produced during the formation of ridges upon cooling. The ridge formation evidently causes a relative rotation between different graphene layers.

7.7 Conclusions

Studies to characterize few layer graphene (FLG) formed on 4H-SiC(000$\bar{1}$) substrates have been summarized. FLG grown at temperatures ranging between 1475 °C and 1600 °C have been investigated. In our study, we confined our attention to FLG that was grown during a ten-minute time interval at the specified growth temperature.

Both X-ray photoelectron spectroscopy (XPS) and scanning tunneling microscopy (STM) were used to characterize the quality of the FLG surface. The XPS studies were useful in confirming the graphitic composition and estimating the thickness of the FLG layers. STM studies revealed a wide variety of different nanometer-scale features on the FLG surface which include rough graphene, atomically smooth graphene, 1D grain boundaries, 1D ridges, and 2D moiré superlattices.

Our efforts to understand the origin of these varied features provide considerable insights into the relevant growth mechanisms of FLG on 4H-SiC(000$\bar{1}$) substrates. In general, our data are qualitatively consistent with a carpet-like growth mechanism of FLG, in which select nano-facets on SiC step edges rapidly produce excess C atoms which diffuse across the substrate to form graphene layers. Upon cooling, the graphene layers are subject to a compressive thermal stress which causes the FLG to fold and buckle along lines of defects that are weak points in the graphene layers. This buckling produces ripples and ridges which induce local strain fields that occasionally cause a rotation of the graphene layers, forming 2D moiré superlattices. The additional periodicity imposed on the electron states in FLG supporting a superlattice will create many narrow minibands separated by small energy minigaps. The creation of these minibands has important implications, especially with regard to increased electron scattering and optical absorption in superlattice regions of FLG.

Chapter 8

Contributions and suggestions for future study

This SAND report presents two avenues of research into nanoscale materials. First, the vibrational spectra of MWNTs and Ag_2Ga nanoneedles were measured using electrostatic excitation and laser Doppler vibrometry. Second, scanning tunneling microscopy scans of graphene provided insights into the nature of epitaxial graphene growth on the C-face of SiC.

The specific contributions of this work are:

1. A demonstration that laser Doppler vibrometery is a practical, non-destructive means to measure the thermal vibration spectra of nanowires.

   (a) The thermal vibration spectra of five MWNTs and eight Ag_2Ga nanoneedles were measured and analyzed.

   (b) From these vibration spectra and the dimensions of the nanowires, the elastic modulus of the nanowires and quality factor of oscillation were calculated. PECVD-grown MWNTs were found to have an elastic modulus, $E = 37 \pm 26$ GPa, well within the range of E previously reported for MWNTs. The E of Ag_2Ga nanoneedles is 84.3 ± 1.0 GPa. For both nanowires, Q at atmospheric pressure was dominated by gas damping.

   (c) The operating deflection shape of acoustically-excited Ag_2Ga nanoneedles was used to confirm the identification of the eigenmodes.

2. Estimates for the smallest diameter nanowires whose vibrational spectra can be measured in this way were calculated using Mie scattering theory. A method of adding reflective glass beads to nanowires to increase their optical scattering was developed.

3. Theoretical approximations sensitivity of cantilevers used as mass sensors were presented. These approximations suggest that short, low mass cantilevers with high E are best suited for mass sensing applications.

4. Scanning tunneling microscopy scans confirmed the presence of few-layer graphene on C-face epitaxial graphene samples grown at temperatures of 1475° and higher.

5. Moiré superlattices were found *only* near ridges, indicating that the ridge formation can cause mis-rotations of the FLG layer(s). These ridges form as the epitaxial graphene cools due to the thermal contraction of the SiC substrate.

6. The paucity of the moiré superlattices, which were found near only $\sim$20 percent of the ridges, indicates that Bernal stacking of FLG is highly energetically favorable.

7. I(V) measurements of the moiré superlattices showed that the high DOS regions had a conductivity 1.7 times greater than that of the low DOS regions.

Both projects offer many possibilities for future research. A few possibilities are:

1. Further research is needed to understand the vibration spectra of optically forced nanoneedles. For optical forcing studies, a variable density filter should be placed in the optical path of the LDV. Rotating the filter would decrease the power of the transmitted laser beam. At lower laser powers, the optical forcing should be minimal.

2. With such a variable density filter in place, the vibrational spectra of nanoneedles in vacuum could be measured without significant optical forcing effects. Measurements of the quality factor of nanoneedles in low vacuum ($\sim$10 Torr) would provide good estimates for the intrinsic quality factor of Ag_2Ga nanoneedles.

3. Recent papers by Seyller *et al.* and Hannon and Tromp [108, 107] illustrate the importance of slowing the rate of Si sublimation to improve the quality of graphene grown on the Si-face of SiC. The epitaxial graphene presented in this thesis was grown in a slight over-pressure of Si. I am interested in the results of growing C-face graphene in an overpressure of argon. I expect the growth rate to be retarded, which might allow for monolayer and bilayer graphene growth.

4. The nature of the SiC reconstruction and the buffer layer which forms is understood for the Si-face, but rarely discussed for the C-face. UHV-STM studies of the fractional-coverage C-face growth at 1450°C could show the atomic arrangements of the atoms in the initial growth patches.

References

[1] P. Poncharal, Z. L. Wang, D. Ugarte, and W. A. de Heer. Electrostatic deflections and electromechanical resonances of carbon nanotubes. *Science*, 283(5407):1513–1516, 1999.

[2] S. T. Purcell, P. Vincent, C. Journet, and V. T. Binh. Tuning of nanotube mechanical resonances by electric field pulling. *Physical Review Letters*, 89(27), 2002.

[3] V. Sazonova, Y. Yaish, H. Ustunel, D. Roundy, T. A. Arias, and P. L. McEuen. A tunable carbon nanotube electromechanical oscillator. *Nature*, 431(7006):284–287, 2004.

[4] B. Witkamp, M. Poot, and H. S. J. van der Zant. Bending-mode vibration of a suspended nanotube resonator. *Nano Letters*, 6(12):2904–2908, 2006.

[5] D. Garcia-Sanchez, A. S. Paulo, M. J. Esplandiu, F. Perez-Murano, L. Forro, A. Aguasca, and A. Bachtold. Mechanical detection of carbon nanotube resonator vibrations. *Physical Review Letters*, 99(8), 2007.

[6] M. F. Yu, G. J. Wagner, R. S. Ruoff, and M. J. Dyer. Realization of parametric resonances in a nanowire mechanical system with nanomanipulation inside a scanning electron microscope. *Physical Review B*, 66(7):073406, 2002.

[7] Z. L. Wang, Z. R. Dai, R. P. Gao, and J. L. Gole. Measuring the Young's modulus of solid nanowires by in situ TEM. *Journal of Electron Microscopy*, 51:S79–S85, 2002.

[8] R. R. He, X. L. Feng, M. L. Roukes, and P. D. Yang. Self-transducing silicon nanowire electromechanical systems at room temperature. *Nano Letters*, 8(6):1756–1761, 2008.

[9] A. A. Michelson and E. W. Morley. On the relative motion of the earth and the luminiferous ether. *American Journal of Science*, 34(203):333–345, 1887.

[10] Wikipedia. LIGO — Wikipedia, the free encyclopedia, 2009. `http://en.wikipedia.org/wiki/LIGO` [Online; accessed 23-March-2009].

[11] N. P. Cooper. An improved heterodyne laser interferometer for use in studies of cochlear mechanics. *Journal of Neuroscience Methods*, 88(1):93–102, 1999.

[12] K. Kokkonen and M. Kaivola. Scanning heterodyne laser interferometer for phase-sensitive absolute-amplitude measurements of surface vibrations. *Applied Physics Letters*, 92(6):063502, 2008.

[13] B. W. Hoogenboom, Pltm Frederix, J. L. Yang, S. Martin, Y. Pellmont, M. Steinacher, S. Zach, E. Langenbach, and H. J. Heimbeck. A Fabry-Perot interferometer for micrometer-sized cantilevers. *Applied Physics Letters*, 86(7):074101, 2005.

[14] J. F. Portoles, P. J. Cumpson, J. Hedley, S. Allen, P. M. Williams, and S. J. B. Tendler. Accurate velocity measurements of AFM-cantilever vibrations by Doppler interferometry. *Journal of Experimental Nanoscience*, 1:51–62, 2006.

[15] J. Ricci and C. Cetinkaya. Air-coupled acoustic method for testing and evaluation of microscale structures. *Review of Scientific Instruments*, 78(5), 2007.

[16] T. Kouh, D. Karabacak, D. H. Kim, and K. L. Ekinci. Diffraction effects in optical interferometric displacement detection in nanoelectromechanical systems. *Applied Physics Letters*, 86(1):013106, 2005.

[17] P. Li and R. Hu. On the air damping of flexible microbeam in free space at the free-molecule regime. *Microfluidics and Nanofluidics*, 3(6):715–721, 2007.

[18] M. Belov, N. J. Quitoriano, S. Sharma, W. K. Hiebert, T. I. Kamins, and S. Evoy. Mechanical resonance of clamped silicon nanowires measured by optical interferometry. *Journal of Applied Physics*, 103(7):074304–7, 2008.

[19] T. Ono, S. Sugimoto, H. Miyashita, and M. Esashi. Mechanical energy dissipation of multiwalled carbon nanotube in ultrahigh vacuum. *Japanese Journal of Applied Physics Part 2-Letters*, 42(6B):L683–L684, 2003.

[20] C. H. Kiang, M. Endo, P. M. Ajayan, G. Dresselhaus, and M. S. Dresselhaus. Size effects in carbon nanotubes. *Physical Review Letters*, 81(9):1869–1872, 1998.

[21] M. Monthioux and V. L. Kuznetsov. Who should be given the credit for the discovery of carbon nanotubes? *Carbon*, 44(9):1621–1623, 2006.

[22] S. Iijima. Helical microtubules of graphitic carbon. *Nature*, 354:56–58, 1991.

[23] M. Meyyappan. *Carbon Nanotubes: Science and Applications*. CRC Press, Washington, D.C., 2005.

[24] S. Amelinckx, X. B. Zhang, D. Bernaerts, X. F. Zhang, V. Ivanov, and J. B. Nagy. A formation mechanism for catalytically grown helix-shaped graphite nanotubes. *Science*, 265(5172):635–639, 1994.

[25] K. M. Lee, B. Lukic, A. Magrez, J. W. Seo, G. A. D. Briggs, A. J. Kulik, and L. Forro. Diameter-dependent elastic modulus supports the metastable-catalyst growth of carbon nanotubes. *Nano Letters*, 7(6):1598–1602, 2007.

[26] J. P. Salvetat, A. J. Kulik, J. M. Bonard, G. A. D. Briggs, T. Stockli, K. Metenier, S. Bonnamy, F. Beguin, N. A. Burnham, and L. Forro. Elastic modulus of ordered and disordered multiwalled carbon nanotubes. *Advanced Materials*, 11(2):161–165, 1999.

[27] P. Harris. *Carbon Nanotubes and Related Structures: New Materials for the Twenty-first Century*. Cambridge University Press, Cambridge, 1999.

[28] A. Loiseau, P. Launois, P. Petit, S. Roche, and J.-P. Salvetat. *Understanding Carbon Nanotubes: From Basics to Applications*, volume 677 of *Lecture Notes in Physics*. Springer, Heidelberg, 2006.

[29] M. F. Yu, B. I. Yakobson, and R. S. Ruoff. Controlled sliding and pullout of nested shells in individual multiwalled carbon nanotubes. *Journal of Physical Chemistry B*, 104(37):8764–8767, 2000.

[30] J. Cumings and A. Zettl. Low-friction nanoscale linear bearing realized from multiwall carbon nanotubes. *Science*, 289(5479):602–604, 2000.

[31] S. I. Lee, S. W. Howell, A. Raman, R. Reifenberger, C. V. Nguyen, and M. Meyyappan. Nonlinear tapping dynamics of multi-walled carbon nanotube tipped atomic force microcantilevers. *Nanotechnology*, 15(5):416–421, 2004.

[32] S. Iijima, C. Brabec, A. Maiti, and J. Bernholc. Structural flexibility of carbon nanotubes. *Journal of Chemical Physics*, 104(5):2089–2092, 1996.

[33] M. M. J. Treacy, T. W. Ebbesen, and J. M. Gibson. Exceptionally high Young's modulus observed for individual carbon nanotubes. *Nature*, 381(6584):678–680, 1996.

[34] J. Gaillard, M. Skove, and A. M. Rao. Mechanical properties of chemical vapor deposition-grown multiwalled carbon nanotubes. *Applied Physics Letters*, 86(23):233109, 2005.

[35] E. W. Wong, P. E. Sheehan, and C. M. Lieber. Nanobeam mechanics: Elasticity, strength, and toughness of nanorods and nanotubes. *Science*, 277(5334):1971–1975, 1997.

[36] G. Guhados, W. K. Wan, X. L. Sun, and J. L. Hutter. Simultaneous measurement of Young's and shear moduli of multiwalled carbon nanotubes using atomic force microscopy. *Journal of Applied Physics*, 101(3), 2007.

[37] M. S. Dresselhaus, G. Dresselhaus, and R. Saito. Physics of carbon nanotubes. *Carbon*, 33(7):883–891, 1995.

[38] R. Saito, G. Dresselhaus, and M. S. Dresselhaus. Electronic-structure of double-layer graphene tubules. *Journal of Applied Physics*, 73(2):494–500, 1993.

[39] Y. K. Kwon and D. Tomanek. Electronic and structural properties of multiwall carbon nanotubes. *Physical Review B*, 58(24):R16001–R16004, 1998.

[40] C. T. White, D. H. Robertson, and J. W. Mintmire. Helical and rotational symmetries of nanoscale graphitic tubules. *Physical Review B*, 47(9):5485–5488, 1993.

[41] T. W. Ebbesen, H. J. Lezec, H. Hiura, J. W. Bennett, H. F. Ghaemi, and T. Thio. Electrical conductivity of individual carbon nanotubes. *Nature*, 382(6586):54–56, 1996.

[42] P. J. de Pablo, E. Graugnard, B. Walsh, R. P. Andres, S. Datta, and R. Reifenberger. A simple, reliable technique for making electrical contact to multiwalled carbon nanotubes. *Applied Physics Letters*, 74(2):323–325, 1999.

[43] P. G. Collins and P. Avouris. Multishell conduction in multiwalled carbon nanotubes. *Applied Physics A-Materials Science & Processing*, 74(3):329–332, 2002.

[44] P. C. Collins, M. S. Arnold, and P. Avouris. Engineering carbon nanotubes and nanotube circuits using electrical breakdown. *Science*, 292(5517):706–709, 2001.

[45] C. Lan. *Electrical Transport Studies of Individual Multiwalled Carbon Nanotubes*. PhD thesis, Purdue University, 2008.

[46] M. M. Yazdanpanah, S. A. Harfenist, A. Safir, and R. W. Cohn. Selective self-assembly at room temperature of individual freestanding Ag2Ga alloy nanoneedles. *Journal of Applied Physics*, 98(7):073510, 2005.

[47] M. M. Yazdanpanah, M. Hosseini, S. Pabba, S. M. Berry, V. V. Dobrokhotov, A. Safir, R. S. Keynton, and R. W. Cohn. Micro-wilhelmy and related liquid property measurements using constant-diameter nanoneedle-tipped atomic force microscope probes. *Langmuir*, 24(23):13753–13764, 2008.

[48] M. Yazdanpanah. *Near Room Temperature Self-Assembly of Nanostructures by Reaction of Gallium with Metal Thin Films*. PhD thesis, University of Louisville, 2006.

[49] V. V. Dobrokhotov, M. M. Yazdanpanah, S. Pabba, A. Safir, and R. W. Cohn. Visual force sensing with flexible nanowire buckling springs. *Nanotechnology*, 19(3), 2008. 035502.

[50] H. J. Butt and M. Jaschke. Calculation of thermal noise in atomic-force microscopy. *Nanotechnology*, 6(1):1–7, 1995.

[51] J. B. Marion and S. T. Thornton. *Classical Dynamics of Particles and Systems*. Saunders College, Fort Worth, 4th edition, 1995.

[52] W. T. Thomson. *Vibration Theory and Applications*. Prentice-Hall, Inc., Englewood Cliffs, N. J., 1965.

[53] B. P. Lathi. *An Introduction to Random Signals and Communication Theory*. International Textbook Company, Scranton, 1968.

[54] P. D. Welch. Use of fast Fourier transform for estimation of power spectra - a method based on time averaging over short modified periodograms. *IEEE Transactions on Audio and Electroacoustics*, AU15(2):70–73, 1967.

[55] L. Landau and E. M. Lifshitz. *Statistical Physics*. Butterworth-Heinemann, Oxford, 3rd edition, 1984.

[56] J. Melcher, S. Q. Hu, and A. Raman. Equivalent point-mass models of continuous atomic force microscope probes. *Applied Physics Letters*, 91(5), 2007.

[57] M. V. Salapaka, H. S. Bergh, J. Lai, A. Majumdar, and E. McFarland. Multi-mode noise analysis of cantilevers for scanning probe microscopy. *Journal of Applied Physics*, 81(6):2480–2487, 1997.

[58] R. B. Bhiladvala and Z. J. Wang. Effect of fluids on the Q factor and resonance frequency of oscillating micrometer and nanometer scale beams. *Physical Review E*, 69(3):036307, 2004.

[59] Wikipedia. Knudsen number — Wikipedia, the free encyclopedia, 2009. `http://en.wikipedia.org/wiki/Knudsen_number` [Online; accessed 30-July-2008].

[60] Wikipedia. Earth's atmosphere — Wikipedia, the free encyclopedia, 2008. `http://en.wikipedia.org/wiki/Earth's_atmosphere` [Online; accessed 30-July-2008].

[61] J. E. Sader, I. Larson, P. Mulvaney, and L. R. White. Method for the calibration of atomic-force microscope cantilevers. *Review of Scientific Instruments*, 66(7):3789–3798, 1995.

[62] E. O. Brigham. *The Fast Fourier Transform and its Applications*. Prentice Hall, Englewood Cliffs, New Jersey, 1988.

[63] P. B. Amama, B. A. Cola, T. D. Sands, X. F. Xu, and T. S. Fisher. Dendrimer-assisted controlled growth of carbon nanotubes for enhanced thermal interface conductance. *Nanotechnology*, 18(38), 2007.

[64] C. Lan, P. B. Amama, T. S. Fisher, and R. G. Reifenberger. Correlating electrical resistance to growth conditions for multiwalled carbon nanotubes. *Applied Physics Letters*, 91(9):093105, 2007.

[65] H. J. Dai, J. H. Hafner, A. G. Rinzler, D. T. Colbert, and R. E. Smalley. Nanotubes as nanoprobes in scanning probe microscopy. *Nature*, 384(6605):147–150, 1996.

[66] R. Stevens, C. Nguyen, A. Cassell, L. Delzeit, M. Meyyappan, and J. Han. Improved fabrication approach for carbon nanotube probe devices. *Applied Physics Letters*, 77(21):3453–3455, 2000.

[67] C. V. Nguyen, C. So, R. Stevens, Y. Li, L. Delziet, P. Sarrazin, and M. Meyyappan. High lateral resolution imaging with sharpened tip of multi-walled carbon nanotube scanning probe. *Journal of Physical Chemistry B*, 108(9):2816–2821, 2004.

[68] C. V. Nguyen, K. J. Chao, R. M. D. Stevens, L. Delzeit, A. Cassell, J. Han, and M. Meyyappan. Carbon nanotube tip probes: stability and lateral resolution in scanning probe microscopy and application to surface science in semiconductors. *Nanotechnology*, 12(3):363–367, 2001.

[69] C. Albonetti, M. Cavallini, M. Massi, J. F. Moulin, and F. Biscarini. Electrochemical fabrication of cobalt and nickel tips for scanning tunneling microscopy. *Journal of Vacuum Science & Technology B*, 23(6):2564–2566, 2005.

[70] Craig F. Bohren and Donald R. Huffman. *Absorption and Scattering of Light by Small Particles*. John Wiley & Sons, New York, 1983.

[71] C. F. Bohren. Scattering of electromagnetic-waves by an optically-active cylinder. *Journal of Colloid and Interface Science*, 66(1):105–109, 1978.

[72] D. L. Greenaway, G. Harbeke, F. Bassani, and E. Tosatti. Anisotropy of optical constants and band structure of graphite. *Physical Review*, 178(3):1340–1348, 1969.

[73] E. D. Palik, editor. *Handbook of Optical Constants of Solids*, volume 1. Elsevier, 1985.

[74] D. E. Aspnes and A. A. Studna. Dielectric functions and optical-parameters of Si, Ge, GaP, GaAs, GaSb, InP, InAs, and InSb from 1.5 to 6.0 eV. *Physical Review B*, 27(2):985–1009, 1983.

[75] L. B. Biedermann, R. C. Tung, A. Raman, and R. G. Reifenberger. Flexural vibration spectra of carbon nanotubes measured using laser Doppler vibrometry. *Nanotechnology*, 20(3):035702, 2009.

[76] A. Ashkin, J. M. Dziedzic, J. E. Bjorkholm, and S. Chu. Observation of a single-beam gradient force optical trap for dielectric particles. *Optics Letters*, 11(5):288–290, 1986.

[77] R. C. Gauthier, M. Ashman, and C. P. Grover. Experimental confirmation of the optical-trapping properties of cylindrical objects. *Applied Optics*, 38(22):4861–4869, 1999.

[78] P. J. Pauzauskie, A. Radenovic, E. Trepagnier, H. Shroff, P. D. Yang, and J. Liphardt. Optical trapping and integration of semiconductor nanowire assemblies in water. *Nature Materials*, 5(2):97–101, 2006.

[79] K. Svoboda and S. M. Block. Optical trapping of metallic Rayleigh particles. *Optics Letters*, 19(13):930–932, 1994.

[80] K. Neuman and S. Block. Optical trapping. *Review of Scientific Instruments*, 75(9):2787, 2007.

[81] L. Bosanac, T. Aabo, P. M. Bendix, and L. B. Oddershede. Efficient optical trapping and visualization of silver nanoparticles. *Nano Letters*, 8(5):1486–1491, 2008.

[82] C. Selhuber-Unkel, I. Zins, O. Schubert, C. Sonnichsen, and L. B. Oddershede. Quantitative optical trapping of single gold nanorods. *Nano Letters*, 8(9):2998–3003, 2008.

[83] P. B. Johnson and R. W. Christy. Optical-constants of noble-metals. *Physical Review B*, 6(12):4370–4379, 1972.

[84] B. Dhayal, N. Post, J. Melcher, A. Raman, G. Chiu, and R. Reifenberger. Enhancing micro-cantilever quality factor by controlling mass distribution. *(in preparation)*, 2009.

[85] R. G. Christian. Theory of oscillating-vane vacuum gauges. *Vacuum*, 16(4):175–178, 1966.

[86] W. E. Newell. Miniaturization of tuning forks. *Science*, 161(3848):1320–1326, 1968.

[87] J. F. Vignola, J. A. Judge, J. Jarzynski, M. Zalalutdinov, B. H. Houston, and J. W. Baldwin. Effect of viscous loss on mechanical resonators designed for mass detection. *Applied Physics Letters*, 88(4):041921, 2006.

[88] T. R. Albrecht, P. Grutter, D. Horne, and D. Rugar. Frequency modulation detection using high-Q cantilevers for enhanced force microscope sensitivity. *Journal of Applied Physics*, 69(2):668–673, 1991.

[89] L. Rodriguez-Pardo, J. Farina, C. Gabrielli, H. Perrot, and R. Brendel. Resolution in quartz crystal oscillator circuits for high sensitivity microbalance sensors in damping media. *Sensors and Actuators B*, 103(1-2):318–324, 2004.

[90] S. W. Howell, 12 May 2009.

[91] K. S. Novoselov, A. K. Geim, S. V. Morozov, D. Jiang, Y. Zhang, S. V. Dubonos, I. V. Grigorieva, and A. A. Firsov. Electric field effect in atomically thin carbon films. *Science*, 306(5696):666–669, 2004.

[92] A. K. Geim and K. S. Novoselov. The rise of graphene. *Nature Materials*, 6(3):183–191, 2007.

[93] A. H. Castro Neto, F. Guinea, N. M. R. Peres, K. S. Novoselov, and A. K. Geim. The electronic properties of graphene. *Reviews of Modern Physics*, 81(1):109–162, 2009.

[94] K. K. Kubista, D. L. Miller, G. M. Rutter, M. Ruan, W. A. de Heer, P. N. First, and J. A. Stroscio. Magnetic oscillations in scanning tunneling spectroscopy of epitaxial graphene on SiC, 18 March 2009.

[95] Y. Q. Wu, P. D. Ye, M. A. Capano, Y. Xuan, Y. Sui, M. Qi, J. A. Cooper, T. Shen, D. Pandey, G. Prakash, and R. Reifenberger. Top-gated graphene field-effect-transistors formed by decomposition of SiC. *Applied Physics Letters*, 92(9):092102, 2008.

[96] A. Reina, X. T. Jia, J. Ho, D. Nezich, H. B. Son, V. Bulovic, M. S. Dresselhaus, and J. Kong. Large area, few-layer graphene films on arbitrary substrates by chemical vapor deposition. *Nano Letters*, 9(1):30–35, 2009.

[97] P. Blake, P. D. Brimicombe, R. R. Nair, T. J. Booth, D. Jiang, F. Schedin, L. A. Ponomarenko, S. V. Morozov, H. F. Gleeson, E. W. Hill, A. K. Geim, and K. S. Novoselov. Graphene-based liquid crystal device. *Nano Letters*, 8(6):1704–1708, 2008.

[98] B. Wang, M. L. Bocquet, S. Marchini, S. Gunther, and J. Wintterlin. Chemical origin of a graphene moire overlayer on Ru(0001). *Physical Chemistry Chemical Physics*, 10(24):3530–3534, 2008.

[99] P. T. B. Shaffer. A review of structure of silicon carbide. *Acta Crystallographica Section B-Structural Crystallography and Crystal Chemistry*, B 25:477–488, 1969.

[100] I. Forbeaux, J. M. Themlin, and J. M. Debever. High-temperature graphitization of the 6H-SiC $(000\bar{1})$ face. *Surface Science*, 442(1):9–18, 1999.

[101] U. Starke, J. Bernhardt, J. Schardt, and K. Heinz. SiC surface reconstruction: Relevancy of atomic structure for growth technology. *Surface Review and Letters*, 6(6):1129–1141, 1999.

[102] A. J. Vanbommel, J. E. Crombeen, and A. Vantooren. LEED and Auger-electron observations of SiC(0001) surface. *Surface Science*, 48(2):463–472, 1975.

[103] I. Forbeaux, J. M. Themlin, A. Charrier, F. Thibaudau, and J. M. Debever. Solid-state graphitization mechanisms of silicon carbide 6H-SiC polar faces. *Applied Surface Science*, 162:406–412, 2000.

[104] C. Berger, Z. M. Song, X. B. Li, X. S. Wu, N. Brown, C. Naud, D. Mayo, T. B. Li, J. Hass, A. N. Marchenkov, E. H. Conrad, P. N. First, and W. A. de Heer. Electronic confinement and coherence in patterned epitaxial graphene. *Science*, 312(5777):1191–1196, 2006.

[105] E. Rollings, G. H. Gweon, S. Y. Zhou, B. S. Mun, J. L. McChesney, B. S. Hussain, A. Fedorov, P. N. First, W. A. de Heer, and A. Lanzara. Synthesis and characterization of atomically thin graphite films on a silicon carbide substrate. *Journal of Physics and Chemistry of Solids*, 67(9-10):2172–2177, 2006.

[106] J. B. Hannon and R. M. Tromp. Pit formation during graphene synthesis on SiC(0001): In situ electron microscopy. *Physical Review B*, 77(24):241404, 2008.

[107] R. M. Tromp and J. B. Hannon. Thermodynamics and kinetics of graphene growth on SiC(0001). *Physical Review Letters*, 102(10):106104, 2009.

[108] K. V. Emtsev, A. Bostwick, K. Horn, J. Jobst, G. L. Kellogg, L. Ley, J. L. McChesney, T. Ohta, S. A. Reshanov, J. Rohrl, E. Rotenberg, A. K. Schmid, D. Waldmann, H. B. Weber, and T. Seyller. Towards wafer-size graphene layers by atmospheric pressure graphitization of silicon carbide. *Nature Materials*, 8(3):203–207, 2009.

[109] F. Varchon, P. Mallet, L. Magaud, and J. Y. Veuillen. Rotational disorder in few-layer graphene films on 6H-SiC(000$\bar{1}$): A scanning tunneling microscopy study. *Physical Review B*, 77(16):165415, 2008.

[110] L. B. Biedermann, M. L. Bolen, M. A. Capano, D. Zemlyanov, and R. G. Reifenberger. Insights into few-layer epitaxial graphene growth on 4H-SiC(000$\bar{1}$) substrates from STM studies. *Phys. Rev. B.*, 79:125411, 2009.

[111] K. S. Novoselov, A. K. Geim, S. V. Morozov, D. Jiang, M. I. Katsnelson, I. V. Grigorieva, S. V. Dubonos, and A. A. Firsov. Two-dimensional gas of massless Dirac fermions in graphene. *Nature*, 438(7065):197–200, 2005.

[112] G. Eda, G. Fanchini, and M. Chhowalla. Large-area ultrathin films of reduced graphene oxide as a transparent and flexible electronic material. *Nature Nanotechnology*, 3(5):270–274, 2008.

[113] A. Cresti, N. Nemec, B. Biel, G. Niebler, F. Triozon, G. Cuniberti, and S. Roche. Charge transport in disordered graphene-based low dimensional materials. *Nano Research*, 1(5):361–394, 2008.

[114] K. Yamashita, M. Saito, and T. Oda. Atomic geometry and stability of mono-, di-, and trivacancies in graphene. *Japanese Journal of Applied Physics Part 1-Regular Papers Brief Communications & Review Papers*, 45(8A):6534–6536, 2006.

[115] P. Simonis, C. Goffaux, P. A. Thiry, L. P. Biro, P. Lambin, and V. Meunier. STM study of a grain boundary in graphite. *Surface Science*, 511(1-3):319–322, 2002.

[116] L. Porte, C. H. Devilleneuve, and M. Phaner. Scanning tunneling microscopy observation of local damages induced on graphite surface by ion-implantation. *Journal of Vacuum Science & Technology B*, 9(2):1064–1067, 1991.

[117] B. K. Annis, D. F. Pedraza, and S. P. Withrow. Topographical changes induced by high-dose carbon-bombardment of graphite. *Journal of Materials Research*, 8(10):2587–2599, 1993.

[118] R. H. Telling, C. P. Ewels, A. A. El-Barbary, and M. I. Heggie. Wigner defects bridge the graphite gap. *Nature Materials*, 2(5):333–337, 2003.

[119] G. M. Rutter, J. N. Crain, N. P. Guisinger, T. Li, P. N. First, and J. A. Stroscio. Scattering and interference in epitaxial graphene. *Science*, 317(5835):219–222, 2007.

[120] N. P. Guisinger, G. M. Rutter, J. N. Crain, C. Heiliger, P. N. First, and J. A. Stroscio. Atomic-scale investigation of graphene formation on 6H-SiC(0001). *Journal of Vacuum Science & Technology A*, 26(4):932–937, 2008.

[121] K. Kojima, T. Suzuki, S. Kuroda, J. Nishio, and K. Arai. Epitaxial growth of high-quality 4H-SiC carbon-face by low-pressure hot-wall chemical vapor deposition. *Japanese Journal of Applied Physics Part 2-Letters*, 42(6B):L637–L639, 2003.

[122] S. R. Snyder, T. Foecke, H. S. White, and W. W. Gerberich. Imaging of stacking-faults in highly oriented pyrolytic-graphite using scanning tunneling microscopy. *Journal of Materials Research*, 7(2):341–344, 1992.

[123] H. Hiura. Generation of circular and hexagonal microholes in a graphite surface. *Journal of Materials Research*, 16(5):1287–1292, 2001.

[124] H. A. Mizes and J. S. Foster. Long-range electronic perturbations caused by defects using scanning tunneling microscopy. *Science*, 244(4904):559–562, 1989.

[125] K. F. Kelly, D. Sarkar, G. D. Hale, S. J. Oldenburg, and N. J. Halas. Threefold electron scattering on graphite observed with C-60-adsorbed STM tips. *Science*, 273(5280):1371–1373, 1996.

[126] J. Cervenka and C. F. J. Flipse. The role of defects on the electronic structure of a graphite surface. *Journal of Physics: Conference Series*, 61:190–194, 2007.

[127] M. Kuwabara, D. R. Clarke, and D. A. Smith. Anomalous superperiodicity in scanning tunneling microscope images of graphite. *Applied Physics Letters*, 56(24):2396–2398, 1990.

[128] Z. Y. Rong and P. Kuiper. Electronic effects in scanning-tunneling-microscopy - moiré pattern on a graphite surface. *Physical Review B*, 48(23):17427–17431, 1993.

[129] W. T. Pong and C. Durkan. A review and outlook for an anomaly of scanning tunnelling microscopy (STM): Superlattices on graphite. *Journal of Physics D-Applied Physics*, 38(21):R329–R355, 2005.

[130] H. Beyer, M. Muller, and T. Schimmel. Monolayers of graphite rotated by a defined angle: hexagonal superstructures by STM. *Applied Physics A-Materials Science & Processing*, 68(2):163–166, 1999.

[131] F. Owman and P. Martensson. The SiC(0001)$6\sqrt{3} \times 6\sqrt{3}$ reconstruction studied with STM and LEED. *Surface Science*, 369(1-3):126–136, 1996.

[132] A. Charrier, A. Coati, T. Argunova, F. Thibaudau, Y. Garreau, R. Pinchaux, I. Forbeaux, J. M. Debever, M. Sauvage-Simkin, and J. M. Themlin. Solid-state decomposition of silicon carbide for growing ultra-thin heteroepitaxial graphite films. *Journal of Applied Physics*, 92(5):2479–2484, 2002.

[133] W. Chen, H. Xu, L. Liu, X. Y. Gao, D. C. Qi, G. W. Peng, S. C. Tan, Y. P. Feng, K. P. Loh, and A. T. S. Wee. Atomic structure of the 6H-SiC(0001) nanomesh. *Surface Science*, 596(1-3):176–186, 2005.

[134] V. W. Brar, Y. Zhang, Y. Yayon, T. Ohta, J. L. McChesney, A. Bostwick, E. Rotenberg, K. Horn, and M. F. Crommie. Scanning tunneling spectroscopy of inhomogeneous electronic structure in monolayer and bilayer graphene on SiC. *Applied Physics Letters*, 91(12):122102, 2007.

[135] C. Riedl, U. Starke, J. Bernhardt, M. Franke, and K. Heinz. Structural properties of the graphene-SiC(0001) interface as a key for the preparation of homogeneous large-terrace graphene surfaces. *Physical Review B*, 76(24), 2007. 245406.

[136] P. Lauffer, K. V. Emtsev, R. Graupner, T. Seyller, L. Ley, S. A. Reshanov, and H. B. Weber. Atomic and electronic structure of few-layer graphene on SiC(0001) studied with scanning tunneling microscopy and spectroscopy. *Physical Review B*, 77(15):155426, 2008.

[137] P. Mallet, F. Varchon, C. Naud, L. Magaud, C. Berger, and J. Y. Veuillen. Electron states of mono- and bilayer graphene on SiC probed by scanning-tunneling microscopy. *Physical Review B*, 76(4):041403, 2007.

[138] T. Angot, M. Portail, I. Forbeaux, and J. M. Layet. Graphitization of the 6H-SiC(0001) surface studied by hreels. *Surface Science*, 502:81–85, 2002.

[139] J. Coraux, A. T. N'Diaye, C. Busse, and T. Michely. Structural coherency of graphene on Ir(111). *Nano Letters*, 8(2):565–570, 2008.

[140] A. N. Obraztsov, E. A. Obraztsova, A. V. Tyurnina, and A. A. Zolotukhin. Chemical vapor deposition of thin graphite films of nanometer thickness. *Carbon*, 45(10):2017–2021, 2007.

[141] M. Sasaki, Y. Yamada, Y. Ogiwara, S. Yagyu, and S. Yamamoto. Moire contrast in the local tunneling barrier height images of monolayer graphite on Pt(111). *Physical Review B*, 61(23):15653–15656, 2000.

[142] J. Hass, F. Varchon, J. E. Millan-Otoya, M. Sprinkle, N. Sharma, W. A. De Heer, C. Berger, P. N. First, L. Magaud, and E. H. Conrad. Why multilayer graphene on 4H-SiC(000$\bar{1}$) behaves like a single sheet of graphene. *Physical Review Letters*, 100(12):125504, 2008.

[143] J. M. Campanera, G. Savini, I. Suarez-Martinez, and M. I. Heggie. Density functional calculations on the intricacies of moire patterns on graphite. *Physical Review B*, 75(23):235449, 2007.

[144] S. Hembacher, F. J. Giessibl, J. Mannhart, and C. F. Quate. Revealing the hidden atom in graphite by low-temperature atomic force microscopy. *Proceedings of the National Academy of Sciences of the United States of America*, 100(22):12539–12542, 2003.

[145] I. Horcas, R. Fernandez, J. M. Gomez-Rodriguez, J. Colchero, J. Gomez-Herrero, and A. M. Baro. WSXM: A software for scanning probe microscopy and a tool for nanotechnology. *Review of Scientific Instruments*, 78(1):013705, 2007.

[146] L. I. Johansson, F. Owman, and P. Martensson. High-resolution core-level study of 6H-SiC(0001). *Physical Review B*, 53(20):13793–13802, 1996.

[147] L. Muehlhoff, W. J. Choyke, M. J. Bozack, and J. T. Yates. Comparative electron spectroscopic studies of surface segregation on SiC(0001) and SiC(000$\bar{1}$). *Journal of Applied Physics*, 60(8):2842–2853, 1986.

[148] D. Briggs and J. Grant. *Surface Analysis by Auger and X-ray Photoelectron Spectroscopy*. IM Publications and SurfaceSpectra Limited, Chichester, UK, 2003.

[149] Charles S. Fadley. *Basic Concepts of X-ray Photoelectron Spectroscopy*, volume 2 of *Electron Spectroscopy: Theory, Techniques, and Applications*. Academic Press Inc., New York, 1978.

[150] National Institute of Standards and MD Technology, Gaithersburg. NIST SRD-82, 2001.

[151] G. Prakash, M. Bolen, M. Capano, R. Reifenberger, and D. Zemlyanov. AFM studies of epitaxial graphene. *(in preparation)*, 2009.

[152] M. Grodzicki, P. Mazur, S. Zuber, G. Urbanik, and A. Ciszewski. Empty core screw dislocations formed on 6H-SiC(0001) during hydrogen etching. *Thin Solid Films*, 516(21):7530–7537, 2008.

[153] C. Gackenheimer, L. Cayon, and R. Reifenberger. Analysis of scanning probe microscope images using wavelets. *Ultramicroscopy*, 106(4-5):389–397, 2006.

[154] T. Seyller, K. V. Emtsev, K. Gao, F. Speck, L. Ley, A. Tadich, L. Broekman, J. D. Riley, R. C. G. Leckey, O. Rader, A. Varykhalov, and A. M. Shikin. Structural and electronic properties of graphite layers grown on SiC(0001). *Surface Science*, 600(18):3906–3911, 2006.

[155] J. C. Meyer, A. K. Geim, M. I. Katsnelson, K. S. Novoselov, T. J. Booth, and S. Roth. The structure of suspended graphene sheets. *Nature*, 446(7131):60–63, 2007.

[156] E. Stolyarova, K. T. Rim, S. M. Ryu, J. Maultzsch, P. Kim, L. E. Brus, T. F. Heinz, M. S. Hybertsen, and G. W. Flynn. High-resolution scanning tunneling microscopy imaging of mesoscopic graphene sheets on an insulating surface. *Proceedings of the National Academy of Sciences of the United States of America*, 104(22):9209–9212, 2007.

[157] M. Ishigami, J. H. Chen, W. G. Cullen, M. S. Fuhrer, and E. D. Williams. Atomic structure of graphene on SiO_2. *Nano Letters*, 7(6):1643–1648, 2007.

[158] F. de Juan, A. Cortijo, and M. A. H. Vozmediano. Charge inhomogeneities due to smooth ripples in graphene sheets. *Physical Review B*, 76(16):165409, 2007.

[159] L. Brey and J. J. Palacios. Exchange-induced charge inhomogeneities in rippled neutral graphene. *Physical Review B*, 77(4):041403, 2008.

[160] F. Guinea, M. I. Katsnelson, and M. A. H. Vozmediano. Midgap states and charge inhomogeneities in corrugated graphene. *Physical Review B*, 77(7):075422, 2008.

[161] N. D. Mermin. Crystalline order in 2 dimensions. *Physical Review*, 176(1):250–254, 1968.

[162] S. V. Morozov, K. S. Novoselov, M. I. Katsnelson, F. Schedin, L. A. Ponomarenko, D. Jiang, and A. K. Geim. Strong suppression of weak localization in graphene. *Physical Review Letters*, 97(1):016801, 2006.

[163] D. D. Quinn, J. P. Wilber, C. B. Clemons, G. W. Young, and A. Buldum. Buckling instabilities in coupled nano-layers. *International Journal of Non-Linear Mechanics*, 42(4):681–689, 2007.

[164] J. P. Wilber, C. B. Clemons, G. W. Young, A. Buldum, and D. D. Quinn. Continuum and atomistic modeling of interacting graphene layers. *Physical Review B*, 75(4), 2007. 045418.

[165] A. Fasolino, J. H. Los, and M. I. Katsnelson. Intrinsic ripples in graphene. *Nature Materials*, 6(11):858–861, 2007.

[166] J. M. Carlsson. Buckle or break. *Nature Materials*, 6(11):801–802, 2007.

[167] A. Golz, G. Horstmann, E. S. vonKamienski, and H. Kurz. Oxidation kinetics of 3C, 4H, and 6H silicon carbide. *Silicon Carbide and Related Materials 1995*, 142:633–636, 1996.

[168] E. I. Altman and R. J. Colton. Determination of the orientation of C-60 adsorbed on Au(111) and Ag(111). *Physical Review B*, 48(24):18244–18249, 1993.

[169] B. Babic, J. Furer, S. Sahoo, S. Farhangfar, and C. Schonenberger. Intrinsic thermal vibrations of suspended doubly clamped single-wall carbon nanotubes. *Nano Letters*, 3(11):1577–1580, 2003.

[170] S. Hembacher, F. J. Giessibl, and J. Mannhart. Force microscopy with light-atom probes. *Science*, 305(5682):380–383, 2004.

[171] G. M. Rutter, J. N. Crain, N. P. Guisinger, P. N. First, and J. A. Stroscio. Structural and electronic properties of bilayer epitaxial graphene. *Journal of Vacuum Science & Technology A*, 26(4):938–943, 2008.

[172] J. E. Sader, J. W. M. Chon, and P. Mulvaney. Calibration of rectangular atomic force microscope cantilevers. *Review of Scientific Instruments*, 70(10):3967–3969, 1999.

[173] J. Therrien, L. Biedermann, C. Lan, and R. Reifenberger. Tunnel gap modulation spectroscopy: a scanning probe high frequency nanoscale oscillator (unpublished), 2006.

[174] Y. Zhang, X. P. Gao, and M. J. Weaver. Scanning tunneling microscopy of C-60 and C-70 on ordered Au(111) and Au(110) - molecular-structure and electron transmission. *Journal of Physical Chemistry*, 96(2):510–513, 1992.

[175] Texas Instruments. Wideband fixed-gain amplifier (Rev. B). Datasheet, Texas Instruments, 20 Jan 2005.

Appendix A

The solution to the Euler-Bernulli beam equation for a cantilevered beam

The transversal vibrations of the MWNT are given by the Euler-Bernoulli equation,

$$\frac{\partial^2 w(x,t)}{\partial t^2} + \frac{EI}{\rho_L}\frac{\partial^4 w(x,t)}{\partial x^4} = 0 \tag{A.1}$$

where E is the elastic modulus, I is the areal moment of inertia, and ρ_L is the density per unit length, calculated by multiplying ρ, the density of the nanowire by its cross-sectional area. The bending deflection of the nanowire, $w(x,t) = \Phi(x)z(t)$ is a function of x, the distance along the length of the nanowire and time, t. The bending deflection can be decomposed into $\Phi(x)$, a function describing the oscillation mode shape, and $z(t)$, the deflection of the free end of the nanowire. Using separation of variables, a solution of the form (A.2) is substituted into (A.1)

$$w(x,t) = \sum_{j=1}^{\infty} C_j \Phi_j(x) e^{\pm i\omega_j t}. \tag{A.2}$$

In the above equation, C_j is the normalization constant and ω_j is the oscillation frequency (in rad/sec). Substituting in the solution (Eq. A.2) yields a homogenous fourth-order linear differential equation,

$$\begin{aligned}
&i^2\omega_j^2\Phi_j(x)e^{\pm i\omega_j t} + \frac{EI}{\rho_L}\left(\frac{d^4\Phi_j(x)}{dx^4}\right)e^{\pm i\omega_j t} = 0 \\
&\frac{d^4\Phi_j(x)}{dx^4} - \frac{\omega_j^2\rho_L}{EI}\Phi_j(x) = 0 \\
&\frac{d^4\Phi_j(x)}{dx^4} - \alpha_j^4\Phi_j(x) = 0, \text{ where } \left(\frac{\alpha_j}{L}\right)^4 = \frac{\omega_j^2\rho_L}{EI} = \frac{\rho_L(2\pi f_j)^2}{EI}.
\end{aligned} \tag{A.3}$$

The general solution to the above differential equation is assumed to be a superposition of trigonometric terms,

$$\Phi_j(x) = A\sin\left(\frac{\alpha_j x}{L}\right) + B\cos\left(\frac{\alpha_j x}{L}\right) + C\sinh\left(\frac{\alpha_j x}{L}\right) + D\cosh\left(\frac{\alpha_j x}{L}\right). \tag{A.4}$$

For a cantilevered rod with one fixed end ($x = 0$) and one free end ($x = L$), the boundary conditions are as follows [50],

$$\begin{aligned}
&\text{(a)}\ \ \Phi_j(0) = 0 && \text{fix the amplitude of the beam to be zero}\\
&\text{(b)}\ \ \frac{d\Phi_j}{dx}(0) = 0 && \text{fix the inclination of the beam to be zero}\\
&\text{(c)}\ \ \frac{d^2\Phi_j}{dx^2}(L) = 0 && \text{fix the torque at the free end of the beam to be zero}\\
&\text{(d)}\ \ \frac{d^3\Phi_j}{dx^3}(L) = 0 && \text{fix the force at the free end of the beam to be zero.}
\end{aligned} \tag{A.5}$$

Applying boundary conditions (a) and (b) yields

$$\begin{aligned}
\Phi_j(0) &= B + D = 0 && \Rightarrow D = -B\\
\Phi_j^{'}(0) &= \alpha_j[A + C] && \Rightarrow C = -A.
\end{aligned} \tag{A.6}$$

Thus the general solution can be rewritten as

$$\Phi_j(x) = A[\sin(\frac{\alpha_j x}{L}) - \sinh(\frac{\alpha_j x}{L})] + B[\cos(\frac{\alpha_j x}{L}) - \cosh(\frac{\alpha_j x}{L})]. \tag{A.7}$$

Applying boundary conditions (c) and (d) to Eq. A.7 yields

$$\begin{aligned}
\frac{1}{\alpha_j^2}\Phi_j^{''}(L) &= -A[\sin(\alpha_j) + \sinh(\alpha_j)] - B[\cos(\alpha_j) + \cosh(\alpha_j)] = 0\\
\frac{1}{\alpha_j^3}\Phi_j^{'''}(L) &= -A[\cos(\alpha_j) + \cosh(\alpha_j)] + B[\sin(\alpha_j) - \sinh(\alpha_j)] = 0
\end{aligned} \tag{A.8}$$

In order for the solution to the linear homogenous differential equations in (A.8) to be non-trivial, the determinate formed by the coefficients A and B must be zero.

$$\begin{vmatrix} \sin(\alpha_j) + \sinh(\alpha_j) & \cos(\alpha_j) + \cosh(\alpha_j) \\ \cos(\alpha_j) + \cosh(\alpha_j) & -\sin(\alpha_j) + \sinh(\alpha_j) \end{vmatrix} = 0$$

$$\begin{aligned}
&[\sin(\alpha_j) + \sinh(\alpha_j)][-\sin(\alpha_j) + \sinh(\alpha_j)] - [\cos(\alpha_j) + \cosh(\alpha_j)]^2 = 0\\
&\sin^2(\alpha_j) + \sinh^2(\alpha_j) - \cos^2(\alpha_j) - 2\cos(\alpha_j)\cosh(\alpha_j)\cosh^2(\alpha_j) = 0\\
&-2 - 2\cos(\alpha_j)\cosh(\alpha_j) = 0\\
&\Rightarrow \cos(\alpha_j)\cosh(\alpha_j) = -1,
\end{aligned} \tag{A.9}$$

(A.10)

Table A.1. Allowed α_j which correspond to the first five oscillation frequencies.

j	1	2	3	4	5
α_j	1.8751	4.6941	7.8548	10.995	14.1372

The resulting transcendental equation is solved numerically; table A.1 gives the solutions corresponding to the first five oscillation frequencies. Solving Eq. A.8 for the coefficients A and B yields

$$A = -\cos(\alpha_j) + \cos(\alpha_j) \text{ and } B = \sin(\alpha_j) + \sinh(\alpha_j). \tag{A.11}$$

The eigenfunctions for the mode shapes can be written as

$$\Phi_j(x) = (\sin\alpha_j + \sinh\alpha_j)[\cos(\frac{\alpha_j x}{L}) - \cosh(\frac{\alpha_j x}{L})] - (\cos\alpha_j + \cosh\alpha_j)[\sin(\frac{\alpha_j x}{L}) - \sinh(\frac{\alpha_j x}{L})]. \tag{A.12}$$

Recalling Eq. A.3, the eigenfrequencies of a cantilevered beam are

$$f_j = \frac{\alpha_j^2}{2\pi L^2}\sqrt{\frac{EI}{\rho_L}}. \tag{A.13}$$

Using the equipartition theorem, Butt and Jaschke showed that the average oscillation amplitude at the end of a cantilevered rod is [50]

$$\langle z_j \rangle = \sqrt{\frac{12 k_c T}{K \alpha_j^4}}. \tag{A.14}$$

The normalization coefficient, C_j, in equation (3.2), is found by dividing the average oscillation amplitude, (A.14), by the amplitude at the end of the beam (A.12),

$$C_j = \frac{\langle z_j \rangle}{\Phi_j(L)}. \tag{A.15}$$

Thus the general solution to the Euler-Bernulli equation is given by

$$w(x,t) = \sum_{j=1}^{\infty} \frac{\langle z_j \rangle}{\Phi_j(L)} \Big\{ (\sin\alpha_j + \sinh\alpha_j)[\cos(\frac{\alpha_j}{L}x) - \cosh(\frac{\alpha_j}{L}x)] \\ -(\cos\alpha_j + \cosh\alpha_j)[\sin(\frac{\alpha_j}{L}x) - \sinh(\frac{\alpha_j}{L}x)] \Big\} e^{\pm i\omega_j t}. \tag{A.16}$$

The above derivation applies for any cantilevered beam, regardless of geometry.

To find the mode shapes and oscillation frequencies for a nanowire, we need the spring constant for a cylindrical object, $k_c = 3EI/L^3$, the areal moment of inertia, I, and the linear mass density, ρ_L. The areal moment of inertia of a solid cylinder is given by

$$\begin{aligned}
I &= \int y^2 dA \\
I &= 4\int dy y^2 \sqrt{R^2 - y^2} \\
I &= \frac{4}{8}[tan^{-1}(\frac{y}{R^2 - y^2})R^4 + y\sqrt{R^2 - y^2}(2y^2 - R^2)]|_0^R \\
I &= \frac{\pi}{4}R^4.
\end{aligned} \tag{A.17}$$

Thus the areal moment of inertia for a MWNT with outer diameter d_o and inner diameter d_i is $I = \frac{\pi}{64}(d_o^4 - d_i^4)$. The linear mass density, ρ_L, can be rewritten in terms of the volumetric density ρ as follows,

$$\begin{aligned}
\rho_L &= \frac{m}{L} \text{ where } m = \rho V = \rho L \pi[(\frac{d_o}{2})^2 - (\frac{d_i}{2})^2] \\
\rho &= \frac{\pi\rho}{4}(d_o^2 - d_i^2).
\end{aligned} \tag{A.18}$$

Substituting ρ and I into Eq. A.13 yields

$$f_j = \frac{\alpha_j^2}{8\pi L^2}\sqrt{\frac{E}{\rho}(d_o^2 + d_i^2)} \tag{A.19}$$

for the oscillation frequency of the MWNTs. While the mode shapes, $\Phi_j(x)$, depend only on the boundary conditions, the general solution, $Z(x,t)$, (Eq. A.16) depends on geometry and material properties, specifically E and ρ. The first three mode-shapes of a 5-μm nanowire are shown in Fig. A.1.

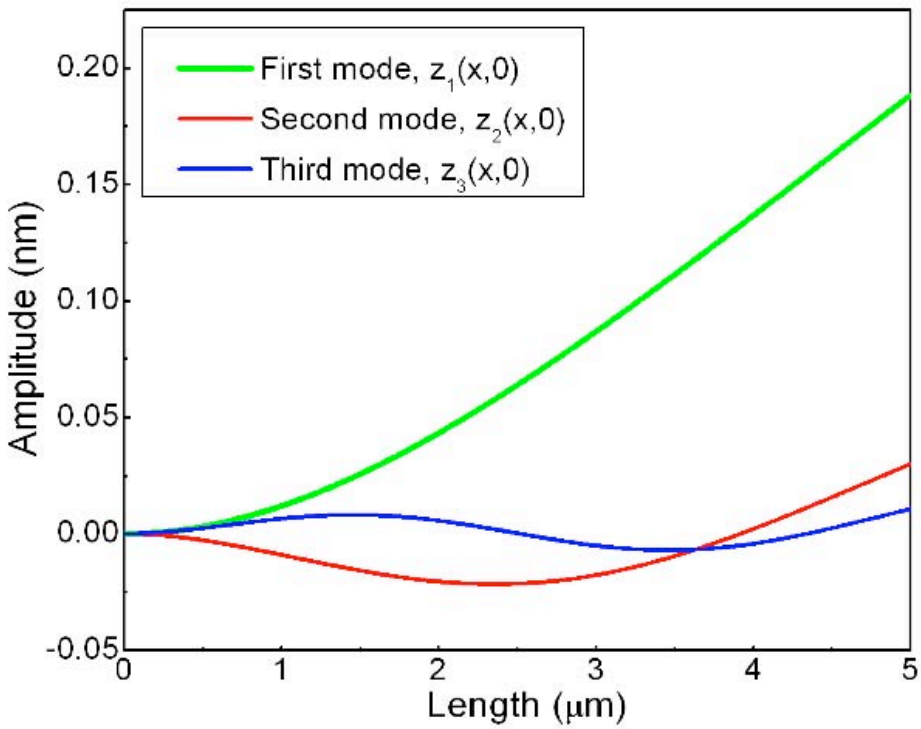

Figure A.1. The first three eigenmodes of a cantilevered nanowire with the following physical properties: E=1 TPa; ρ=2300 kg/m^3; d_o=100 nm; d_i=44 nm, and L = 5 μm.

Appendix B

Tunnel Gap Modulation Spectroscopy

Please note that this section describes the TGMS experiments, as we understood them at the time. Initial literature surveys of the Young's modulus of MWNTs suggested that all MWNTs had $E \sim$ 1 TPa. We now know that the E of CVD and PECVD-grown MWNTs is much lower, 10s-100s of GPa, as is reported in the literature. However, changing the estimated value of E in this appendix would mis-represent the experiments performed.

B.1 Aim of tunnel gap modulation spectroscopy (TGMS)

Since the development of STM in the early 1980s, STMs have been primarily used to examine samples that remain fixed over long periods of time. In certain cases, STMs have been used to study atom diffusion across substrates with atomic resolution. In traditional STM studies, changes in images typically occur at frequencies in the 1 Hz–1 kHz range. However STMs have also been used to monitor the average distance between an STM tip and an oscillating object. For example, STMs have been used to detect cantilever oscillations in AFM experiments.

Tunnel Gap Modulation Spectroscopy (TGMS) is an STM-derived technique that utilizes the exponential dependence of tunnel current to gap distance to measure the frequency of vibrations at the nanoscale. Consider a vibrating object attached to an STM tip that modulates the size of the tunnel gap. The tunnel gap acquires a time-dependence given by

$$z(t) = z_o + A_\perp \sin(2\pi f_1 t), \tag{B.1}$$

where z_o is the tunnel gap maintained by the feedback of the STM (typically 0.4–0.7 nm), $A_\perp$ is the amplitude of the vibrating object in the direction perpendicular to the substrate's surface, and f_1 is the natural frequency of vibration of the object; f_1 can span the MHz to GHz range. The periodic modulation of the tunnel current, $i(t)$ will result in a periodic variation at f_1 given by,

$$i(t) = i_o e^{-2\alpha z(t)}, \tag{B.2}$$

where i_o, the dc tunnel current, is approximately constant and $\alpha \cong 20\ nm^{-1}$ for typical barriers in STM. In what follows, it is important to remember that for this value of α, a change in $z(t)$ by $\sim$0.1 nm produces a factor of $\sim$10 change in $i(t)$. Calculations of the resulting time dependent current (B.2), when Fourier analyzed, exhibit peaks at nf_1, where $n = 1,2,3,4$, etc.

Two possible modes of operation for TGMS are proposed. In the first, a conventional STM tip can be used to measure the oscillation frequency of a rapidly rotating object (such as a C_{60} molecule) [168]. In the second, a vibrating object (such as a MWNT) is attached at an angle to a conducting STM tip that is held above a conducting substrate (Fig. B.1). In both cases, the STM

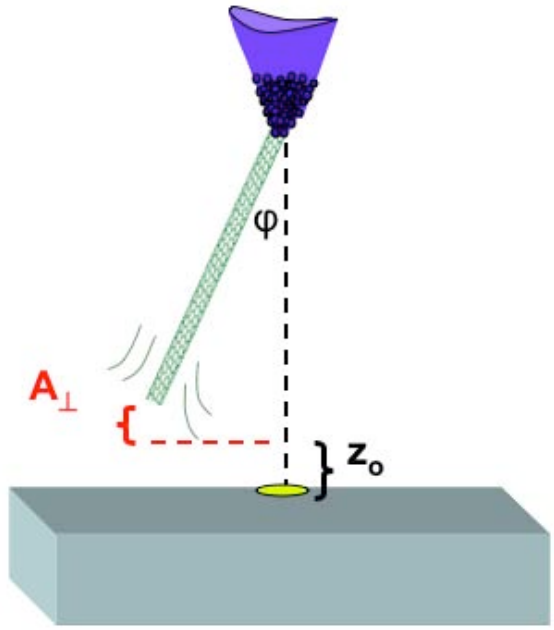

Figure B.1. Schematic of a MWNT attached at angle ϕ to an STM tip (not drawn to scale). The size of the tunnel gap, z_o, is set by the tunnel current set point; $A_\perp$ is the amplitude of the MWNT oscillations.

feedback loop maintains a tunnel gap z_o consistent with a given set point current. In the first case, the rotating C_{60} modulates the size of the tunnel gap; in the second case, the thermally excited vibration of the MWNT modulates the size of the tunnel gap. TGMS offers a means of detecting the oscillations of MWNTs in air. Both thermally-excited [33, 1, 169] and electrically-driven vibrations of carbon nanotubes in vacuum [1, 2, 3] have been previously reported.

Estimated size of the tunnel gap

If a MWNT is attached at an angle ϕ to an STM tip, a tunnel gap of size z_o can be established between the end of the MWNT and a conducting substrate in the usual way. In this case, the substrate is usually inert, freshly cleaved, highly oriented pyrolytic graphite (HOPG). Using TGMS, the resonant frequency of a MWNT mounted on a STM tip can be measured. As derived in Chapter 2, the natural frequency of oscillation of a MWNT of length, L, inner diameter, d_i, and outer

diameter, d_o, is given by [50]

$$f_j = \frac{\alpha_j^2}{8\pi L^2}\sqrt{\frac{E}{\rho}(d_o^2 + d_i^2)}. \tag{B.3}$$

For typical values of L ~3–10 μm, d_o = 100 nm, and d_i = 44 nm, which are estimated from TEM micrographs, Eq. 3.7 predicts frequencies in the 10s of MHz range.

The size of the tunnel gap is proportional to the oscillation amplitude of the MWNT. The average oscillation amplitude at the end of the MWNT is given by [50]

$$\langle z_j \rangle = \sqrt{\frac{12k_BT}{K\alpha_j^4}} = \sqrt{\frac{12k_BT}{\alpha_j^4}\frac{L^3}{3EI}}; \tag{B.4}$$

for MWNTs with the above parameters, $\langle z_1 \rangle$ ranges from 0.18 nm to 1.08 nm, as shown in Fig. B.2. The modulations of the tunnel gap, z, depend on the angle, ϕ, between the MWNT and the normal

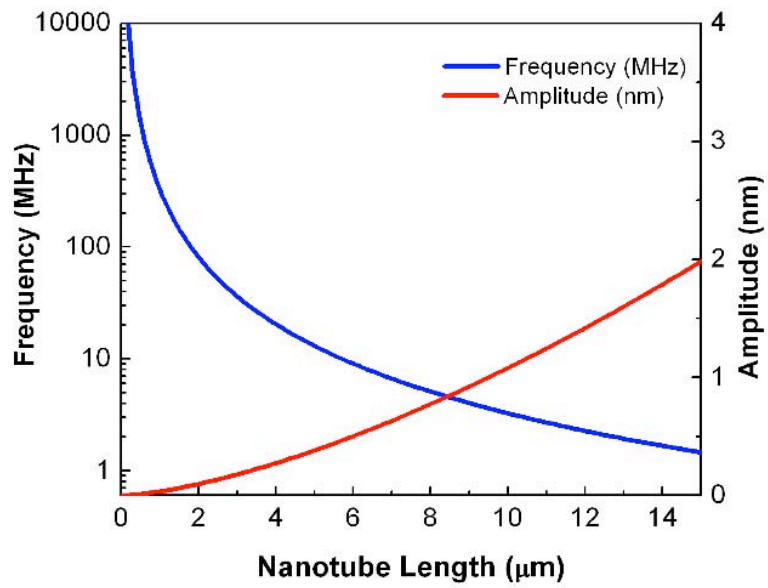

Figure B.2. Calculated fundamental oscillation frequency and amplitude of MWNT as a function of length. The MWNT is assumed to have the following physical properties: E=1 TPa; ρ=2300 kg/m^3; d_o=100 nm; d_i=44 nm. The optimum nanotube lengths for experimental purposes are between 3 and 10 nm. Shorter MWNTs are hard to affix to STM tips and have oscillation frequencies above 40 MHz, the upper limit of our spectrum analyzer; longer MWNTs are likely to snap into contact with the substrate.

to the conducting substrate. From simple geometry we find

$$A_{\perp} = 2\langle z_j \rangle \sin\phi. \tag{B.5}$$

For a 5 μm-long MWNT at ϕ = 30° from the normal, we calculate the that change in the tunnel gap due to the fundamental mode of the oscillating MWNT is 0.19 nm, a value that should easily be detected using TGMS.

While positioning the MWMT at ϕ = 90° from the normal leads to the greatest modulation of the tunnel gap, this configuration is inherently unstable. When parallel to the substrate, the MWNT is likely to snap into contact with the substrate. Conversely, a MWNT held perpendicular to the substrate is in the most stable configuration, yet the modulation of the tunnel gap is infinitesimal. The optimum attachment angle is between 15° and 35° from the normal, as illustrated for a 5-μm MWNT in Fig. B.3.

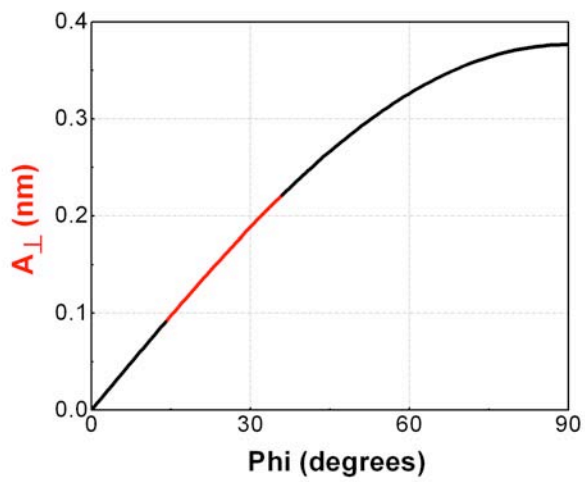

Figure B.3. Modulation of the tunnel gap as a function of attachment angle for a 5 μm-long MWNT. The red portion indicates the range of optimum attachment angles.

B.2 Initial TGMS experiments by J. Therrien

Joel Therrien, a former post-doc in the Reifenberger Nanophysics Lab, developed the concept of TGMS and performed initial experiments demonstrating the viability of the technique. The following experimental procedures are generally applicable to the experiments described in "Results and Discussion" and "Future Work."

For the initial TGMS experiments, a MWNT was carefully mounted to the end of a freshly etched STM tip using nanomanipulators under a darkfield microscope. One nanomanipulator held a cartridge of MWNTs stuck to conducting carbon tape; the other nanomanipulator held a high-aspect ratio tungsten STM tip. Bringing the STM tip in close proximity to a protruding MWNT caused the MWNT to snap into contact with the tip due to van der Waals interaction. A small potential difference, 3-10 V, between the MWNT cartridge and STM tip increased this attraction [66]. Once the MWNT and STM tip were in contact and the MWNT was roughly parallel to the axis of the tip, a voltage pulse of $\sim$20-30 V was applied to break apart the contacted MWNT from the mat of MWNTs on the carbon tape. A bright flash indicative of an electric arc usually occurred when the MWNT broke off of the carbon tape. At this point the MWNT was affixed to the STM tip by the van der Waals force.

The MWNT-tip assembly was then placed in the tip-holder of a modified Nanotec Electrónica^{TM} STM head operating in air, as shown in Fig. B.4. The STM head was placed on top of a two-level vibration isolation system inside a Faraday cage. The input lines between Dulcinea, the STM controller, and the STM head are filtered with commercial low-pass π filters (Spectrum Control case filter 51-311-314). The π filters block nearly all high-frequency noise emanating from Dulcinea; only a 32-MHz clock signal passes through the π filters into the STM pre-amp. The STM is described in detail in Section 3.1.

The thermally-excited oscillations of the MWNT cause a high-frequency oscillation of the tunnel current. These high-frequency signals are shunted around the pre-amp (cut-off frequency $\sim$20 kHz) of the current-to-voltage converter and are amplified by an external rf amplifier with a gain of 20 dB between 100 kHz and 1 GHz. An HP spectrum analyzer Model 3585A was used to analyze the spectral content from the rf amplifier. This spectrum analyzer, while limited to frequencies under 40 MHz, allowed signal averaging over a specified dwell time per channel to further improve the signal to noise ratio (Fig. B.4).

Because of the small signal strength, repeated measurements of the spectral content of the rf amplifier output were performed over a selected frequency range. Each scan was saved and then averaged before any TGMS signal could be identified above the noise floor. For the most robust MWNTs, $\sim$20 separate scans could be reliably obtained, but often the number of scans was limited by inadvertent tip failure [173]. For the following experiments, a MWNT-tip assembly was brought within tunneling range of the substrate and four sweeps of the tunneling current between 0 and 40 MHz were recorded. To obtain the background spectra, the MWNT-tip assembly was withdrawn a few hundred nanometers from the substrate, resulting in a complete loss of the tunnel current. Four sweeps of the background signal between 0 and 40 MHz were then recorded. The four tunnel current scans and background scans were separately averaged; the TGMS current appearing in each tunnel current scan is effectively amplified while random peaks from the noise are cancelled out. Comparisons of the tunnel current and background signal show an identifiable signal at a well-defined frequency. This identifiable signal was believed to be from the modulated tunnel current of the MWNT since this signal was present only when the MWNT was in tunneling range (Fig. B.5).

After measuring the spectral content of the tunneling data, the lengths and outer diameters of many MWNTs were determined by SEM. Approximately 30 MWNT samples were investigated.

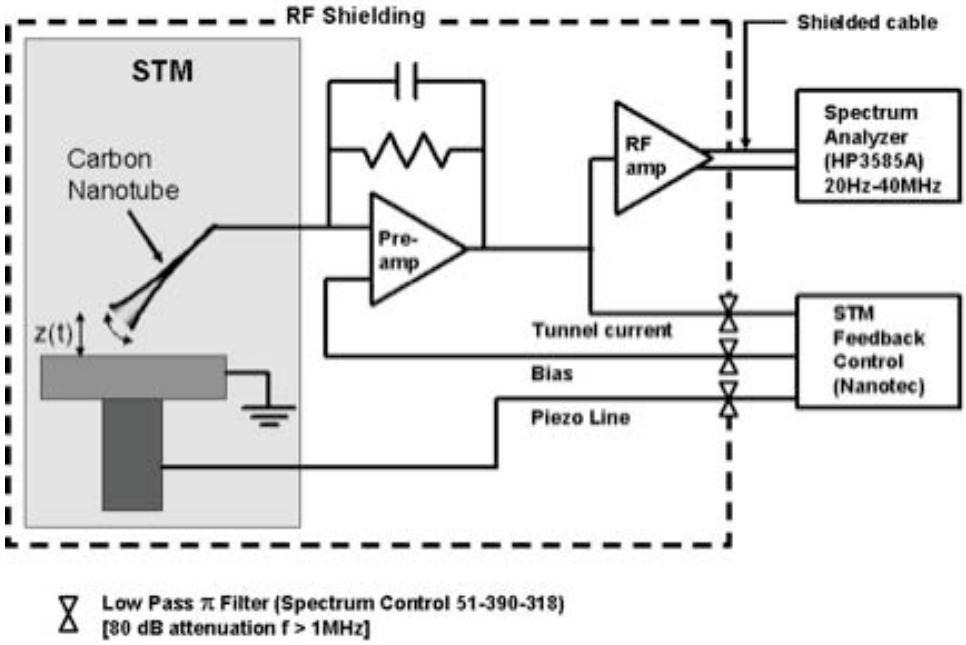

Figure B.4. A block diagram of the experimental setup showing the low frequency STM preamp (cutoff frequency 20 kHz) and the rf amplifier (flat 20 dB gain between 100 kHz and 1 GHz). High frequency signals from Dulcinea are attenuated by low pass π filters. The entire apparatus is enclosed in an rf shielded box. The two level system of vibration damping for the STM is not shown.

Of these, seven MWNTs were sufficiently free of carbonaceous debris to allow comparison to Eq. 3.7. The measured frequencies are compared with those calculated for a cantilevered beam with L and d_o determined from SEM and assuming $d_i \approx 0.44 d_o$, as estimated from TEM micrographs. The frequency decreases systematically with increasing length of the MWNT (Fig. B.6) The frequency of the spectral peak for each of the MWNTs follows the overall trend in the calculation remarkably well [173]. There appears to be a systematic variation of E/ρ; smaller values of E/ρ are needed for longer MWNTs. Variations of E/ρ in the same range for MWNTs have been previously reported [33].

B.3 Redesign of the rf-STM circuit (June 2006)

Orcad PSpice was used to design a custom STM head with improved amplification of high-frequency signals. To optimize the detection and amplification of high-frequency signals, I built a custom rf-STM head. This head, based on the the Nanotec ambient air STM head, interfaced with the Nanotec Electrónica control electronics, Dulicinea, and the data acquisition and analysis

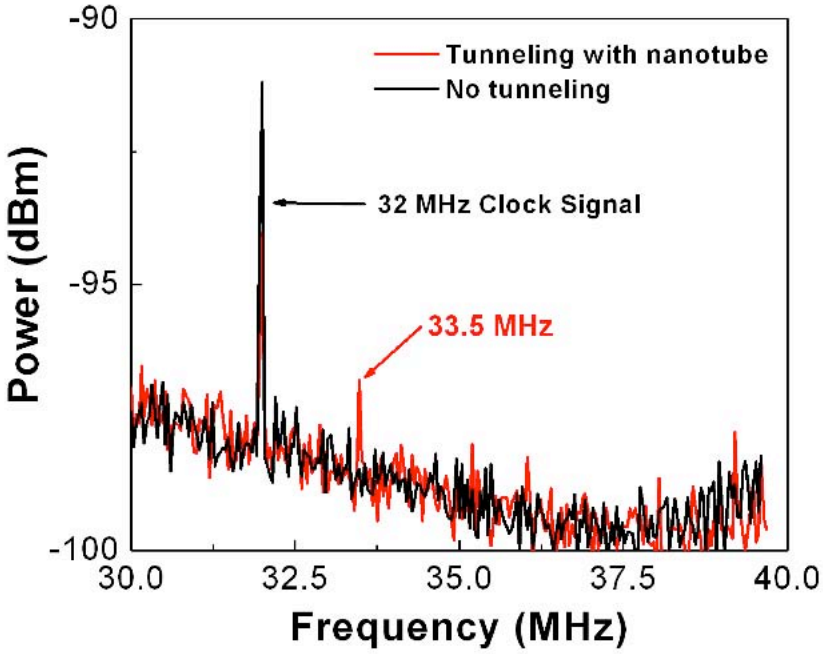

Figure B.5. The frequency spectra obtained with a MWNT affixed to an STM tip. Each line is the average of four scans taken consecutively. The red curve shows the spectral content with a tunnel current from the MWNT; the black curve plots the spectral content without a tunnel current. The 32 MHz clock signal due to the control electronics is present and dominates both spectra. The 33.5 MHz signal was only present when the MWNT was in tunneling range; this signal was attributed to the modulation of the tunnel gap.

system, WSxM© (http://www.nanotec.es).

Other than the obvious introduction of a high-frequency amplification circuit in the rf-STM head, the key differences between the two STM heads is as follows. First, the primary op amp in the current-to-voltage converter is an OPA129 in the rf-STM head, rather than a OPA111. OPA129 has a lower input bias current and guard shielding around its input pins, which helps reduce noise. The rf-STM head lacks noise filters on the power supply lines, resulting in a tendency to amplify 60-Hz noise. I think the lack of noise filters is a key reason atomic-resolution STM scans were never obtained with the rf-STM head. Other differences are (1) all the op amps in the rf-STM head are surface-mount components, (2) the rf-STM head's circuit board has a ground plane, unlike the circuit board in Nanotec's STM head, and (3) the electronic connections between the rf-STM head and the cable to the chassis are physically stronger.

An HP spectrum analyzer, Model 3585A, was used to analyze the spectral content output from

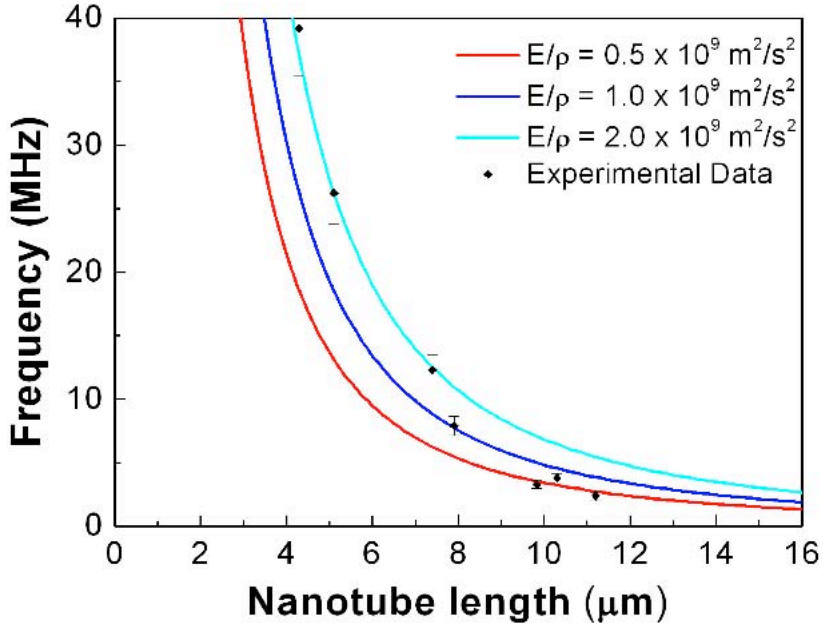

Figure B.6. A plot of the measured frequencies (diamonds) vs. nanotube length for MWNTs whose lengths were determined from SEM micrographs. Theoretical estimates of the fundamental frequency of oscillation, as given by Eq. 3.7, are plotted for comparison, assuming all nanotubes have diameters d_o=100 nm, d_i=44 nm. The error bars represent the uncertainty in diameter ($\pm$10 percent) and length ($\pm$2 percent).

the high-frequency portion of the rf-STM head. This spectrum analyzer has a range of 20 Hz to 40 MHz and was controlled by Collect Spectra.vi, a LabView program, which stored and averaged the data sets.

B.3.1 Design and theoretical performance of the June 2006 rf-STM circuit

The custom rf-STM preamp utilized an inductor-capacitor pair to split the tunnel current into two outputs. The low-frequency portion of the tunnel current wad shunted through the inductor, amplified and converted to a voltage, and sent to the feedback electronics, as described in Chapter 1. High-frequency signals were shunted through a capacitor into a series of two wideband (0.1–40 MHz) fixed-gain amplifiers. These high-frequency signals were input into the spectrum analyzer and recorded. A discussion of the active portions of the preamp and a simplified circuit schematic (Fig. B.7) follows. The following preamp design iteration is named June06 rfSTM, but frequently is referred to as the custom rf-STM preamp in following sections.

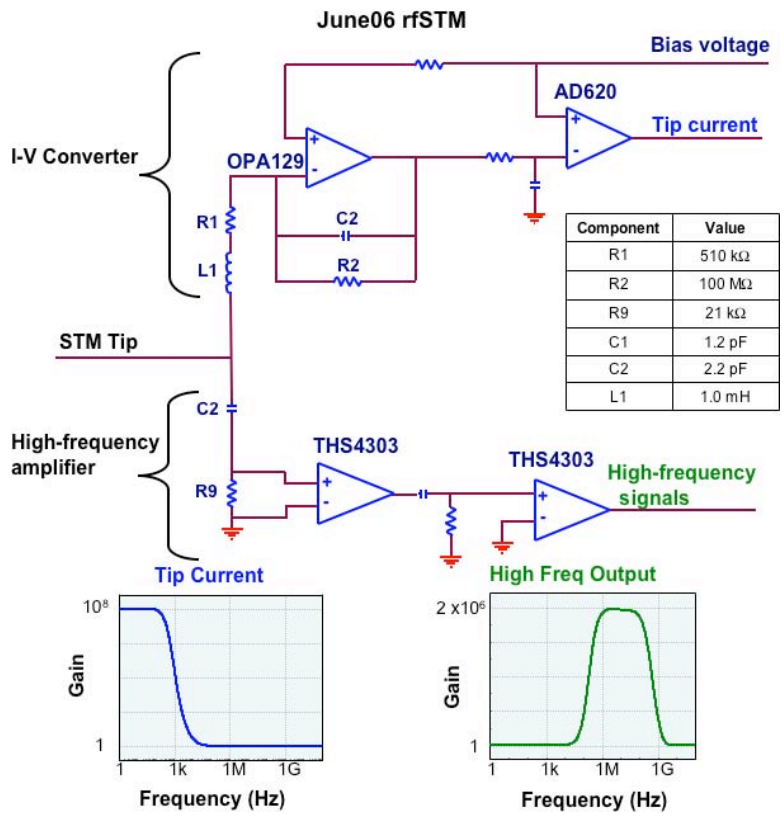

Component	Value
R1	510 kΩ
R2	100 MΩ
R9	21 kΩ
C1	1.2 pF
C2	2.2 pF
L1	1.0 mH

Figure B.7. Simplified circuit diagram for June06 rfSTM and the theoretical frequency response, which was modeled using OrCAD. Low frequency (<1 kHz) tunnel current signals are amplified with a gain of 10^8. High frequency signals between 1 and 100 MHz are amplified with a gain of 10^5.

OrCAD® Capture CIS, a Candence® circuit design and PSpice analysis program, was instrumental in the design and analysis of the June06 rfSTM circuit. Style files for the operational amplifiers (op amps) were downloaded from the manufacturers' websites, allowing for accurate modeling of the op amps' behavior. OrCAD®'s analysis capabilities allowed me to select low-pass and high-pass filter pairs for the ideal frequency response. Once the circuit design in OrCAD was completed, Mark Smith laid out the circuit components and traces for the circuit board, which was printed by PCBexpress. Mark also provided invaluable support throughout the circuit design process.

Op amp OPA129, in a current-to-voltage converter configuration, converted the tunnel current from the STM tip into a voltage with a gain of 10^8 V/A; the gain was set by $R2$. An active low-pass filter ($R2$ and $C2$ in parallel) with a 3dB point at 720 Hz shunted high frequency signals around OPA129. The tunnel current was the inverting input for OPA129; the bias voltage was the noninverting input. The output of OPA129 was the inverting input for AD620, a high accuracy instrumentation amplifier manufactured by Analog Devices. AD620, which was in a unity-gain

configuration, subtracted the bias voltage from the output of OPA129 and outputs the tunnel current. The tunnel current is measured in volts; the conversion is 0.1 V = 1 nA. This low-frequency portion of the rf-STM preamp is based predominately on the Nanotec Electrónica design. The only change to note is that Nanotec design utilizes op amp OPA111, which is now obsolete and was replaced by OPA129.

The high input impedance (10^{13} Ω || 1 pF) and low input bias current (± 30 fA) of OPA129 made it ideal for a current-to-voltage converter in an STM. At frequencies under 47 kHz the power response is linear and set by the supply voltages. The low input bias of OPA129 is achieved by having a non-standard pin layout. Pin 5 is the negative power pin, instead of pin 4. Pins 1 and 4 are not connected to the internal circuitry of OPA129, allowing a guard trace to completely surround the inputs (pins 2 and 3). OPA129 was originally designed by Burr-Brown and is currently manufactured by Texas Instruments.

High-frequency signals passed through the high-pass filter pair of $C1$ and $R1$ (3dB point at 0.26 MHz) into a series of two wideband fixed-gain amplifiers, THS4303. A Texas Instruments op amp, THS4303 has a linear gain of 20 dB (10 V/V) from 0.1 to 40 MHz and a nearly-linear gain (≥19 dB) from 40 MHz to 1000 MHz. In this circuit THS4303 was used in a wideband, noninverting gain configuration nearly identical to that shown in Fig. 43 of the TI application notes [175].

Through the J1 connector Dulcinea control electronics supplied the ±12 V power supply needed for OPA129 and AD620, the bias voltage, and an electronics ground. The bias voltage was controlled using WSxM software. An external power supply provided the ±2.5 V needed for the THS4303s.

B.3.2 Tests of the low-frequency performance of the June 06 rf-STM circuit

The Nanotec STM head was the basis for the current-to-voltage convertor portion of the rf-STM head. As expected, both heads had similar performance. While I was never able to obtain atomic-resolution STM scans with the rf-STM head, the rf-STM head accurately measured the topography of samples such as HOPG, as shown in Fig. B.8. This scan was obtained with a PtIr STM tip, a tunnel current set point of 1 nA and a potential bias of 500 mV. The quality of this image obtained with the rf-STM head is comparable to images obtained with the Nanotec STM head.

B.3.3 Tests of the high-frequency performance of the June 06 rf-STM circuit

Before attempting to measure TGMS signals, the output of the high frequency portion of the rf-STM circuit was tested for known signal outputs. A constant DC signal at the STM input should result in a 0 V output of the high-frequency portion, while AC signals above 1 MHz should have a gain of 10^6 at the high-frequecy output. Dr. Robert Santini, the director of instrumentation for the Jonathan Amy Facility for Chemical Instrumentation in the Department of Chemistry at Purdue,

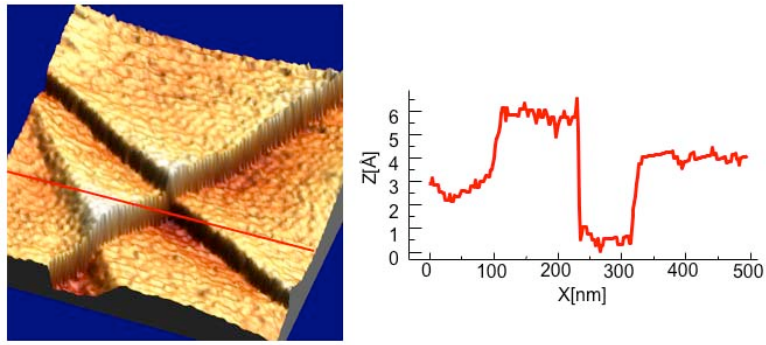

Figure B.8. Constant current STM image of HOPG obtained with the custom rf-STM head. There are overlapping step edges of 0.3 nm and 0.6 nm. The top graphene layer on the right-hand side has likely been peeled up slightly during the cleaving process, similar to the curving corners of a well-read book. This curling of the graphene layer results in a measured step edge of 0.4 nm. Scan parameters are frequency = 2.035 Hz, points = 256, (XY, Z) gain = (1,5), and (P, I) gain = (0.5, 0.1).

assisted us in the tests of the high-frequency portion. Dr. Santini's tests revealed that resistances in the power filtration circuit led to self-oscillation at 50 MHz for most input conditions. Second, in order to decrease the inductance of the circuit traces at MHz frequencies, the traces should have been 1–5 mm wide. Third, the first high-frequency op amp (U3) should have been placed as close to the STM top as physically possible, since the path between the STM tip and U3 acts as an antenna. Finally, the ground vias for the tantalum capacitors (C10 and C11) should have been much wider and should have been placed directly underneath the capacitors. These tantalum capacitors are part of the power filtration circuit for the high-frequency portion of the rf-STM circuit.

Rather than redesign the high-frequency portion, Dr. Santini suggested that we bypass it entirely and use commercial amplifiers instead to amplify the TGMS signal. Dr. Santini lent us a Keithley 110 high-impedence (10 MΩ input impedance, 50 Ω output impedance) unity-gain amplifier and a pair of Keithley 108 X10 wideband amplifiers. The unity-gain amplifier has an input impedance of 10 MΩ and an output impedance of 50 Ω; this amplifier was used to match the high-impedance of the STM input with the 50 Ω impedance of the X10 gain amplifiers. The entire high-frequency portion of the rf-STM circuit board (beginning with C2) was bypassed with a thin RG174 coax cable.

Bench-top tests of the Keithley amplifiers showed that they accurately amplified MHz signals generated by a function generator. Extensive tests of the rf-STM/Keithley pair revealed repeatable noise signals in the output of the high-frequency portion. The many approaches tried to reduce or block the noise included locating the rf-STM/Keithley pair in the electromagnetically shielded Hall Nanometrology Room at the Birck Nanotechnology Center, inserting a DC block between the rf-STM/Keithley pair and the spectrum analyzer, and adding pi filters to the voltage supply lines

between the Dulcinea control electronics and the rf-STM circuit. One key source of noise was the digital signal processor (DSP) in the STM control computer. The DSP generated harmonics at multiples of 2.4 MHz.

Despite all these challenges, numerous attempts were made to measure the TGMS signal of a MWNT affixed to a nickel STM tip. Prior to the TGMS experiments, the resonant frequency of each MWNT was first estimated by observing the electrostatically driven resonance in the dark-field microscope. These resonance measurements provided a guide for the frequency range to be measured with the HP3585A spectrum analyzer. Background spectra were obtained by recording the output of the Keithley amplifiers while the MWNT-Ni STM tip was millimeters above the HOPG substrate. At such a distance, no tunnel current flowed between the MWNT and HOPG. The MWNT-Ni STM tip was then brought to within tunneling range of the substrate using the conventional STM control electronics. The output of the Keithley amplifiers was again recorded. After these TGMS measurements, the status of the MWNT-Ni STM tip was checked in the darkfield microscope to ensure that the MWNT had not fallen off.

TGMS spectra were measured for seven MWNTs. While all of these spectra showed numerous noise peaks, none showed a reproducible signal that could be attributed to the MWNT's oscillations. At this point (August 2007), Prof. Arvind Raman had just obtained the laser doppler vibrometer. Since the LDV experiments were so successful, we ended the TGMS measurements.

B.3.4 June06 rf-STM circuit layout and bill of materials

Please note, due to a late change in the circuit design, R8 does not exist.

Table B.1. Bill of materials for rf-STM June06 circuit.

Symbol	Type	Footprint	Value
B1, B2	bead	1206	80 Ω
C1	capacitor	0603	1.2 pF
C2	capacitor	0603	2.2 pF
C3	capacitor	0603	240 pF
C4, C5, C6, C7	capacitor	0603	0.1 μF
C8, C9	capacitor	0402	47 pF
C10, C11	capacitor	7343	22 μF
C12	capacitor	0603	0.022 μF
J1	connector	C grid	5 pins
J2	connector	C grid	2 pins
J3	connector	SMA end launch 4	
L1	inductor		1 mH
R1	resistor	0402	510 kΩ
R2	resistor	RAZL0P3	100 MΩ
R3	resistor	0402	1.5 kΩ
R4	resistor	0402	43.0 kΩ
R5, R6, R7	resistor	0402	100 Ω
R9	resistor	0402	21 kΩ
R10, R11	resistor	0603	49.9 Ω
R12,R13	resistor	0402	30.1 Ω
T1-T9	test point	test point	
U1	op amp	8 SOIC	OPA129
U2	op amp	HCPL-0708 SO8	AD620AR 8
U3, U4	op amp	RGT	THS4303

June06 rf-STM circuit

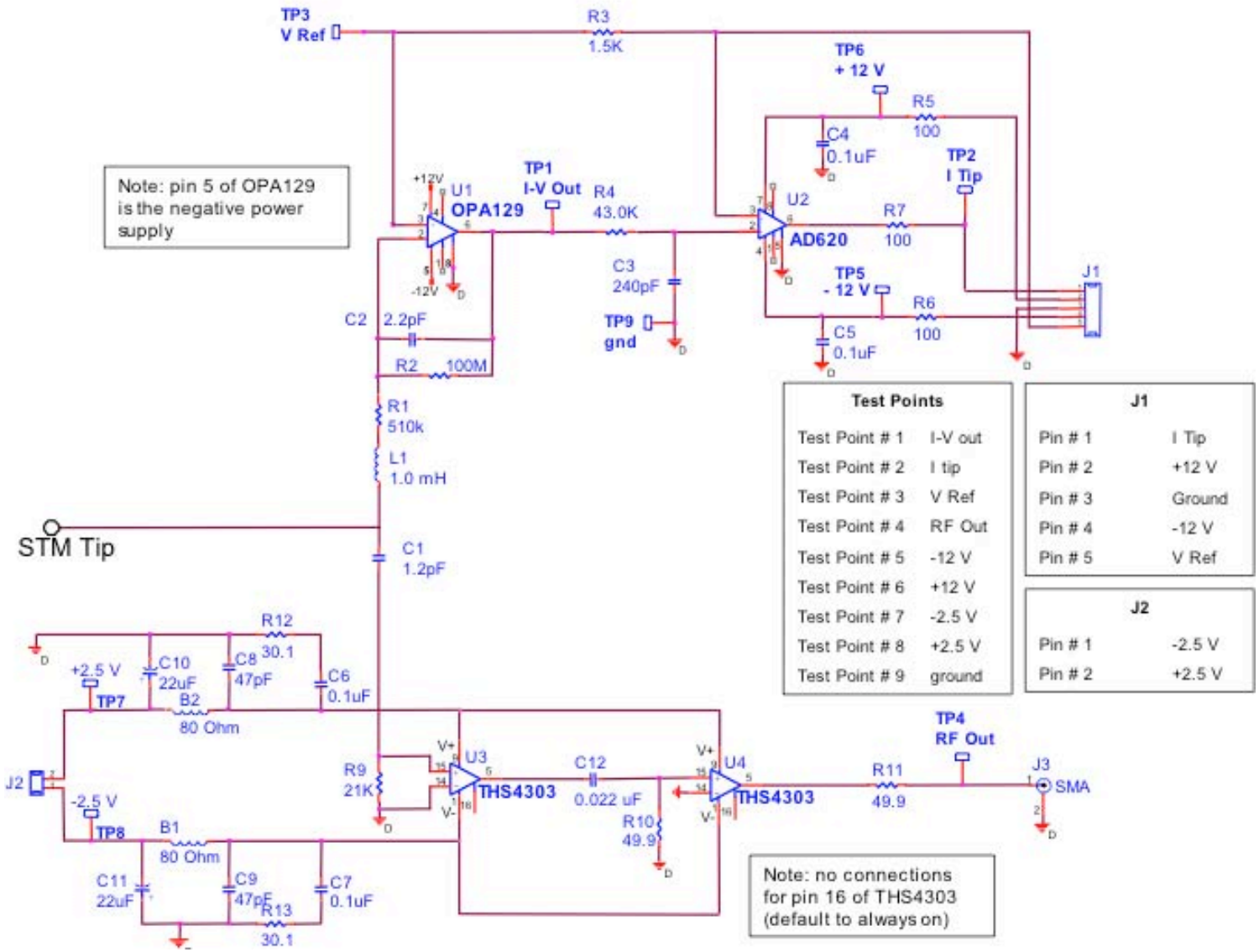

Test Points	
Test Point # 1	I-V out
Test Point # 2	I tip
Test Point # 3	V Ref
Test Point # 4	RF Out
Test Point # 5	-12 V
Test Point # 6	+12 V
Test Point # 7	-2.5 V
Test Point # 8	+2.5 V
Test Point # 9	ground

J1	
Pin # 1	I Tip
Pin # 2	+12 V
Pin # 3	Ground
Pin # 4	-12 V
Pin # 5	V Ref

J2	
Pin # 1	-2.5 V
Pin # 2	+2.5 V

Appendix C

Polytec MSA-400 Laser Doppler Vibrometer

Section 1 of this appendix lists the physical parameters and manufacturer specifications for the Polytec MSA-400 Laser Doppler Vibrometer. Section 2 presents a user's guide for the LDV, with a focus on thermal measurements of nanowires.

C.1 Manufacturer specifications for the Polytec MSA-400-M2-20 Micro System Analyzer

OFV-5000 vibrometer control (SN# 0108029)

MSA-400 optics head junction box (SN# 108301)

OFV-551 fiber vibrometer (SN# 0108030)

Mitutoyo NIR lenses $2\times$, $5\times$, $10\times$, $20\times$, $50\times$

Wavelength: 633 nm

VD-02 Velocity decoder Freq: 0.5 Hz–1.5 MHz • Resolution: 0.1–2.5 μm/s/$\sqrt{\text{Hz}}$ • minimum detectable velocity: $< 0.15\,\mu$m/s • Maximum velocity: 10 m/s

DD-300 Displacement decoder Freq: 50 kHz–20 MHz • Resolution: 0.1 pm/$\sqrt{\text{Hz}}$ • minimum detectable displacement: 0.1 pm • Maximum displacement: $\pm$75 nm

C.2 Basic instructions for using the Polytec MSA-400 LDV

1. Start-up procedure

   (a) Turn on the junction box. The toggle switch is in the back of the box.

Table C.1. Specifications for the M Plan NIR Mitutoyo objectives

Zoom	NA	Field of view (mm×mm)	WD (mm)	Pixel res. (μm)	Spot diam. (μm)	Focal depth (μm)
2	0.055	0.90×0.67	34.0	3.225	7.0	188
5	0.14	1.8×1.34	37.5	1.29	2.8	29
10	0.26	0.90×0.67	30.5	0.645	1.5	8.4
20	0.40	0.45×0.335	20.0	0.323	1.0	3.6
50	0.42	0.18×0.134	17.0	0.129	0.9	3.2

(b) Turn on the vibrometer controller.

(c) Turn on the data acquisition and analysis computer.

(d) At any time during the start-up, turn on the laser. The laser needs ∼20 minutes to warm up.

(e) If only the computer is turned on, the Polytec PSV 8.5 software is then available for data analysis. Before acquiring data, the junction box and vibrometer controller need to be turned on and the computer restarted.

2. Connect the vibrometer controller and junction box as shown in Fig. C.1. Note that the only difference between displacement and velocity scans is the input to "Vel In" of the junction box. For displacement scans, the auxiliary output of the vibrometer controller is connected to "Vel In;" for velocity scans, the velocity output of the vibrometer controller is connected to "Vel In."

3. Start the PSV 8.5 software and select the "Acquisition" icon in the toolbar. Starting PSV 8.5 activates the microscope display.

4. Bring the object into focus

   (a) If microscope screen image is all lines, turn off (small power button on screen) and back on again to refresh

   (b) Right-click on the microscope image to adjust the microscope brightness, contrast, and illumination. This menu is also available under Menu → Scan → Properties → Video

   (c) For best results, position the sample in the center of the field of view. Also, align the long scanning axis in the x-direction.

5. Select the "Perform 2D alignment" icon in the toolbar to begin aligning the laser

   (a) Create scan points by clicking where the laser beam reflects off of the sample

   (b) Depress the mouse wheel and drag the mouse to move the laser beam

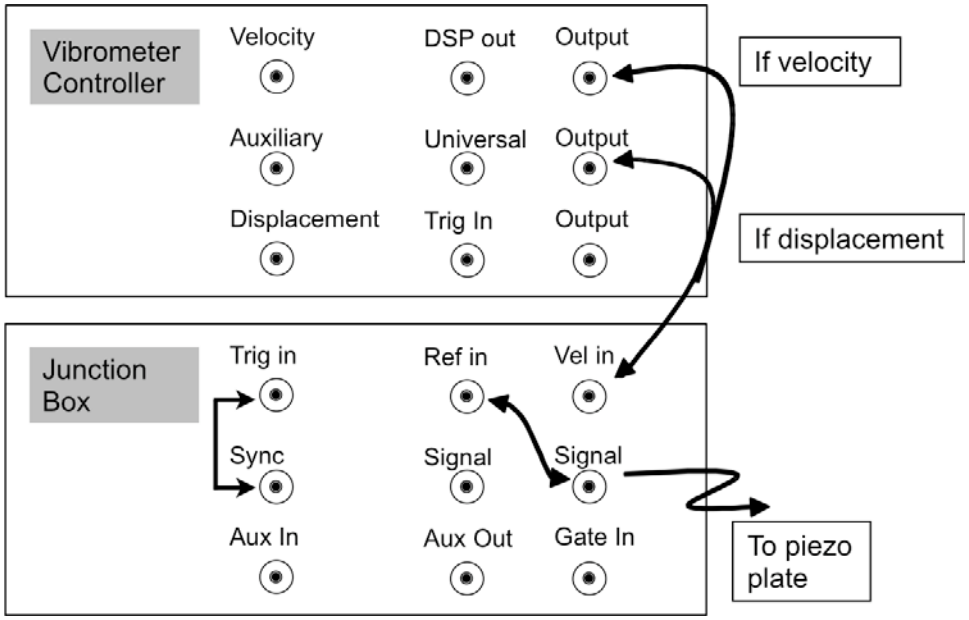

Figure C.1. A diagram indicating the connections for the coaxial cables connecting the Polytec vibrometer controller and junction box. Note that the displacement output of the vibrometer controller is connected to the output of the Auxiliary row, "Auxilliary," not the displacement row.

6. Define the scan range or individual scan points using the "Define Scan Points" option in the toolbar

   (a) Select a scan range (rectangle, ellipse, polygon) or individual points by selecting the appropriate box from the icon menu.

   (b) Set the density of scan points in x and y. Greater numbers of scan points yield higher spatial resolution but slower scan times.

   (c) For a background signal, ensure that the scan range or points includes a region that is not expected to oscillate in the frequency range of interest. For the nanowire experiments, the oscillations of the supporting SPM tip were measured.

7. Set scan options using the "A/D" icon in the toolbar and save the data

   (a) Choose scan parameters using the A/D box as described below

   (b) Check that the laser signal return is optimized

   (c) Select saving options, then begin scanning using the "Scan" icon.

8. Open the data analysis window by selecting the "Presentation" icon.

(a) The operating deflection shape (ODS) at any frequency can be plotted for driven vibration spectra.

(b) The thermal vibration spectra for any individual scan point can be displayed

9. Export data

   (a) Vibration spectrum: Save the vibration spectrum, either from the current point or all points, by clicking on the spectra and then selecting "Export to ASCII" under the file menu.

   (b) Movies of the operating deflection shape: After selecting the desired frequency and view, select File → Save animation.

   (c) Screen capture of the ODS: After adjusting the ODS to the desired view, pause the animation and select File → Save graphics

   (d) Microscope image without overlaid graphics: Turn "3D" off, remove root components, and save the microscope image using the Save graphics command.

10. Turn-off procedure

    (a) Quit PSV 8.5 and turn off computer

    (b) Turn off vibrometer controller

    (c) Turn off junction box

C.2.1 A/D box scan parameters

The A/D box has nine scan parameters tabs: General, Channels, Filters, Frequency, Window, Trigger, SE (speckle enhancement), and Vibrometer. Each of these tabs is described below.

- **General** controls the measurement mode – Time or FFT – as well as the signal averaging.
  - For movies of the driven operating deflection shape, choose FFT.
  - For the highest frequency resolution, chose Time.
  - Averaging options are Off, Magnitude, Complex, Peak Hold, and Time
  - Use Magnitude averaging for random excitation and Complex averaging for deterministic signals
  - For FFT scans, I typically used 20–30 averages
- **Channels** controls the type of measurement – Displacement or velocity – as well as the voltage ranges.

- The default is for both “Active” boxes to be checked and the direction in “+Z”
- For displacement measurements, the impedance should be 50 Ω; for velocity measurements, the impedance should be 1 MΩ. If displacement spectra are measured with a 1 MΩ impedance, the measured amplitude will be twice the actual amplitude. The frequencies will not be changed.
- Range should be adjusted to the smallest value between 200 mV and 10 V which does not lead to “Out of range” error messages.

- **Filters** are generally not used (“No Filter”) unless (1) the input signal will be integrated or differentiated or (2) selected frequencies within the selected measurement bandwidth will be selected

- **Frequency (FFT mode)** sets the frequency range and data resolution.
  - Choose a bandwidth greater than or equal to f_{max}.
  - If in displacement mode, $F_{min} \geq 50$ kHz.
  - For best frequency resolution, chose as close to 6400 lines as possible.

- **Time (time mode):** sets the sampling frequency and number of samples (2^N). Per the Nyquist criterion, the sampling frequency should be at least two times the highest signal frequency.

- **Windows** are available for both the vibrometer and reference signal.
  - For thermal, pseudo-random driven, and periodic chirp driven, use rectangular windowing of the vibrometer signal.
  - For random driven, use Hanning; for sinusoidal driven, use flat top; for transient driven, use exponential.

- **Trigger** is required for driven oscillations, but not thermal oscillations. For driven oscillations, ”External (TTL), rising” was used.

- **Speckle enhancement (SE):** Enabling SE will increase the number of averages on the noisier scan points so that the signal-to-noies ratio is comparable for all scan points.

- **Vibrometer** has the options of Velocity, Tracking Filter, Low Pass Filter, and High Pass filter.
  - Velocity was usually set to 25 mm/s/V
  - Tracking filter was always off
  - Low-pass filter was set to the maximum value of 1.5 MHz
  - High-pass filter was set to 100 Hz to block some environmental noise.

- **Generator** is used for driven scans, but not thermal scans. While a wide variety of waveforms are available, Pseudo Random, 2V excitations, was generally used. For thermal scans, ensure that the ”Active” box is not checked.

Appendix D

Mie Scattering Codes

D.1 Fortran code used to calculate $\mathscr{Q}_{sca}$

The Fortran code, InfiniteCylinder_v1.f, is based on a Fortran program, CALCYL.F, given in Appendix 2 of "Absorption and Scattering of Light by Small Particles" by C. F. Bohren and D. R. Huffman [70]. The below wavelength (WAVEL), cylinder radius (RAD), real medium refractive index (REFMED), and complex cylinder refractive index (REFRE and REFIM) should be adjusted for the appropriate experimental conditions.

```
PROGRAM CALCYL
C  %%%%%%%%%%%%%%%%%%%%%%%%%%%%%%%%%%%%%%%%%%
C  CALCYL CALCULATES THE SIZE PARAMETER (X) AND RELATIVE
C  REFRACTIVE INDEX (REFREL) FOR A GIVEN CYLINDER REFRACTIVE
C  INDEX, MEDIUM REFRACTIVE INDEX, RADIUS, AND FREE SPACE
C  WAVELENGTH.  IT THEN CALLS BHCYL, THE SUBROUTINE THAT COMPUTES
C  AMPLITUDE SCATTERING MATRIX ELEMENTS AND EFFICIENCIES
C  %%%%%%%%%%%%%%%%%%%%%%%%%%%%%%%%%%%%%%%%%%
COMPLEX REFREL,T1(200),T2(200)
DIMENSION ANG(200)
Open(Unit=5, File='SiNanoWire633.txt', STATUS='NEW')
WRITE (5,11)
C  %%%%%%%%%%%%%%%%%%%%%%%%%%%%%%%%%%%%%%%%%%
C  REFMED = (REAL) REFRACTIVE INDEX OF SURROUNDING MEDIUM
C  %%%%%%%%%%%%%%%%%%%%%%%%%%%%%%%%%%%%%%%%%%
REFMED=1.0
C  %%%%%%%%%%%%%%%%%%%%%%%%%%%%%%%%%%%%%%%%%%
C  REFRACTIVE INDEX OF CYLINDER = REFRE + I*REFIM
C  %%%%%%%%%%%%%%%%%%%%%%%%%%%%%%%%%%%%%%%%%%
REFRE=3.877
REFIM=0.019
REFREL=CMPLX(REFRE,REFIM)/REFMED
```

```
WRITE (5,12) REFMED,REFRE,REFIM
PI=3.14159265
C  %%%%%%%%%%%%%%%%%%%%%%%%%%%%%%%%%%%%%%%
C  RADIUS (RAD) AND WAVELENGTH (WAVEL) SAME UNITS
C  %%%%%%%%%%%%%%%%%%%%%%%%%%%%%%%%%%%%%%%
RAD=50
WAVEL=633
X=2.*PI*RAD*REFMED/WAVEL
WRITE (5,13) RAD,WAVEL
WRITE (5,14) X
WRITE (5,15)
CALL BHCYL (X,REFREL,T1,T2,QSCPAR,QSCPER)
NPTS=1
T11NOR=0.5*(CABS(T1(1))*CABS(T1(1)))
T11NOR=T11NOR+0.5*(CABS(T2(1))*CABS(T2(1)))
C  %%%%%%%%%%%%%%%%%%%%%%%%%%%%%%%%%%%%%%%
C  T33 AND T34 MATRIX ELEMENTS NORMALIZED BY T11
C  T11 IS NORMALIZED TO 1.0 IN THE FORWARD DIRECTION
C  POL = DEGREE OF POLARIZATION (INCIDENT UNPOLARIZED LIGHT)
C  %%%%%%%%%%%%%%%%%%%%%%%%%%%%%%%%%%%%%%%
DO 107 J=1,NPTS
TPAR=CABS(T1(J))
TPAR=TPAR*TPAR
TPER=CABS(T2(J))
TPER=TPER*TPER
T11=0.5*(TPAR+TPER)
T12=0.5*(TPAR-TPER)
POL=T12/T11
T33=REAL(T1(J)*CONJG(T2(J)))
T34=AIMAG(T1(J)*CONJG(T2(J)))
T33=T33/T11
T34=T34/T11
  107 T11=T11/T11NOR
C   WRITE (5,68) RAD,T11,POL,T33,T34,TPAR,TPER,QSCPAR,QSCPER
   WRITE (5,68) RAD,QSCPAR,QSCPER
WRITE (*,68)  RAD,QSCPAR,QSCPER
   68 FORMAT (1X,F8.2,2X,E13.6,2X,E13.6)
   11 FORMAT (/"CYLINDER PROGRAM: NORMALLY INCIDENT LIGHT"//)
   12 FORMAT (5X,"REFMED =",F8.4,3X,"REFRE =",E14.6,3X
     *"REFIM ="E14.6)
   13 FORMAT (5X, "CYLINDER RADIUS (nm) = ",F7.3,3X,
```

```
         * "WAVELENGTH (nm) = " ,F7.3)
   14 FORMAT (5X,"SIZE PARAMETER =",F8.3/)
   15 FORMAT (//2X,"RADIUS",10X,"QSCPAR",10X,"QSCPER"//)
C   15 FORMAT (//2X,"RADIUS",7X,"T11",12X,"POL",12X,"T33",12X,"T34",
C     *12X,"TPAR",12X,"TPER",10X,"QSCPAR",10X,"QSCPER"//)
STOP
END
C  %%%%%%%%%%%%%%%%%%%%%%%%%%%%%%%%%%%%%%%%
C  SUBROUTINE BHCYL CALCULATE AMPLITUDE SCATTERING MATRIX
C  ELEMENTS AND EFFICIENCIES FOR EXTINCTION AND SCATTERING
C  FOR A GIVEN SIZE PARAMETER AND RELATIVE REFRACTIVE INDEX
C  THE INCIDENT LIGHT IS NORMAL TO THE CYLINDER AXIS
C  PAR:ELECTRIC FIELD PARALLEL TO CYLINDER AXIS
C  PER:ELECTRIC FIELD PERPENDICULAR TO CYLINDER AXIS
C  %%%%%%%%%%%%%%%%%%%%%%%%%%%%%%%%%%%%%%%%
SUBROUTINE BHCYL (X,REFREL,T1,T2,QSCPAR,QSCPER)
COMPLEX REFREL,Y,AN,BN,A0,B0
COMPLEX G(1000),BH(1000),T1(200),T2(200)
DIMENSION THETA(200),ANG(200),BJ(1000),BY(1000),F(1000)
Y=X*REFREL
XSTOP=X+4.*X**.3333+2.
C  %%%%%%%%%%%%%%%%%%%%%%%%%%%%%%%%%%%%%%%%
C  SERIES TERMINATED AFTER NSTOP TERMS
C  %%%%%%%%%%%%%%%%%%%%%%%%%%%%%%%%%%%%%%%%
NSTOP=XSTOP
YMOD=CABS(Y)
NMX=AMAX1(XSTOP,YMOD)+15
NPTS=1
DO 555 J=1,NPTS
  555 THETA(J)=0
C  %%%%%%%%%%%%%%%%%%%%%%%%%%%%%%%%%%%%%%%%
C  LOGARITHMIC DERIVATIVE G(J) CALCULATED BY DOWNWARD
C  RECURRENCE BEGINNING WITH INITIAL VALUE 0.0 + I*0.0
C  AT J = NMX
C  %%%%%%%%%%%%%%%%%%%%%%%%%%%%%%%%%%%%%%%%
G(NMX)=CMPLX(0.0,0.0)
NN=NMX-1
DO 120 N=1,NN
RN=NMX-N+1
K=NMX-N
  120 G(K)=((RN-2.)/Y)-(1./(G(K+1)+(RN-1.)/Y))
```

```
C  %%%%%%%%%%%%%%%%%%%%%%%%%%%%%%%%%%%%%%%%
C  BESSEL FUNCTIONS J(N) COMPUTATED BY DOWNWARD RECURRENCE
C  BEGINNING AT N = NSTOP + NDELTA
C  BESSEL FUNCTIONS Y(N) COMPUTATED BY UPWARD RECURRENCE
C  BJ(N+1) = J(N), BY(N+1) = Y(N)
C  %%%%%%%%%%%%%%%%%%%%%%%%%%%%%%%%%%%%%%%%
NDELTA=(101.+X)**.499
MST=NSTOP+NDELTA
MST=(MST/2)*2
F(MST+1)=0.0
F(MST)=1.0E-32
M1=MST-1
DO 201 L=1,M1
ML=MST-L
  201 F(ML)=2.*FLOAT(ML)*F(ML+1)/X-F(ML+2)
ALPHA=F(1)
M2=MST-2
DO 202 LL=2,M2,2
  202 ALPHA=ALPHA+2.*F(LL+1)
M3=M2+1
DO 203 N=1,M3
  203 BJ(N)=F(N)/ALPHA
BY(1)=BJ(1)*(ALOG(X/2.)+.577213664)
M4=MST/2-1
DO 204 L=1,M4
  204 BY(1)=BY(1)-2.*((-1.)**L)*BJ(2*L+1)/FLOAT(L)
BY(1) =.636619772*BY(1)
BY(2)=BJ(2)*BY(1)-.636619772/X
BY(2)=BY(2)/BJ(1)
NS=NSTOP-1
DO 205 KK=1,NS
  205 BY(KK+2)=2*FLOAT(KK)*BY(KK+1)/X-BY(KK)
NN=NSTOP+1
DO 715 N=1,NN
  715 BH(N)=CMPLX(BJ(N),BY(N))
A0=G(1)*BJ(1)/REFREL+BJ(2)
A0=A0/(G(1)*BH(1)/REFREL+BH(2))
B0=REFREL*G(1)*BJ(1)+BJ(2)
B0=B0/(REFREL*G(1)*BH(1)+BH(2))
QSCPAR=CABS(B0)*CABS(B0)
QSCPER=CABS(A0)*CABS(A0)
```

```
DO 101 K=1,NPTS
T1(K)=B0
  101 T2(K)=A0
DO 123 N=1,NSTOP
RN=N
AN=(G(N+1)/REFREL+RN/X)*BJ(N+1)-BJ(N)
AN=AN/((G(N+1)/REFREL+RN/X)*BH(N+1)-BH(N))
BN=(REFREL*G(N+1)+RN/X)*BJ(N+1)-BJ(N)
BN=BN/((REFREL*G(N+1)+RN/X)*BH(N+1)-BH(N))
DO 102 J=1,NPTS
C=COS(RN*THETA(J))
T1(J)=2.*BN*C+T1(J)
  102 T2(J)=2.*AN*C+T2(J)
QSCPAR=QSCPAR+2.*CABS(BN)*CABS(BN)
  123 QSCPER=QSCPER+2.*CABS(AN)*CABS(AN)
QSCPAR=(2./X)*QSCPAR
QSCPER=(2./X)*QSCPER
C QEXPER=(2./X)*REAL(T2(1))
C QEXPAR=(2./X)*REAL(T1(1))
RETURN
END
```

The output of the above Fortran code is saved as "SiNanoWire633_matrix.txt" and is given below.

```
CYLINDER PROGRAM: NORMALLY INCIDENT LIGHT

     REFMED =  1.0000   REFRE =  0.387700E+01   REFIM =  0.190000E-01
     CYLINDER RADIUS (nm) =   5.000   WAVELENGTH (nm) = 633.000
     SIZE PARAMETER =   0.050

  RADIUS          QSCPAR          QSCPER

     5.00     0.333851E-01   0.232472E-03
    10.00    0.348122E+00   0.188290E-02
    15.00    0.163471E+01   0.645613E-02
    20.00    0.462656E+01   0.155888E-01
    25.00    0.687577E+01   0.311169E-01
    30.00    0.656217E+01   0.552895E-01
    35.00    0.557216E+01   0.914917E-01
```

40.00	0.476084E+01	0.146797E+00
45.00	0.422571E+01	0.242116E+00
50.00	0.406950E+01	0.461965E+00
55.00	0.512439E+01	0.125162E+01
60.00	0.877412E+01	0.332410E+01
65.00	0.671257E+01	0.254393E+01
70.00	0.486165E+01	0.189195E+01
75.00	0.402043E+01	0.179955E+01
80.00	0.353167E+01	0.200380E+01
85.00	0.317163E+01	0.254983E+01
90.00	0.288094E+01	0.368535E+01
95.00	0.382501E+01	0.373235E+01
100.00	0.200540E+01	0.121540E+01
105.00	0.118649E+01	0.563510E+00
110.00	0.154127E+01	0.511242E+00
115.00	0.177777E+01	0.582353E+00
120.00	0.180067E+01	0.764852E+00
125.00	0.168753E+01	0.162270E+01
130.00	0.174388E+01	0.911419E+00
135.00	0.119338E+01	0.227894E+00
140.00	0.161077E+01	0.466165E+00
145.00	0.311864E+01	0.129306E+01
150.00	0.347326E+01	0.156187E+01

D.2 Matlab code used to plot $\mathcal{Q}_{sca}$

```
% Mie_SiNanowires_633nm.m

% Reads and plots data from variation of "Normally Illuminated
%      Infinite Cylinder"
% This variation calculations Qsca as a function of cylinder
%      diameter
% Appendix C, Bohren and Huffman's text
% Absorption and Scattering of Light by Small Particles

% 28 May 2008
```

```
clc; clear all; close all;

v1 = FuncMatrixRead('SiNanoWire633_matrix.txt');

radius = v1(:,1); % radius in nanometers
QSCPAR = v1(:,2); QSCPER = v1(:,3);

diam = 2*radius; % diam in nm
Qsca = 0.5*(QSCPAR + QSCPER);   % assuming circ polarized light

figure(1)
hold on
plot(diam, Qsca, 'g','LineWidth', 2)
plot(diam, Qsca, 'g.','MarkerSize',20)
hold off
xl=xlabel('Diameter (nm)'), yl=ylabel('Q_{scatt}')
tl=title('Mie scattering of 633 nm light from a Si nanowire...
      (N=3.877+i0.019)')
axis([0 300 0 inf])
set(xl,'fontsize',14); set(yl,'fontsize',14); set(tl,'fontsize',16);
```

Appendix E

Matlab code for power spectral density (PSD) analysis of vibration spectra

Below is the Matlab code used to generate Fig. 5.13. The subroutines called by

```
NNB_vacuum_4April09Analysis_v1.m
```

are given in full, in the order in which they are called.

E.1 Main analysis code

```
% NNB_vacuum_4April09Analysis_v1.m
% Reads in data of Nanoneedle NNB taken 23 Jan 09
% Labbook pg 56-59
clc; close all; clear all


% STEP 1: Load data, previously imported and saved as a .mat file
load NNB_Res5_Pt2_23Jan09;
   NNB_Res5_Pt2 = NNB_Res5_Pt2_23Jan09;

% STEPS 2&3:  Call Pwelch_PlotAnalysis
% 1) subtracts any background offset
% 2) calculates PWelch spectra (m^2/Hz)
% 3) smooths the data by Navg and Nsmooth

Lw = 8; overlap = 50; % window length divisor (length = N/Lw)
%  and overlap
[DataA, FreqA] = Pwelch_PlotAnalysis2(NNB_Res5_Pt2, Lw, overlap, 0);
[DataB, FreqB] = Pwelch_PlotAnalysis2(NNB_Res5_Pt2, 4, overlap, 0);
```

```
[DataC, FreqC] = Pwelch_PlotAnalysis2(NNB_Res5_Pt2, 1, overlap, 0);

figure(10); semilogy(FreqA, DataA, 'r.')

% STEP 4: Find peaks in the oscillation spectrum
df = FreqA(2) - FreqA(1);
MPD = ceil((0.07e6)/df);         MPH = 8e-25;

clc
[pksA, indA] = findpeaks(DataA, 'MinPeakHeight', MPH, ...
  'MinPeakDistance',MPD);
PeakFA = FreqA(indA); PeakFA*1e-6
PeaksA = [indA(2:8)' PeakFA(2:8)]; % Index & Freq (Hz)
[pksB, indB] = findpeaks(DataB, 'MinPeakHeight', MPH, ...
  'MinPeakDistance',MPD);
PeakFB = FreqB(indB); PeakFB*1e-6
PeaksB = [indB(2:8)' PeakFB(2:8)]; % Index & Freq (Hz)


% STEP 5: Calculate the power in each peak using trapzoidal integration
% Choose a peak width of 200 kHz, centered around PeakF
PW = 0.1e5; % Hz
[FsegA, PksegA, FrangeA, PowerA] = PeakPower(FreqA,DataA,PeaksA,PW,df);
[FsegB, PksegB, FrangeB, PowerB] = PeakPower(FreqB,DataB,PeaksB,PW,df);
disp('Frequency ranges (MHz)'), [FrangeA*1e-6  FrangeB*1e-6]
disp('Calculated power (m^2)'), [PowerA'*1e18   PowerB'*1e18]


% STEP 6: Use cftool to plot curve fits
% First, scale data so that Peak(1,2) = 1
DataScaledA = DataA/max(PksegA(:,1));
DataScaledB = DataB/max(PksegB(:,1));

% Curve fits from cftool: General model:
%    f(x) = ((A*1e18)/(Q*f^3))*(1/((1-(x/f)^2)^2 + (x/(Q*f))^2))+N
%FitX = ['A'; 'N'; 'Q'; 'f']

% Fits to smoothed data (Lw = 4)
FitA1 = [4.987e-6; 5.675e-12; 197.5; 1.4e5];   % j=2?
FitA2 = [1.409e-5; 9.998e-11; 422.1; 1.542e5]; % j=2?
FitB   = [1.901e-7; 6.659e-5;  268.3; 3.147e5]; % j=3?
```

```
FitC   = [3.932e-6; 0.000137;  263.9; 3.902e5]; % j=3
FitD   = [8.218e-7; 5.622e-5;  310.9; 5.326e5]; % j=?
FitE   = [5.986e-7; 8.689e-5;  248.7; 7.667e5]; % j=4
FitF   = [2.414e-5; 4.013e-5;  182.4; 1.81e6 ]; % j=6
FitG  = [2.87e-5; 8.638e-7;   373.2; 2.328e6]; % j=7

Fit = [FitA1 FitA2 FitB FitC FitD FitE FitF FitG];
FitFreq = Fit(4,:)'*1e-6

% Define frequency ranges, fr, for curve fits
% Calculate the fit curves using LorentzFRF
frA1 = [1.35e5 1.45e5];
frA2 = [1.45e5 1.6e5];
frB  = [FsegB(1,2) FsegB(length(FsegB),2)];
frC  = [FsegB(1,3) FsegB(length(FsegB),3)];
frD  = [FsegB(1,4) FsegB(length(FsegB),4)];
frE  = [0.7631e6 0.7703e6];
frF  = [1.804e6  1.816e6];
frG  = [2.323e6  2.332e6];

CurveA1 = LorentzPSD(frA1, FitA1);
CurveA2 = LorentzPSD(frA2, FitA2);
CurveB = LorentzPSD(frB, FitB);
CurveC = LorentzPSD(frC, FitC);
CurveD = LorentzPSD(frD, FitD);
CurveE = LorentzPSD(frE, FitE);
CurveF = LorentzPSD(frF, FitF);
CurveG = LorentzPSD(frG, FitG);


% STEP 7:  Calculate percentage errors from eigenfrequency ratio
% Define the eigenfrequency points.
% Calculate ratio of frequency peaks, ExpRatio
ExpRatio1(1) = 0;
ExpRatio1(2) = FitA1(4)/FitA1(4);
ExpRatio1(3) = FitA2(4)/FitA1(4);
ExpRatio1(4) = FitB(4)/FitA1(4);
ExpRatio1(5) = FitC(4)/FitA1(4);
ExpRatio1(6) = FitD(4)/FitA1(4);
ExpRatio1(7) = FitE(4)/FitA1(4);
ExpRatio1(8) = FitF(4)/FitA1(4);
```

```
ExpRatio2(1) = 0;
ExpRatio2(2) = FitA1(4)/FitA2(4);
ExpRatio2(3) = FitA2(4)/FitA2(4);
ExpRatio2(4) = FitB(4)/FitA2(4);
ExpRatio2(5) = FitC(4)/FitA2(4);
ExpRatio2(6) = FitD(4)/FitA2(4);
ExpRatio2(7) = FitE(4)/FitA2(4);
ExpRatio2(8) = FitF(4)/FitA2(4);

disp('Experimental ratio, f_j/f_A1'); ExpRatio1'
disp('Experimental ratio, f_j/f_A2'); ExpRatio2'

% From CantileverSeparationConstants.m
a = [1.8751 4.6941 7.8548 10.995 14.1372 17.2788 ...
           20.4204 23.5619 26.7035 29.8451];
for i = 1:length(a)
    ratio(i) = a(i)/a(2);
    FreqRatio(i) = ratio(i).^2;
end
ratio(1) = 0; FreqRatio(1) =0;

for i = 1:8
    err1(i) = abs(FreqRatio(i) - ExpRatio1(i))/FreqRatio(i);
    err2(i) = abs(FreqRatio(i) - ExpRatio2(i))/FreqRatio(i);
end

%%%%%%%%%%%%%%%%%%%%%%%%%%%%%%%%%%%%%%%%
figure(2)
semilogy(FreqB*1e-6, DataB,'k.'); hold on
semilogy(CurveA1(:,1)*1e-6, CurveA1(:,2)*max(PksegB(:,1)), 'r', ...
    'LineWidth', 3);
semilogy(CurveA2(:,1)*1e-6, CurveA2(:,2)*max(PksegB(:,1)), 'r', ...
    'LineWidth', 3);
semilogy(CurveB(:,1)*1e-6, CurveB(:,2)*max(PksegB(:,1)), 'm', ...
     'LineWidth', 3);
semilogy(CurveC(:,1)*1e-6, CurveC(:,2)*max(PksegB(:,1)), 'm', ...
     'LineWidth', 3);
semilogy(CurveD(:,1)*1e-6, CurveD(:,2)*max(PksegB(:,1)), 'y', ...
     'LineWidth', 3);
semilogy(CurveE(:,1)*1e-6, CurveE(:,2)*max(PksegB(:,1)), 'b', ...
```

```
     'LineWidth', 3);
semilogy(CurveF(:,1)*1e-6, CurveF(:,2)*max(PksegB(:,1)), 'g', ...
     'LineWidth', 3);
semilogy(CurveG(:,1)*1e-6,  CurveG(:,2)*max(PksegB(:,1)), 'c', ...
    LineWidth', 3);
hold off
axis([0.05, 2.5, 1e-26, 5e-21]);
  xl=xlabel('Frequency (MHz)'); yl=ylabel('Power (m^2/Hz)');
  tl=title('NNB: In vacuum (650 mTorr)');
  set(xl, 'FontSize', 18); set(yl, 'FontSize', 18);
  set(gca,'FontSize', 18); set(tl, 'FontSize', 22);
```

E.2 Pwelch PlotAnalysis2.m

```
function [Data, Freq] = Pwelch_PlotAnalysis2 ...
     (data, Lwindow, overlap, i);
% Calculates PWelch for given data, number of windows, and overlap
% Number of windows = length(data)/Lwindow
% if i == 1, then plot instant Pwelch.

% STEP 1a: Import data (do before runing Pwlech_PlotAnalysis)
% STEP 1b: Calculate and subtract average displacement of NNB
N = length(data);
AvgZ = sum(data(:,2))/N;
disp('Un-shifted average z(t)'), AvgZ
data(:,2) = data(:,2) - AvgZ;
disp('Check that average z(t) is now zero'), [sum(data(:,2))/N]

% STEP 2: Use PWelch to calculate the PSD of data
dt= data(2,1) - data(1,1);
Fs = 1/dt;
% Experiment with window lengths and overlap
h1 = spectrum.welch('hamming', length(data)/Lwindow, overlap);
hopts1 = psdopts(h1,data);  % Default options
  set(hopts1,'Fs',Fs,'SpectrumType','onesided','centerdc',false);
hpsd1 = psd(h1,data(:,2), 'Fs', Fs);
%power_hpsd1 = avgpower(hpsd1);
```

```
FullData = hpsd1.data; FullFreq = (hpsd1.frequencies);
L = length(FullFreq);

% STEP 3b: Omit frequencies < 0.05 MHz
df = FullFreq(2)-FullFreq(1);
StartInd = ceil((0.05e6)/df);
Freq = FullFreq(StartInd:L);
Data = FullData(StartInd:L);

% sometimes I want the instant plot, othertimes I don't
if i == 1;
    figure(1)
    semilogy(Freq, Data, 'k.', Freq, Data, 'k')
    axis([0.05e6, inf, -inf, inf]);
    xl=xlabel('Frequency (Hz)');
    yl=ylabel('Power/Frequency (m^2/Hz)');
    tl=title('PWelch PSD spectra data');
    set(xl, 'FontSize', 16); set(yl, 'FontSize', 16);
    set(tl, 'FontSize', 16); set(gca,'FontSize', 16);
end
```

E.3 PeakPower.m

```
function [Fseg, Pkseg, Frange, Power] = ...
     PeakPower(Freq,Data,Peaks,PW,df)

d_ind = floor((PW/2)/df); % [integer] df in indices to count

S = size(Peaks)
if S(1) ==1
    L=1
else
    L=length(Peaks)
end

for i = 1:L  % had been i=1:length(Peaks)
```

```
    if (Peaks(i,1) - d_ind) < 1
        Fseg(:,i)  = Freq(1: (Peaks(i,1) + d_ind));
        Pkseg(:,i) = Data(1: (Peaks(i,1) + d_ind));
        Frange(i,:) = [1, Peaks(i,2) + PW/2];
    else
        Fseg(:,i)  = Freq((Peaks(i,1) - d_ind): (Peaks(i,1) + d_ind));
        Pkseg(:,i) = Data((Peaks(i,1) - d_ind): (Peaks(i,1) + d_ind));
        Frange(i,:) = [Peaks(i,2) - PW/2, Peaks(i,2) + PW/2];
    end
    Power(i) = trapz(Fseg(:,i), Pkseg(:,i));
end
```

E.3.1 LorentzPSD.m

```
function [FRF] = LorentzPSD(FreqRange, Fit)

% Calculates a matrix of the Lorentzian curve fit given data
% output from the cftool (G, N, W, F) and the subset frequency
% range (fmin to fmax).
% General model:
% f(x) = ((A*1e18)/(Q*f^3))*(1/((1-(x/f)^2)^2 + (x/(Q*f))^2))+N
% The output data curve, DataCurve, is easily plotted on
% top of the original data

A = Fit(1);
N = Fit(2);
Q = Fit(3);
F = Fit(4);
fmin = FreqRange(:,1);
fmax = FreqRange(:,2);

% Calculate the subset frequency vector, x (same units as f)
x = linspace(fmin, fmax); %x = x';
%y = G./((1-(x/F).^2).^2 + (x/(Q*F)).^2) + N;
y = ((A*1e18)./(Q*F^3))*(1./((1-(x./F).^2).^2 + (x./(Q*F)).^2))+N;
FRF = [x' y'];
```

Appendix F

Copyright statements for previously published work

Portions of this SAND report, both text and figures, have been previously published in academic journals. The previously published figures are noted by an appropriate citation in the figure caption. Furthermore, the text of this report is only slightly modified from the Laura Biedermann's PhD dissertation, "Vibrational Spectra of Nanowires Measured Using Laser Doppler Vibrometry and STM Studies of Epitaxial Graphene," Purdue University, 2009.

Figures 5.3 and 5.5 are derived from Figs. 1 and 3 of "Flexural vibration spectra of carbon nanotubes measured using laser doppler vibrometry," by L. B. Biedermann, R. C. Tung, A. Raman, and R. G. Reifenberger, which was published in *Nanotechnology* 20:3, 035702 (2009). Portions of sections 5.2 and 5.3 were derived from this *Nanotechnology* manuscript. Permission to reprint these figures and the accompanying text was grated by Sarah Ryder of IOP Publishing.

Figures 7.2, 7.5–7.8, 7.10, and 7.12–7.14 were previously published in "Insights into few-layer epitaxial graphene growth on $4H$-SiC$(000\bar{1})$ substrates from STM studies", by L. B. Biedermann, M. L. Bolen, M. A. Capano, D. Zemlyanov, and R. G. Reifenberger, which was published in *Physical Review B* 79: 125411 (2009). Chapter 7 is an expanded discussion of the experiments and results presented previously in *Physical Review B*. Permission to reprint these figures and the accompanying text was grated by Eileen LaManca of the American Physical Society (APS).

DISTRIBUTION:

1 Prof. R. Reifenberger
Birck Nanotechnology Center
1205 W. State St.
West Lafayette, IN 47905

10	MS 0892	L. Biedermann, 1748
1	MS 0892	R. Dondero, 1748
10	MS 0892	S. Howell, 1748
1	MS 0892	A. Ross, 1748
1	MS 1070	M. Spletzer, 1526
1	MS 1072	R. Cernosek, 5719
1	MS 1210	S. Martin, 5935
1	MS 0899	Technical Library, 9536 (electronic)
1	MS 0123	D. Chavez, LDRD Office, 1011

Sandia National Laboratories